



UNIVERSITÀ
DEGLI STUDI
DI PADOVA



University College Dublin
Ireland's Global University

Sede Amministrativa: Università degli Studi di Padova

Consiglio nazionale delle ricerche, Istituto di Fotonica e Nanotecnologie (CNR-IFN), Padova

Dipartimento di Ingegneria dell'Informazione (DEI)

SCUOLA DI DOTTORATO DI RICERCA IN: Ingegneria dell'Informazione

INDIRIZZO: Scienza e tecnologia dell'Informazione

CICLO: XXX

TESI IN COTUTELA

FUV- EUV Polarimetric System Development

Direttore della Scuola: Prof. Andrea Neviani

Supervisore: Ch.mo Prof. Piergiorgio Nicolosi

Supervisore: Ch.mo Prof. Gerry O'Sullivan

Dottorando: Ahmed Eid Hamed Gaballah

2018



UNIVERSITÀ
DEGLI STUDI
DI PADOVA



University College Dublin
Ireland's Global University

FUV- EUV Polarimetric System Development

Ahmed Eid Hamed Gaballah

Thesis presented for the degree of

Doctor of Philosophy

To the

School of Physics
College of Science
University College Dublin, Ireland

and

Department of Information Engineering
University of Padova, Italy

Supervisors: Prof. Gerry O'Sullivan, Prof. Piergiorgio Nicolosi

Head of School: Prof. Martin Grünewald

2018

Summary

The generation and control of linearly and circularly polarized light in the far ultraviolet (FUV) and extreme ultraviolet (EUV) spectral regions are required in different frontiers research and technological areas ranging from material science, where the nature of the beam plays a fundamental role in the light-matter interaction, to optical components developments including devices for manipulation of the light polarization state. This has pushed researchers to examine and outline new optical elements as optical polarizers and quarter-wave retarders (QWRs) specifically designed for this spectral range and thought to be used in proper optical arrangements in order to provide valuable information about physical and optical properties of materials and optical coatings.

In this thesis, we present an EUV reflectometer facility located in the Institute for Photonics and Nanotechnologies-CNR Padua (Italy) which was implemented for polarimetric measurements within a suitably wide spectral range (90-160 nm) where some important spectral emission lines are, as the hydrogen Lyman alpha 121.6 and Oxygen VI (103.2 nm) lines. The development part focuses on the design and fabrication of an optical linear polarizer based on four reflection gold-coated mirrors to be inserted in the EUV reflectometer optical path. In this way, the facility can be used as an EUV spectroscopic ellipsometric system. The robustness of the methodology and the system were tested to characterize the optical and structural properties of a single layer aluminum mirror as quarter wave retarder (QWR) by deriving its amplitude component $\tan\psi = \frac{r_p}{r_s}$ and phase difference δ .

The second part of the thesis comes from the desire to explore new optical materials employed as a capping layer for optical coatings in the far ultraviolet (FUV) and extreme ultraviolet (EUV) spectral regions. The materials are mostly absorptive in these spectral regions, thus the availability of high-performance optical coatings for the short wavelengths is quite restricted for this reason. In this part, we present a phase retarder optical component based on *SnTe/Al* bilayer covering the spectral range between 80 nm and 160 nm. The measurements have been performed using an EUV reflectometer facility improved for ellipsometric measurements. The specimen has been fully characterized at hydrogen Lyman-alpha line (121.6 nm) in terms of reflectance and ellipsometric

parameters, i.e. the ratio r , ratio of the Fresnel coefficient, and the phase difference δ introduced between the $-s$ and $-p$ reflected components. To our knowledge, such structure based on *SnTe* haven't been studied as capping layer for a wide spectral range in the vacuum ultraviolet, although the throughputs are not those expected for this structure. The drop-in performances are attributed to the carbon contamination on the sample surface identified by additional reflectance measurements at 160 nm wavelength. The results also confirm the potentialities and the advantages of such non-invasive optical approach.

Lastly, the whole system consisting of the reflectometer and the polarizer could be particularly useful as diagnostic tools in EUV ellipsometry field. The system can be a relatively simple complement to large-scale facilities and can be applied to test optical components by deriving their efficiency, determining the Mueller Matrix terms, and even to the analysis of optical surface and interface properties of thin films. In addition, the QWRs developed in this framework could be used in other experimental applications for generating EUV radiation beams of suitable polarization, for characterizing and controlling the polarization state of EUV radiation beams and to be inserted in an ellipsometric scheme in order to characterize optical devices.

Sommario

La generazione e il controllo di luce polarizzata linearmente e circolarmente nell' ultravioletto da vuoto (VUV) e nell'estremo ultravioletto (EUV) è argomento di grande interesse in diversi ambiti tecnologici e di ricerca, che riguardano la fisica solare, la scienza dei materiali e lo sviluppo di componenti ottici, inclusi dispositivi per la manipolazione dello stato di polarizzazione della luce. Questo ha spinto i ricercatori ad esaminare e disegnare ritardatori di fase, polarizzatori e lamine al quarto d'onda, specificamente progettati per questa regione spettrale e pensati per essere usati in diverse configurazioni ellissometriche al fine di fornire preziose informazioni sulle proprietà fisiche e ottiche di materiali e rivestimenti ottici.

In questa tesi, presentiamo l'implementazione di un riflettometro EUV, già presente presso l'Istituto di fotonica e Nanotecnologie-CNR di Padova (Italia), recentemente implementato e testato per misure polarimetriche in una banda spettrale ampia, compresa tra i 90 e i 160 nm, di grande interesse per la fisica solare.

La prima parte del lavoro descrive lo sviluppo, la progettazione e la fabbricazione di un polarizzatore lineare ottico costituito da quattro specchi in oro opportunamente assemblati. Il dispositivo è stato accoppiato al riflettometro EUV in modo da permettere l'utilizzo dell'intero sistema per analisi ellissometriche nell'EUV. La robustezza della metodologia sperimentale è stata poi validata per caratterizzare le proprietà ottiche e strutturali di uno specchio di alluminio monostato proposto come lamina al quarto d'onda broadband. Per questo specchio, sono stati derivati i due parametri ellissometrici caratteristici $\tan\psi = \frac{r_p}{r_s}$ e δ , la differenza di fase.

La seconda parte della tesi tratta, invece, lo sviluppo e la progettazione di lamine al quarto d'onda broadband innovative. Le attività nell'ambito di questo argomento includono la ricerca di nuovi materiali, la simulazione numerica e la caratterizzazione. A tale scopo, sono state studiate le proprietà di una lamina al quarto d'onda basata su $SnTe/Al$, per la quale il $SnTe$ è stato utilizzato come strato protettivo al fine di migliorare la stabilità e l'efficienza, contro l'ossidazione e la contaminazione proprie dell'alluminio. Il campione è stato caratterizzato attraverso misure di tipo polarimetrico e di riflettanza. Le lamine al quarto d'onda sviluppate in questo contesto

potrebbero essere utilizzate in altre applicazioni sperimentali per la generazione, la caratterizzazione e il controllo di luce polarizzata nell' EUV.

L'intero strumento, composto dal riflettometro e dal polarizzatore, è a tutti gli effetti un sistema ellissometrico nell' EUV. Lo si propone in maniera complementare a large scale facility per testare componenti ottici disegnati per l'EUV, per lo studio di coating e di interfacce di film sottili.

Acknowledgment

Firstly, I would like to express my deepest gratitude and appreciations to my advisor Prof. Piergiorgio Nicolosi for the continuous support of my doctorate study and related research, for his guidance, patience, motivation, and spacious knowledge. Besides my advisors, I would also like, to place on record my deep sense of gratitude to Prof. Gerry O’Sullivan for critical review of the thesis.

The author wishes to thank Dr. Fergal O’Reilly and Dr. Tom McCormack at University College Dublin (UCD) for giving me the opportunity to work in their labs and made me learn a lot during my mobility. Special thanks to all the staff in UCD for having insightful discussions during the weekly meetings.

I owe a debt of gratitude to Dr. Paola Zuppella for supporting me during the experimental part, especially for providing peer teaching and mentoring through the EUV experiment that was quite challenging for me, also I am thankful to the academic and administrative staff in CNR-IFN Padova for their adherence in supporting me even on non-academic topics. I am thankful also to the director of the IFN Dr. Luca Poletto. In the heart of this, I express my genuine gratitude to the administrative staff of the department of information engineering (DEI) for their plentiful cooperation.

Furthermore, I also like to extend my acknowledgments to the financial support from The Education, Audiovisual and Culture Executive Agency (EACEA), Erasmus Mundus Joint Doctorate Program EXTATIC under framework partnership Agreement No. 2012-0033. Thanks also to the COST action for supporting my scientific activities.

Finally, I am so much grateful to my parents for their faith in me and supporting me to become the person who I am today. My deepest feeling to my wife and my daughter who has been with me all along this work. Thanks for your patience and understanding

Publications and Conference Presentations

I. Publications during PhD program

1. **A.E.H. Gaballah**, P. Zuppella, A.J. Corso, P. Nicolosi “Optical and structural characterization of reflective quarter wave plates for EUV range” Proc. SPIE 9905, Space Telescopes and Instrumentation: Ultraviolet to Gamma Ray (2016).
2. **A.E.H. Gaballah**, P.Zuppella, Nadeem Ahmed, K. Jimenez, G. Pettinari, A. Gerardino , P. Nicolosi, “A tabletop polarimetric facility for the EUV spectral range:implementations and characterization“ Proc. 10235, UV and X-ray Optics: Synergy between Laboratory and Space (2017).
3. K. Jimenez, **A.E.H. Gaballah**, Nadeem. Ahmed, P. Zuppella, P.Nicolosi “Optical and structural characterization of Nb, Zr, Nb/Zr, Zr/Nb thin films on Si₃N₄ membranes windows. “Proc. 10236, Damage to VUV, EUV, and X-ray Optics (2017).
4. **A.E.H. Gaballah**, P. Nicolosi, Nadeem Ahmed, K. Jimenez, G. Pettinari, A. Gerardino, P.Zuppella “EUV polarimetry for thin film and surface characterization and EUV phase retarder reflector development” Rev. Sci. Instrum. 89, 015108 (2018).
5. **A.E.H. Gaballah**, P. Nicolosi, P.Zuppella, Nadeem Ahmed, K. Jimenez, G. Pettinari, A. Gerardino, P. Nicolosi “Vacuum ultraviolet quarter wave plates based on *SnTe/Al* bilayer: design, fabrication and ellipsometric characterization” submitted to applied surface science, Appl. Surf. Sci. 463 (2018) 75–81. doi:10.1016/j.apsusc.2018.08.190.
6. Nadeem. Ahmed, P. Nicolosi, **A.E.H. Gaballah**, K. Jimenez, P. Zuppella “EUV reflective ellipsometry in laboratory: determination of the optical constants and phase retarder properties of *SiO₂* at hydrogen Lyman-alpha” submitted to Materials Research Express.

II. Other publications by Author

7. A. Ashery, G. Said, W. A. Arafa, **A. E. H. Gaballah**, and A. A. M. Farag, “Structural and optical characteristics of PEDOT/n-Si heterojunction diode,” Synthetic Metals, vol. 214, pp. 92-99, 2016.
8. A.Ashery, G. Said, W. A. Arafa, **A. E. H. Gaballah**, and A. A. M. Farag, “Morphological and crystalline structural characteristics of PEDOTTM/TiO₂ nanocomposites for applications towards technology in electronic devices,” Journal of Alloys and Compounds, vol. 671, pp. 291-298, 2016.

9. A. Ashery, A. A. M. Farag, **A. E. H. Gaballah**, G. Said, and W. A. Arafa, “Nanostructural, optical and heterojunction characteristics of PEDOTTM/ZnO nanocomposite thin films,” *Journal of Alloys and Compounds*, vol. 723, pp. 276–287, 2017.

II. Presentations at Conferences and Workshops

- ❖ PTB Seminar VUV and EUV Metrology "EUV ellipsometric measurements: a proof of concept" 19-20 October 2017 at **PTB Berlin, Germany (Oral Presentation)**.
- ❖ Extatic Workshop, “EUV polarimetry in laboratory: thin film characterization and EUV phase retarder reflector development” 22-24 September 2017 at Faculty of Nuclear Sciences & Physical Engineering of CTU, **Prague (Oral Presentation)**.
- ❖ SPIE conference: Synergy between Laboratory and Space, **Prague, Czech Republic** 24-27 April 2017 (**Poster Presentation**).
- ❖ SPIE conference: Damage to VUV, EUV, and X-ray Optics, **Prague, Czech Republic** 24-27 April 2017 (Poster Presentation).
- ❖ Extatic Workshop, “Optical and structural characterization of reflective quarter wave plates for EUV range” 16-20 January 2017 at (ICTP) the International Centre for Theoretical Physics in **Trieste, Italy. (Oral Presentation)**.
- ❖ Training session on the characterization of multilayers mirrors in EUV spectral range at BEAR beamline, **ELETTRA synchrotron Trieste, Italy**, 11-14 November 2016.
- ❖ Workshop on Multilayer and neutron scattering 10 -11 November 2016 the University of **Twente, Netherland (Poster Presentation)**.
- ❖ COST Action workshops: MP1203 (X-ray optic metrology), Sept. 19-21, 2016 **Athens, Greece (Oral Presentation)**.
- ❖ SPIE conference astronomical telescope and instrumentation in Edinburgh, United Kingdom, Jun 26-30, 2016 (Poster Presentation).
- ❖ Training session on the characterization of multilayers mirrors in EUV spectral range at BEAR beamline, **ELETTRA synchrotron Trieste, Italy**, 12-15, 24-26 May 2016.
- ❖ Extatic Workshop “Optical characterization of reflective quarter wave retarder in FUV-EUV range” 11-15 January 2016 at the University of **Southampton, UK. (Oral Presentation)**.
- ❖ Extatic Workshop, “EUV Multilayer optical coatings development” at MUT (**Warsaw Poland**), 20 -24 October 2014 (**Oral Presentation**).

Glossary

UV	Ultraviolet
VUV	Vacuum Ultraviolet
FUV	Far Ultraviolet
EUV	Extreme Ultraviolet
SXR	soft X-ray
SE	Spectroscopic ellipsometry
ML	Multilayer
SUMER	Solar Ultraviolet Measurements of Emitted Radiation
SOHO	Solar Heliospheric Observatory
SolmeX	Solar magnetism explorer
CUSP	Coronal UV Spectro-polarimeter
VIRCOR	EUV imaging polarimeter
SUSP	Scanning UV Spectro-polarimeter
ChroME	Chromospheric magnetic explorer
TRACE	Transition Region and Coronal Explorer
SDO	Solar Dynamic Observatory
CL	Capping layer
FELs	Free electron lasers
QWR	Quarter Wave retarder
QWP	Quarter Wave Plate
TEY	Total Electrons Yield
HCL	Hollow Cathode lamp
LPP	Laser Produced plasma
GDP	Gas Discharge plasma
HHG	High harmonic generation

Table of Contents

Summary	ii
Sommario	iv
Acknowledgment	vi
Publications and Conference Presentations	vii
Glossary	ix
Chapter.1 Introduction to FUV- EUV Polarimetry	1
1.1. Motivations	1
1.2. Extreme Ultraviolet Radiation.....	3
1.3. Interaction of EUV Radiation with Matter	4
1.4. Reflection and Transmission at Interfaces.....	6
1.5. Optical Coatings for FUV-EUV Polarimetry.....	12
1.6. EUV Polarimetry for Space Imaging	14
1.7. EUV Spectroscopic Ellipsometry	16
1.8. Thesis Breakdown	18
Chapter.2 Mathematical Representation of Polarized Light.....	19
2.1. The Polarized Light and Polarization Ellipse	19
2.2. Stokes Representation of Polarized Light	22
2.3. Mueller Matrix Formalism	26
2.4. Jones Representation of Polarized Light.....	29
Chapter.3 Multi-Angle FUV-EUV Ellipsometry	32
3.1. The FUV-EUV Normal Incidence Reflectometer	32
3.2. FUV- EUV Radiation Source.....	34
3.3. The Channel Electron Multiplier Detector (CEM)	36
3.4. Opto-Mechanical Design of the FUV-EUV Polarizer	38
Chapter.4 System Calibration and Phase Retarder Reflector.....	46
4.1. Polarimetric Characterization of The Light Source	46
4.2. Characterization of Al Phase Retarder Reflector.....	52
4.3. Conclusion.....	64
Chapter.5 Quarter Wave Plates Based on <i>SnTe/Al</i> bilayer.....	66
5.1. Introduction	66
5.2. Experimental Methods.....	68

5.3. Structural Characterization	70
5.4. Conclusion.....	79
Chapter.6 Thesis Summery.....	80
Appendices	82
Appendix A. Deposition Facilities.....	83
Appendix B. MATLAB Code	87
Appendix C. Opto-Mechanical Designs.....	93
Bibliography.....	97

Chapter.1

Introduction to FUV- EUV Polarimetry

1.1. Motivations

Nowadays, thin films and multilayer mirrors (ML) are essential components of the modern optical and semiconductor industry which requires high-quality standards in fabrication and characterization techniques. Multilayers can provide sufficient throughput power through reflective optics for successfully and economically production of integrated circuit components.

In the extreme ultraviolet spectral region (EUV), photolithography has opened the door for the development of faster computers by increasing the density of components in integrated electronic chips [1]. In addition, there is also a growing interest in high k elements in order to overcome the limitation of conventional gates by improving present Si-based electronics [2]. Furthermore, the development of new EUV radiation sources like free electron lasers (FEL) and high harmonic generation (HHG) are expected to open new frontiers for the material science community [3,4]. Last but not least, space-weather research attracts new growing interest in space exploration. The recent solar missions to outer space have opened new windows on the possibility of understanding the energetic processes and dynamics of both the solar plasma and solar wind which significantly affect life on our planet [5,6]. Thus, the accurate investigation of the magnetic field variables will enable us to understand the basic underlying physics and predict space weather events.

In this sense, improved evaluation techniques to study thin film properties and multilayer optics at shorter wavelengths are strongly required especially for systems designed for EUV

lithography and space imaging telescopes. However, the availability of non-destructive characterizing techniques in the far ultraviolet (FUV) and the EUV spectral ranges is quite restricted as most of the optical components are strongly absorptive at these high energy photons [7]. The synchrotron light source is a leading technology for materials science analysis which can deliver valuable knowledge about optical constants, films thickness and intermixing of layers in optical coatings [8]. However, access to such large-scale facilities needs financial support and experiment proposal approval for beam time schedule. Therefore, laboratory-based experimental systems are highly desired as a good option to expensive and time-consuming facilities for fast, low cost and reliable preliminary experiments. This has motivated researchers to investigate and design new characterizing techniques to overcome the difficulties of measurements.

Spectroscopic ellipsometry (SE) is one of the promising techniques adapted for such a purpose. It can provide valuable information about the structural and optical properties of materials using Müller matrix formalism and Stokes parameters. The method is not invasive and can give more information about the sample with high-precision and accuracy. It may worth to mention that the need to develop electronic devices based on magnetic elements motivates the development of such technique since linearly and circularly polarized radiations are very sensitive to the interaction of EUV radiation with electrons in magnetic materials and compounds [9].

This work presents the design requirements, development and characterization of the optical components (i.e. polarizer and quarter-wave retarders) required for arranging an ellipsometric system. The systems works over the spectral range from 90 to 160 nm wavelength, which covers well some important spectral lines such as the hydrogen emission lines at 121.6 nm, 97.2 and 91.2 as well as the Oxygen VI line at 103.2 nm. The thesis mainly consists of two parts. The first part discusses the implementation and polarimetric characterization of an EUV reflectometer facility which is located in the Institute for Photonics and Nanotechnologies-CNR Padua (Italy). The reflectometer which is already available in the laboratory was coupled with a four reflection EUV linear polarizer in order to be used as an EUV spectroscopic ellipsometer system. In spite of the wide range of interests for FUV- EUV polarimetry, there is a notable lack of retarders available for polarimetric measurements in this bandpass. In particular, the availability of FUV- EUV quarter-wave retarders (QWR) would be particularly useful for complete Stokes polarimetry when used in conjunction with the linear polarizers. The second part focuses on developing of reflective

QWRs using innovative capping layers of *SnTe* on top of aluminium specimen. Lastly, the EUV reflectometer facility was tested to characterize the optical and structural properties of different samples and quarter wave retarders (QWRs) by deriving their reflectance amplitude components and their phase effect on the impinging light.

1.2. Extreme Ultraviolet Radiation

Extreme ultraviolet (EUV) radiation is a portion of the electromagnetic spectrum referring to short wavelengths where photons are energetic enough to excite atoms. In some literature, the region with wavelengths from 200 nm down to the soft x-ray edge at 10 nm is usually referred to as vacuum ultraviolet (VUV) [10,11]. The radiation at these energy ranges are strongly absorbed by air molecules so the whole working system must be maintained in high-vacuum. Fig. 1.1 shows the electromagnetic spectrum indicating the EUV and soft x-ray regions, however; it is difficult to identify clear-sharp boundaries between them. In astronomy, the term extreme ultraviolet (EUV) denotes the wavelengths between 10 nm and the photoionization edge of the hydrogen atom at 91.2 nm [12], while longer wavelengths are called far ultraviolet (FUV). In the most recent publications, the EUV spectral range is defined to lie somewhere between 5 nm and 40 nm [7]. For the purposes of this thesis, the convention used by the astronomy community is adopted.

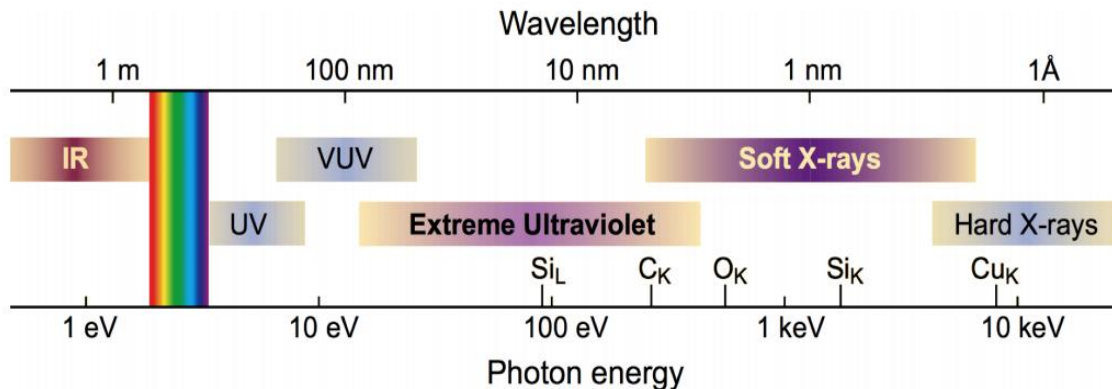


Figure 1.1. The electromagnetic spectrum indicating the spectral range from the Infra-Red (IR) up to X-rays [7].

EUV radiation is naturally emitted by the solar corona in outer space, but nowadays it is widely used in several applications which require high brilliant light sources with spatial coherence

and enough monochromaticity. This can be generated artificially in different ways such as hot plasma emission, synchrotron radiation and high harmonic generation. The emission of hot plasma is usually the common sources of EUV radiation in laboratory scale experiments; among the sources are Discharge-Produced Plasmas (DPP) and Laser-Produced Plasmas (LPP). In DPP, the emission of EUV radiation occurs by applying a high-voltage through the working gases according to the required emission of the desired spectral line. In LPP, EUV radiation is emitted by focusing a high irradiance laser pulse onto a solid target. It is associated with an ablation process in which the laser pulses heat the target material which will begin to sputter and vaporize. As the target becomes ionized, free electrons are released. These electrons start to collide with each other and with the sputtered atoms of the target materials creating the plasma. The plasmas created depend on laser intensity, laser wavelength, pulses duration, focusing lens and the target material [13].

The use of synchrotron radiation has produced enormous growth of scientific research utilizing the vacuum ultraviolet to soft x-ray regions. In such large facilities, the radiation is emitted by accelerating relativistic electrons through a periodic sequence of magnetic field; the commonly used assemblies to produce synchrotron radiation are bending magnets, undulators, and wigglers [14]. Currently, the emission of EUV radiation from Free Electron Lasers (FELs) has taken a significant consideration as a light source for EUV lithography and other applications due to their tunability and the availability of high-power accelerators. The emission of EUV radiation from (FELs) is also based on the same physical principle of synchrotron radiation [15].

1.3. Interaction of EUV Radiation with Matter

The interactions of EUV radiation with matter can be explained by two models, the photo-absorption and the coherent scattering models. In photo-absorption, the energy of the incoming photon exceeds the ionization energy of the bound electron. When the photon energy is not enough to ionize atoms, the most frequently occurring process is a coherent scattering of the photon without energy loss [7]. Accordingly, the electron-photon interactions model can describe the interaction of EUV radiation with matter through the concept of scattering cross sections of particles as follows:

$$f^o(\omega) = f_1^o(\omega) + if_2^o(\omega) \tag{1.1}$$

where f_1^o and f_2^o are the atomic scattering factors of an element associated with the reflection and absorption respectively. The materials show characteristics interaction with EUV radiation. This in turn was described by the concept of the complex optical constant (\hat{n}) as:

$$\hat{n} = 1 - \delta + i\beta, \quad 1.2$$

where δ and β , or equivalently n and k , are the optical constants and these can be experimentally derived by applying methods based on reflectance and transmittance measurements combined with an optimized algorithm for fitting analysis. In the EUV, the refractive index (\hat{n}) can be described in terms of the atomic scattering factors f_1^o and f_2^o as [7]:

$$\hat{n} = 1 - \delta + i\beta = 1 - \frac{n_a r_e \lambda^2}{2\pi} f^o(\omega), \quad 1.3$$

where n_a is the atomic density per unit volume, and λ is the wavelength of the EUV radiation and r_e is the classical electron radius which is defined as:

$$r_e = \frac{e^2}{4\pi\epsilon_0 m_e c^2} = 2.82 \times 10^{-15} \text{ m} \quad 1.4$$

From equations

(1.1) Error! Reference source not found. Error! Reference source not found. Error! Reference source not found and (1.3) δ and β can be related to the real and imaginary parts of the scattering factor respectively. This can be represented as:

$$\delta = \frac{n_a r_e \lambda^2}{2\pi} f_1^o \quad 1.5$$

$$\beta = \frac{n_a r_e \lambda^2}{2\pi} f_2^o$$

Several indicators can be derived from equation (1.3). The real part of the optical constant n in the EUV spectral range is smaller than one compared to the visible light. The absolute values of δ and β decrease for higher energies, thus, the complex refractive index \hat{n} of all materials approaches unity. Fig. 1.2 shows the variation of the real part of the optical constant n across the electromagnetic spectrum, associated with resonances (ω) at each region.

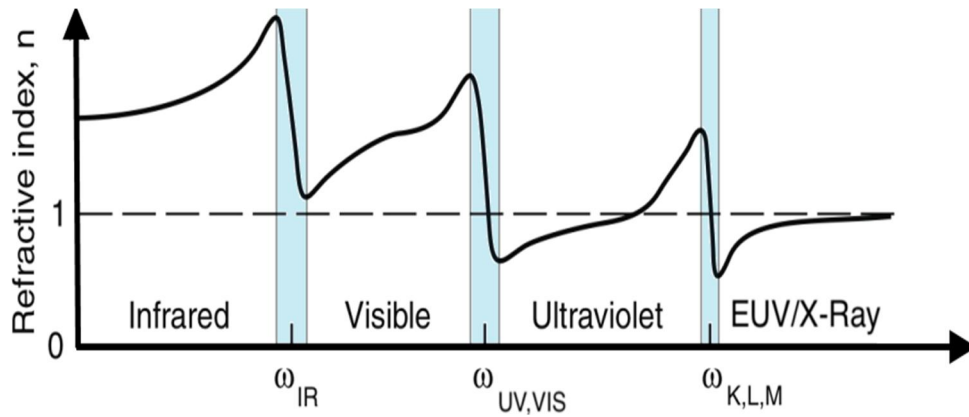


Figure 1.2. Variation of refractive index n over the electromagnetic spectrum, strong variations are observed near resonance edges which are dropping toward unity for higher frequencies [7].

1.4. Reflection and Transmission at Interfaces

The electromagnetic waves traveling in space are associated with some optical phenomena as reflection, transmission and refraction occurring at the interfaces between two media of different refractive indices.

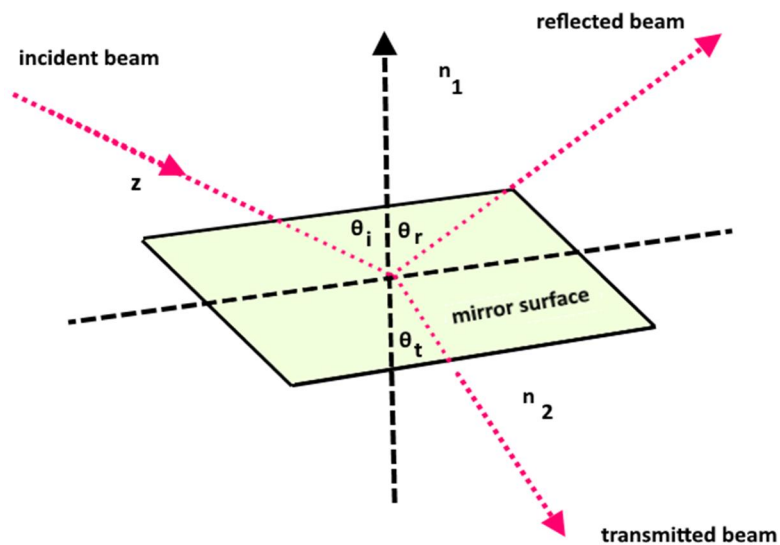


Figure 1.3. Reflection and transmission at the interface of two different media.

To study these phenomena, we will inspect three distinct waves traveling along the propagation direction z as seen in the Fig. 1.3. The index n_1 defines the material on the mirror

surface, and the index n_2 defines the material below the surface. k_i and k_r specify incident and reflected plane wave making angles of θ_i and θ_r , respectively, with the normal to the interface. K_t specifies the transmitted wave that makes an angle θ_t with the interface normal [16]. The electric field components of the incident; reflected and transmitted wave can be expressed respectively as:

$$E_i(z, t) = E_0 e^{-i(\omega_i t - k_i z)} \quad 1.6$$

$$E_r(z, t) = E_0 e^{-i(\omega_r t - k_r z)} \quad 1.7$$

$$E_t(z, t) = E_0 e^{-i(\omega_t t - k_t z)} \quad 1.8$$

At the interface, the three fields have the same frequency (ω), where $\omega_i = \omega_r = \omega_t$, and the tangential components of all wave vectors must be equal; therefore,

$$k_i \sin \theta_i = K_r \sin \theta_r = K_t \sin \theta_t \quad 1.9$$

As the incident and reflected wave are in the same medium, their wave vectors will be equal; therefore, the law of reflection is obtained:

$$\theta_i = \theta_r \quad 1.10$$

The proportionality of the wave-vector (k) and the refractive index n is expressed as

$$k_i = \frac{\omega}{c} n_1, \quad k_t = \frac{\omega}{c} n_2 \quad 1.11$$

Equation (1.9) can be expressed in the form of refractive index n ; to obtain, Snell's law:

$$n_1 \sin \theta_i = n_2 \sin \theta_t \quad 1.12$$

The complex dispersion relation in this case is:

$$\frac{\omega}{k} = \frac{c}{\tilde{n}} = \frac{c}{1 - \delta - i\beta} \quad 1.13$$

Accordingly, the equation of the plane wave can be written in terms of the complex refractive index as:

$$E = E_0 e^{i(Kz - \omega t)} = E_0 e^{i\left(\frac{2\pi n}{\lambda} z - \omega t\right)} = \underbrace{E_0 e^{i\omega\left(\frac{z}{c} - t\right)}}_a \underbrace{e^{\frac{-i2\pi\delta}{\lambda} z}}_b \underbrace{e^{\frac{2\pi\beta}{\lambda} z}}_c \quad 1.14$$

The first term (a) in the exponent of equation (1.14) describes a plane wave propagating through vacuum while the second term (b) contributes an additional phase shift proportional to δ due to the different optical density of the propagation medium. The last term (c) accounts for absorption within the medium. The imaginary part of the optical constant (β) can be directly related to the absorption coefficient (α) by the relation:

$$I = I_0 e^{\alpha z} \quad \text{or} \quad \alpha = \frac{2\pi\beta}{\lambda} \quad 1.15$$

In the visible region, a single surface mirrors can work at nearly normal incidence angles with high reflectance. No comparable optics are available in the EUV spectral range. Accordingly, reflective mirrors can be used at grazing incidence as there are no transmissive optical elements for EUV radiation. Due to the growing demands of the industrial applications in EUV which require high reflectance and an intensive radiation, multilayer coatings are considered key components of EUV lithography at near-normal incidence [17]. Multilayers are optical coating thin films consisting of two or more alternating layers of high and low refractive index materials [18]. The concept of multilayer mirrors arose from Bragg diffraction law described by crystallography as:

$$m\lambda = 2d \sin \theta \left(1 - \frac{2\delta}{\sin^2 \theta}\right)^{1/2} \quad 1.16$$

where m is the reflection order, λ is the wavelength, θ is the grazing incidence angle, d represents the thickness of the bi-layer and δ represents the real part of the refractive index of the bilayer. A standing wave will be created at the multilayer surface upon reflection which in turn enhances the reflectance through constructive interference. Figure 1.4 shows the calculated reflectivity for a $[Si/Mo]_{60}$ multilayers mirror near 13.5 nm. A typical periodic multilayer structure is shown inset of the figure.

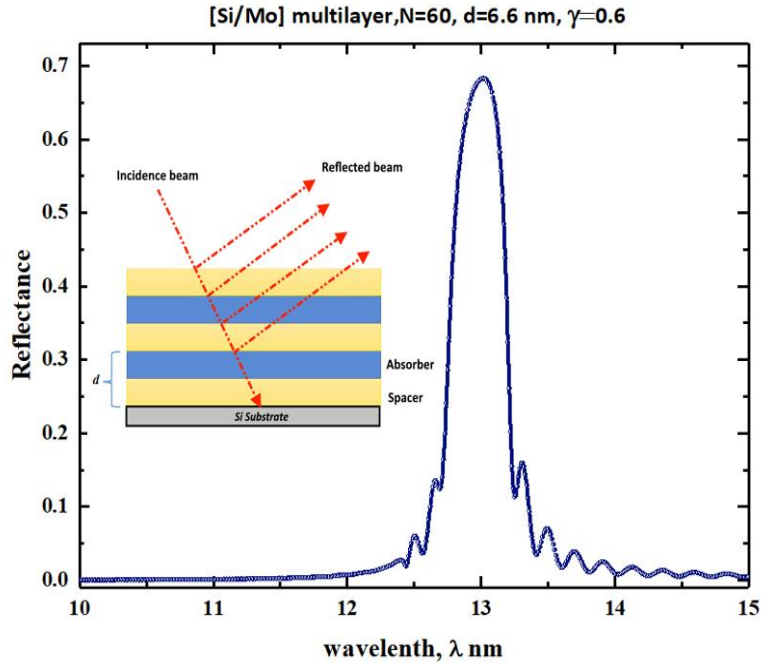


Figure 1.4. Calculated spectral reflectance for $[Si/Mo]_{60}$ multilayers tuned around 13 nm.

The equations describe the reflection and transmission of an electromagnetic wave incident on the interface between two optical media with different refractive indices are the Fresnel's equations [19].

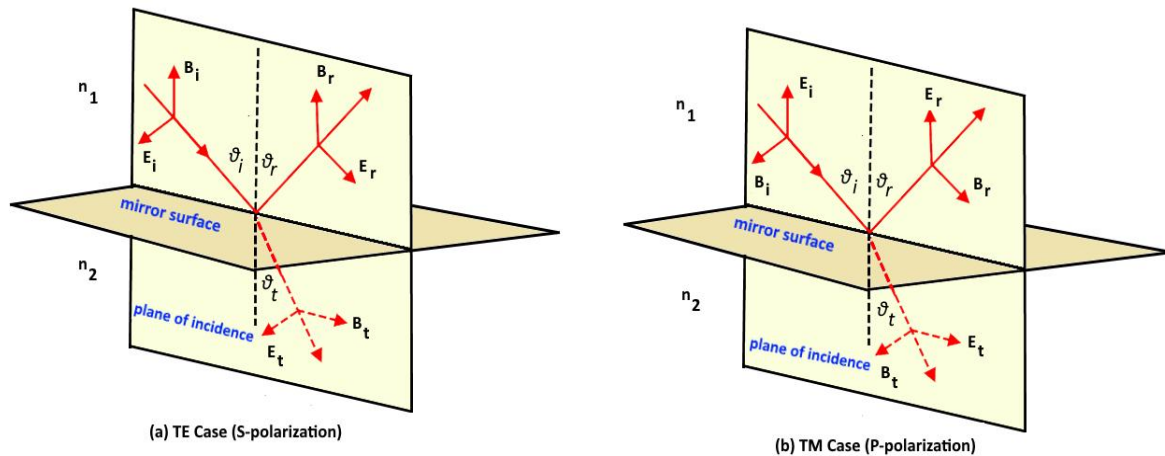


Figure 1.5. Plane wave incidents at the boundary between two homogeneous and isotropic media. (a) with the electric field perpendicular to the plane of incidence $E \perp$. (b) with the electric field parallel to the plane of incidence $E \parallel$.

As seen in Fig.1.5, there are two possible cases that could occur with the electric field vector of the incident wave; the electric field vector can be either perpendicular to the plane of incidence (a), or parallel to the plane of incidence (b). These two states are known respectively as Transverse Electric (TE) or s-polarization and Transverse Magnetic (TM) or p-polarization. It may worth to mention here that the letter s in “s-polarization” comes from to the initial of the word "senkrecht", which means the perpendicular component of the electric field.

The reflectivity is defined as the ratio of the reflected intensity to that incident at the interface between the two media. Applying the boundary conditions at the interface of Fig. 1.5 (a) for TE where $E \perp$ and $B \parallel$ will give the reflectance and transmittance for s-polarization. These can be described as:

$$R_s = \left| \frac{E_r}{E_i} \right|^2 = \left| \frac{n_1 \cos \theta_i - n_2 \cos \theta_t}{n_1 \cos \theta_i + n_2 \cos \theta_t} \right|^2 \text{ and} \quad 1.17$$

$$T_s = \left| \frac{E_t}{E_i} \right|^2 = \left| \frac{2n_1 \cos \theta_i}{n_1 \cos \theta_i + n_2 \cos \theta_t} \right|^2. \quad 1.18$$

Similarly, by applying the boundary conditions at the interface of Fig. 1.5 (b) for TM where $E \parallel$ and $B \perp$ will give the reflectance and transmittance for p-polarization, which could be also represented as:

$$R_p = \left| \frac{E_r}{E_i} \right|^2 = \left| \frac{n_2 \cos \theta_i - n_1 \cos \theta_t}{n_1 \cos \theta_t + n_2 \cos \theta_i} \right|^2 \text{ and} \quad 1.19$$

$$T_p = \left| \frac{E_t}{E_i} \right|^2 = \left| \frac{2n_1 \cos \theta_i}{n_1 \cos \theta_t + n_2 \cos \theta_i} \right|^2. \quad 1.20$$

The total reflection of un-polarized light can be found by combining the reflectivity due to the two different polarizations as:

$$R = \frac{R_s + R_p}{2}. \quad 1.21$$

The term “polarization” comes from the Greek word “polos” which means “orientation”. For that, the polarization of light is a specific orientation of the electric field in waves. The polarization

of light can be achieved by different mechanisms such as **reflection, scattering, dichroism and birefringence materials**. When un-polarized light crosses the interface between two different media at a certain angle of incidence, the reflected beam will be completely polarized depending on the incidence angle. The angle at which this occurs is called the polarizing angle or the Brewster angle θ_p and is given as [20] :

$$\tan\theta_p = \frac{n_2}{n_1} \quad 1.22$$

where n_1 and n_2 are the refractive indices of the two-media defining the reflecting surface. Fig. 1.6 shows the variation of the perpendicular s and parallel p components of the reflected light from SiO_2 substrate versus the incidence angles at wavelength 121.6 nm. The Brewster angle corresponds to the minimum reflectance of R_p .

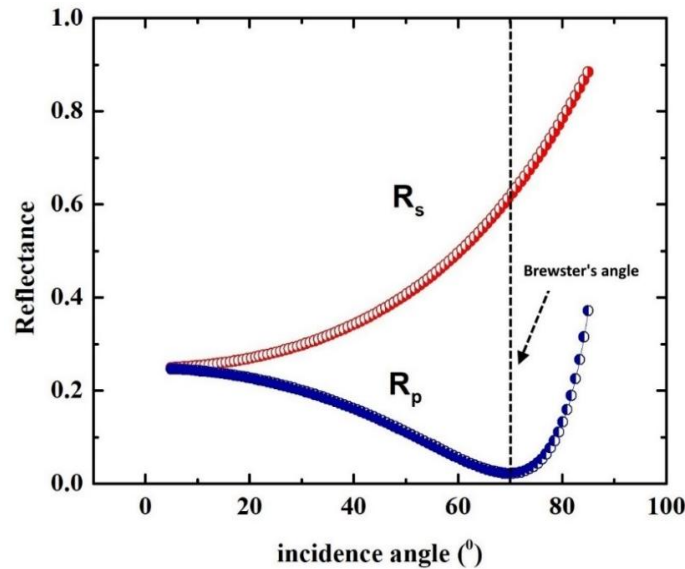


Figure 1.6. Calculated reflectance of a SiO_2 substrate for both polarization components of the reflectance versus the angle of incidence at 121.6 nm.

At the Brewster angle, most of the reflected beam is polarized with the electric vector perpendicular to the plane of incidence, which is defined by the incoming and outgoing beams [21]. This property opened the door for several applications which require knowledge of the polarization state of the light even not all materials show a characteristic behavior of Brewster angle property. This in turns has made the fabrication of mirrors, filters, polarizers and phase

retarders is highly required, although it needs proper designs, optimized deposition procedures as well as accurate selection of materials.

1.5. Optical Coatings for FUV-EUV Polarimetry

The development of optical components for polarization measurements in the far ultraviolet (FUV) and extreme ultraviolet (EUV) regions has experienced a rapid growth over the last decades. This has been motivated by the development of the 4th generation sources and new lithography arrangements working in the EUV spectral range [22], where the contrast between the lowest and highest intensity is considerably enhanced by using a linearly-polarized light source when compared with un-polarized ones. In this range, polarized light can be generated using large-scale facilities such as synchrotrons [23], and free electron lasers [24]. Due to the natural divergence of synchrotron radiation, the emitted radiation from the bending magnets is fully linearly polarized in the plane of the particle's orbit. In addition, the beamline is equipped with a polarization selector to select the radiation emitted on the orbit plane, i.e., with linear polarization, or out of the plane with elliptical polarization. The first reported measurements of synchrotron polarization were reported by Joos who confirmed the theoretical prediction of polarized light from the Cornell synchrotron [25].

The emission of the solar coronal plasma in the FUV-EUV spectral range and its impact on our life has fostered scientists to investigate and design new optical coatings for polarization measurements to study the coronal magnetic field. It is well known that fluorides behave as birefringent down to 130 nm [26], and have been used as transmissive polarizers working at their Brewster angles. Wollaston and Rochon prisms [27,28] are one of the common polarizers used in the FUV range; however, the extinction ratio of MgF_2 and LiF is insignificant especially at 121.6 nm. Multilayer coatings can be an alternative solution for delivering high polarization degree. *Kim et al.* [29] deposited three layers of (Al/MgF_2) on an Al substrate optimized for solar observation at 121.6 nm and 130.4 nm wavelengths. *Bridou et al.* [30] designed several coatings for optimum polarization performance at 121.6 nm based on (Al/MgF_2) multilayer. They also used a single pair of polarizing coatings of AlF_3 and of MgF_2 deposited on glass substrate tuned at 103.2 and 121.6 nm, respectively [31].

Even a single metal surface working at the Brewster angle of incidence is not enough for a high extinction coefficient. Multi-reflection mirrors polarizer can be designed for this purpose. *Hass and Hunter* [32] developed a three-reflection mirror polarizer combined Al/MgF_2 mirrors and a MgF_2 plate working close to Brewster angle. It had a good extinction efficiency ratio over a wide spectral range, but it had low reflectance for the s- component of the electric field. This, in turns, which resulted in moderate polarizer efficiency. *Yang et al.* proposed triple reflective mirror polarizers based on $Au/SiC/Au$, which can be working in a wide band including the FUV and shortwards [33].

Most of the previous work is based on fluoride as a major element for FUV-EUV polarizing mirrors despite the cut-off around 115 nm in case of MgF_2 and 106 nm in case of LiF , which limits their use in some cases. The most widely used materials for optical coating devices in FUV and EUV spectral range are shown in Fig.1.6. The gap between FUV and EUV region is a challenging problem that must be treated. This will be discussed through the Thesis.

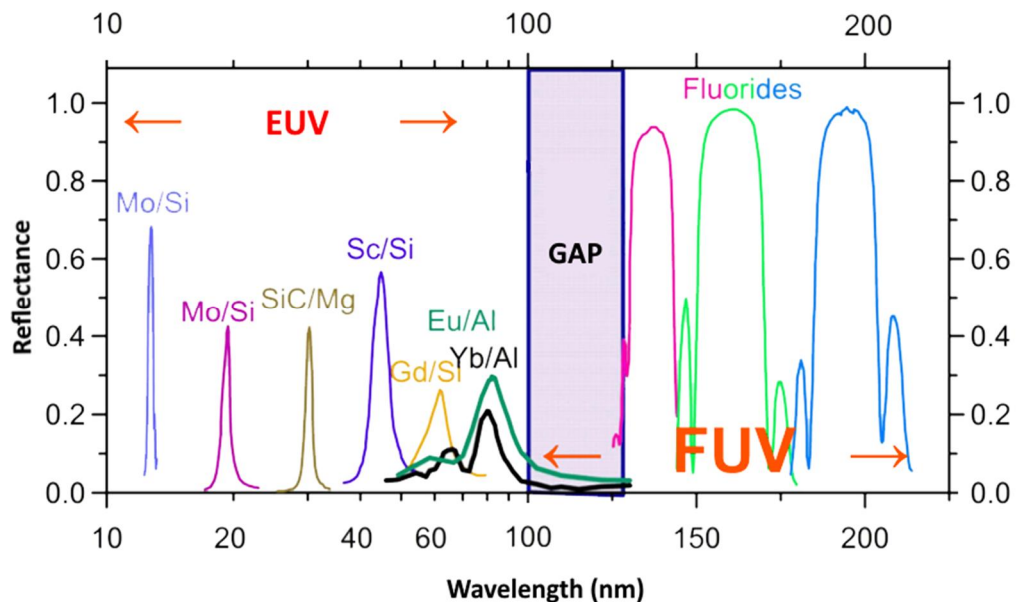


Figure 1.6. The most widely used materials for optical coatings in FUV and EUV range [34].

Polarization has led to numerous discoveries and applications in various scientific fields from materials science analysis to the more advanced techniques such as medical diagnosis and spectroscopic ellipsometry. Furthermore, circular dichroism spectroscopy [35] and magneto-optical spectroscopy [36] are only some of other examples requiring polarimetry. In the following

Section we will discuss the applications of FUV polarization related to space imaging and materials analyses.

1.6. EUV Polarimetry for Space Imaging

In space, polarimetry plays an important role in understanding the physical processes of the coronal plasma in energy transfer from the inner parts of the sun to outer space. The emission of the solar corona in the EUV spectral range has been widely investigated by various space instruments, such as TRACE, SOHO, SUMER and SDO [37]. These missions have accomplished an exceptional progress in understanding the behavior of the external solar atmosphere. However, more information on the coronal magnetic field is still not achievable due to shortage of knowledge about the polarization states. The most interesting spectral range that could be used in diagnosing solar magnetic fields, via the Zeeman and Hanle effects, are located between 90-160 nm. In this spectral range, many hydrogen emission lines are founded such the Lyman series of hydrogen and O VI line at 103.2 nm and C IV line at 154.8 nm [38].

The Zeeman effect is the most frequent phenomena used for coronagraphic observations; it involves alignments of polarization by way of the magnetic field. The interaction of the magnetic moment of the atom with an external magnetic field leads to splitting the energy levels of the atom to the close sublevels. For this reason, the spectral lines split into components with circular and linear polarization; however, its own polarization depends on the number of sublevels and the direction of the applied magnetic field. The Stokes vectors (I, Q, U, V) of spectral lines can be measured using Zeeman effect. This can be given as [39]:

$$Q(\lambda) = -\left(\frac{\mu B}{2hc} g_l \lambda^2\right)^2 \frac{\partial^2 I}{\partial^2 \lambda^2} B \sin^2 \gamma \cos 2\chi \quad 1.23$$

$$U(\lambda) = -\left(\frac{\mu B}{2hc} g_l \lambda^2\right)^2 \frac{\partial^2 I}{\partial^2 \lambda^2} B \sin^2 \gamma \sin 2\chi \quad 1.24$$

$$V(\lambda) = -\frac{\mu B}{hc} g_l \lambda^2 \frac{\partial I}{\partial \lambda} B \cos \gamma \quad 1.25$$

where μB is the Bohr magneton and g_l the Lande factor, χ and γ represent the azimuth and magnetic field deviation respectively.

It is more sensitive to circular polarization $V(\lambda)$ which is called longitudinal Zeeman effect and can derive valuable information about the orientation and strength of the magnetic field. In contrast to Zeeman effect, more information on the weak magnetic field can be obtained through Hanle effect in which the magnetic field induces a modification to the linear polarization caused by the scattering processes. Raouafi *et al.* [37] achieved the first detection of the Hanle polarization signal in the coronal plasma at the spectral line of *OVI* at 103.2 nm by means of SOHO spectrograph [40]. H Lyman β (102.6 nm) and Lyman- γ (97.3 nm) lines are also sensitive to weak magnetic fields. Such weak fields are expected out of active regions of the Sun.

It is of pivotal importance to know the state of the magnetic field to reveal the nature of the governing processes in the outer solar atmosphere. Therefore, for the first time, the solar magnetism explorer (SolmeX) will investigate the polarization state over a wide spectral range from the extreme ultraviolet to the infrared region [38]. It consists of five instruments dedicated to explore the magnetic field in different regions, as described in Table 1.1.

Table 1.1. Table 1.1. Expected instruments on-board SolmeX. explorer.

	Instruments	Spectral lines
CUSP	Coronal UV Spectro-polarimeter	95 nm -125 nm
VIRCOR	Visible light and IR coronagraph	400 nm- infrared
SUSP	Scanning UV Spectro-polarimeter	115 nm -160 nm
EIP	EUV imaging polarimeter	17.4 nm
ChroME	Chromospheric magnetic explorer	Mg IIk 279.6 nm

The mission is expected to be launched in 2022. The most important instruments for investigation of the magnetic field effects at FUV and EUV are the EUV imaging polarimeter (EIP) and Scanning UV Spectro-polarimeter (SUSP).

As shown in the table, SUSP is an effective normal incidence UV spectrometer with high throughput. It consists of a single parabolic mirror telescope attached with grating spectrograph

with a concave Variable Line Spacing (VLS) grating as described in Fig.1.7. It can measure various orientations of polarized light over wide spectral range from 115 nm to 160 nm by investigating the Stokes parameters.

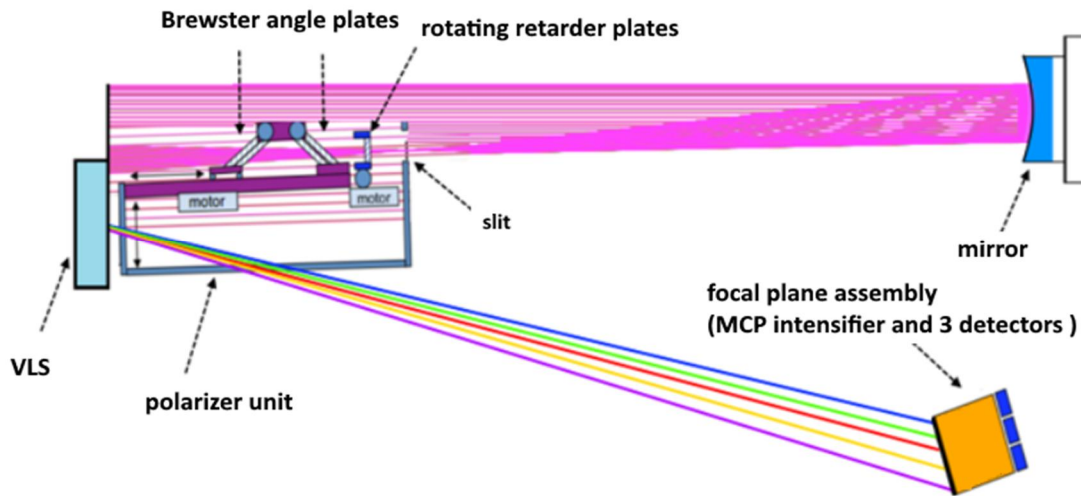


Figure 1.7. Scanning UV Spectro-polarimeter (SUSP) configuration highlighted with the main optical components. [38].

SUSP is attached with a transmissive polarizer placed between the entrance slit and the grating to measure the Stokes parameters. The polarizer consists of a rotating MgF_2 retarder plate and a double set of MgF_2 plates working at a Brewster's angle perpendicular to the dispersion plane. The polarizer can be removed from the optical path which in turns allows the measurements of non-polarizing mode. The reflected beam from the grating will be recorded by an anode phosphorous coating of the visible-blind MCP intensifier and then transferred by fiber optical couplers to three separate CMOS-APS detectors that work in photon counting mode.

1.7. EUV Spectroscopic Ellipsometry

Spectroscopic ellipsometry is one of the powerful techniques developed for material science analysis. The technique turned its way to science with the work presented by Paul Drude in the nineteenth century [41]. This work stimulated further investigations in a wide spectral range from the infrared (IR) to the near ultraviolet (UV) region [42,43]. Additionally, the rapid development in semiconductor industry, especially for high K electronics, has fostered to extend the

investigation down to shorter wavelengths in the far ultraviolet (FUV) and extreme ultraviolet (EUV).

The first achievement of ellipsometry measurements in the EUV spectral range has been realized at *Deutsches Elektronen-Synchrotron* (DESY) light source by *Schledermann* [44]. Since then, no further efforts have been made until the pioneering work was presented by *J.Barth et.al* at the BESSY storage ring [45]. In fact, the use of synchrotron radiation has enhanced great transition for further improvements of such techniques [46]. This has been followed by several approaches being used and several devices being implemented for measuring the polarization of EUV radiation at synchrotron light sources.

Today there is a very good understanding of ellipsometry principles, not only the mathematical representation but also the experimental realization. However, the most critical issue that makes EUV ellipsometry more difficult than conventional ellipsometry in the visible region is the strong absorption of EUV radiations due to their high energy photons. The overall structure of any ellipsometric system is like a spectrophotometer except that the emitted light is linearly polarized. Fig.1.8 shows the setup of an ellipsometry system where the beam coming from a specific light source is linearly polarized by an optical polarizer and refocused onto the sample under investigation. The polarization change of the reflected light is then analyzed by a second polarizer, which acts here as an analyzer. The transmitted intensity is collected by the detector afterwards

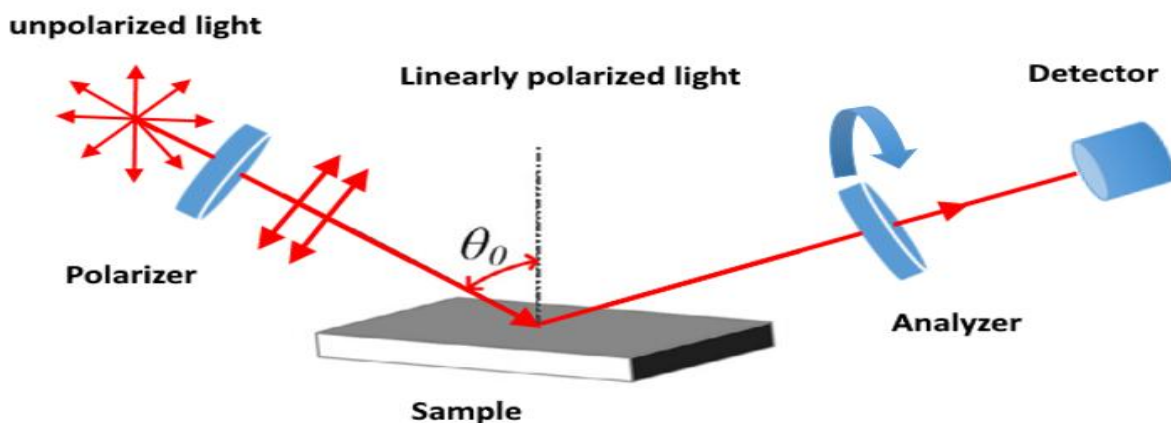


Figure.1.8. The setup of ellipsometry technique: the sample is illuminated with linearly polarized light; the reflected beam is analyzed by the second polarizer and the output intensity is collected with the detector.

In general, the principle of ellipsometry is based on the fact that the different polarization states of an electric field, parallel, E_p , and perpendicular, E_s , to the plane of incidence, are reflected with different intensities. In this sense, ellipsometry measures the change in the polarization state of the incoming beam upon reflection from the surfaces under investigation by introducing new expressions denoted by [47]:

$$\tan\psi = \frac{r_p}{r_s} \quad \Delta = \delta_p - \delta_s \quad 1.26$$

where ψ and δ are the ellipsometry parameters which represent the intensity ratio of the two orthogonal components of the electric field vector and the phase difference introduced by the sample under investigation.

1.8. Thesis Breakdown

The thesis consists of five chapters. The current chapter has introduced the nature of EUV radiations and their interaction with the matter along with the basic theoretical background. The history of polarized light and the application of EUV polarimetry has been also presented. Chapter 2 briefly introduces the mathematical representation of polarized light with more insight to the Mueller matrix formalism that has been adopted for the experiment carried out during this work. Chapter 3 presents an original implementation of the multi-angle EUV reflectometer facility for polarimetric analysis. This facility has been coupled with FUV-EUV linear polarizer to be used as a spectroscopic ellipsometer system. Chapter 4 introduces the setup for the facility calibration by characterizing the polarization degree of the beam delivered by the light source via the Stokes parameters formalism. Furthermore, application of the method to the characterization of Al/Si structure and non-uniform contamination layers due to the presence of Al_2O_3 is also discussed. Chapter 5 describes the experimental setup and data analysis of a reflective QWPs using innovative capping layers of $SnTe$ on top of aluminium specimen.

Chapter.2

Mathematical Representation of Polarized Light

The determination of the nature of light has a long history extending from the beginning of the seventeenth century when Christian Huygens suggested that light was not a scalar quantity; his assumption was based on the propagation of light through crystals; and after several investigations, Maxwell demonstrated that light is an electromagnetic wave [19]. However, the nature of polarized light remained undistinguishable until Fresnel reported that polarized light consists of two orthogonal components. Currently, there is a deeper understanding of the mathematical representation of polarized light. There are two mathematical models describing the polarization of light, the common model is based on Stokes vectors combined with the Mueller matrix formalism, while the other model is based on the Jones formalism [48]. However, the Mueller matrix formalism is the most general representation of the interaction of polarized light with materials and can account for any polarization states of light. In this chapter, we will briefly review the theoretical descriptions of the polarized light based on these two models with more insight to the Mueller formalism, which is adapted to the experiment carried out in this thesis.

2.1. The Polarized Light and Polarization Ellipse

As concluded by Fresnel's wave theory, the electric field vector E_0 of a plane electromagnetic wave traveling along z-direction can be characterized by two orthogonal components of E_x and E_y along x and y directions respectively [19]:

$$E_x(t, z) = E_{0x} \cos(\omega t - kz + \delta_x) \quad 2.1$$

$$E_y(t, z) = E_{0y} \cos(\omega t - kz + \delta_y) \quad 2.2$$

where E_{0x} and E_{0y} are the amplitudes of the electric field components, δ_x and δ_y are the relative phases of the components and ω is the wave angular frequency. As the electromagnetic wave propagates in space, the resultant electric vector E describes the locus of points in the xy plane which can be derived from a combination of the two equations, after some algebraic operations Eq. (2.1) and Eq. (2.2) will yield:

$$\frac{E_x^2(t)}{E_{0x}^2(t)} + \frac{E_y^2(t)}{E_{0y}^2(t)} - 2 \frac{E_x(t)}{E_{0x}(t)} \frac{E_y(t)}{E_{0y}(t)} \cos\delta = \sin^2\delta(t) \quad 2.3$$

where $\delta(t) = \delta_y(t) - \delta_x(t)$

Equation (2.3) is time-dependent and shows that once the observation plane is fixed along the z -axis, the locus of points of the electric field vectors describes an ellipse. Fig. 2.1 shows an ellipse encountered within a rectangle whose sides are parallel to the coordinate axes and whose lengths are $2E_{0x}$ and $2E_{0y}$.

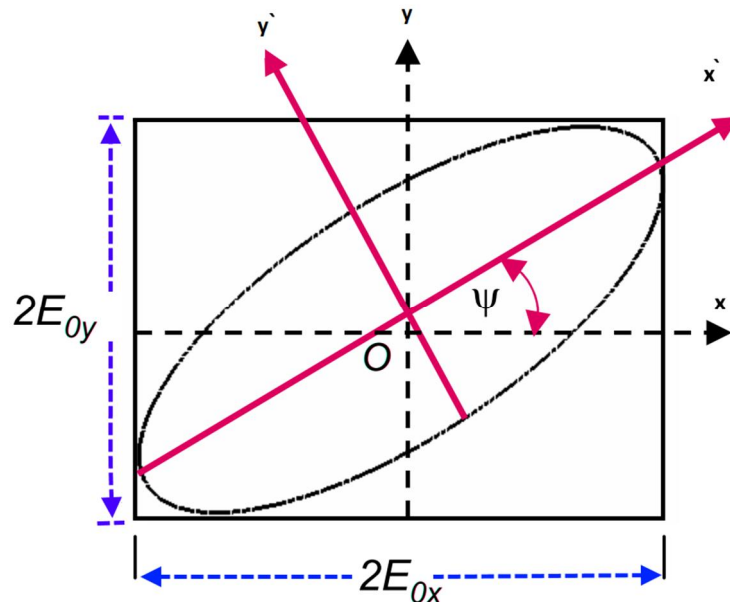


Figure 2.1. The polarization ellipse of a wave propagating in the z -direction; E_{0x} and E_{0y} are the amplitudes of the field oscillations along the x and y directions.

The figure shows also a rotated $x' - y'$ coordinate system with rotation angle ψ between Ox and the direction Ox' of the major axis. The rotated components E_x' and E_y' are

$$E_x' = E_x \cos \psi + E_y \sin \psi \quad 2.4$$

$$E_y' = -E_x \sin \psi + E_y \cos \psi \quad 2.5$$

An ellipse can be defined by two terms: the length of the minor and major axis, if $2a$ and $2b$ are the lengths of the major and minor axes, respectively, then the equation of the ellipse can be written in terms of Ox' and Oy' as

$$E_x' = a \cos(\omega t + \delta_x') \quad 2.6$$

$$E_y' = \pm b \sin(\omega t + \delta_y') \quad 2.7$$

where δ_x' and δ_y' is an arbitrary phase. The \pm sign describes the two possible cases in which the terminal point of the field vector can describe the ellipse. Equations (2.6) and (2.7) leads to the standard form of the ellipse,

$$\frac{E_x'^2}{a^2} + \frac{E_y'^2}{b^2} = 1 \quad 2.8$$

we can relate a and b regarding the parameters E_{0x} and E_{0y} as

$$(E_{0x}^2 - E_{0y}^2) \sin 2\psi = 2E_{0x}E_{0y} \cos \delta \cos 2\psi \quad 2.9$$

Equation (2.9) will give the orientation angle $0 \leq \psi \leq \pi$ of the polarization ellipse:

$$\tan 2\psi = \frac{2E_{0x}E_{0y} \cos \delta}{E_{0x}^2 - E_{0y}^2} \quad 0 \leq \psi \leq \pi \quad 2.10$$

another important parameter of interest is the angle of ellipticity which is defined as the ratio of the minor axis to the major axis of the ellipse, and given by

$$\sin 2\chi = \frac{2E_{0x}E_{0y} \sin \delta}{E_{0x}^2 + E_{0y}^2} \quad -\frac{\pi}{4} \leq \chi \leq \frac{\pi}{4} \quad 2.11$$

2.2. Stokes Representation of Polarized Light

The polarization ellipse is considered an idealization case of light behavior where the light is completely polarized, in contrast to the situation for the available light sources where light is very often un-polarized or partially polarized. These limitations have stimulated scientists to investigate an alternative description for representations of polarized light which accounts for partially or un-polarized light. In 1852, Gabriel Stokes overcome these limitations by introducing four measurable quantities describing any polarization state of light and known as the Stokes parameters [19]. In order to derive the Stokes parameters, it is mandatory to take the time average of the polarization ellipse equation (2.3) which will yield the form :

$$\frac{\langle E_x^2(t) \rangle}{E_{0x}^2} + \frac{\langle E_y^2(t) \rangle}{E_{0y}^2} - 2 \frac{\langle E_x(t)E_y(t) \rangle}{E_{0x}E_{0y}} \cos\delta = \sin^2\delta \quad 2.12$$

where the time average $\langle E_i(z, t)E_j(z, t) \rangle$ is defined by

$$\langle E_i(z, t)E_j(z, t) \rangle = \lim_{T \rightarrow \infty} \frac{1}{T} \int_0^T E_i(z, t)E_j(z, t) dt \quad i, j = x, y \quad 2.13$$

Where T is the total averaging time. Applying the definition given in equation (2.13) to the definition of the electric field vectors which was given in equations (2.1) and (2.2) will give average values of

$$\langle E_x^2(t) \rangle = \frac{1}{2} E_{0x}^2 \quad 2.14$$

$$\langle E_y^2(t) \rangle = \frac{1}{2} E_{0y}^2 \quad 2.15$$

$$\langle E_x(t)E_y(t) \rangle = \frac{1}{2} E_{0x}E_{0y} \cos\delta \quad 2.16$$

Then, Eq. (2.12) can be written after some algebraic manipulations as

$$(E_{0x}^2 + E_{0y}^2)^2 - (E_{0x}^2 - E_{0y}^2)^2 - (2E_{0x}E_{0y} \cos\delta)^2 = (2E_{0x}E_{0y} \sin\delta)^2 \quad 2.17$$

The quantities inside the parentheses can be rewritten individually as follows:

$$S_0 = E_{0x}^2 + E_{0y}^2 \quad 2.18$$

$$S_1 = E_{0x}^2 - E_{0y}^2 \quad 2.19$$

$$S_2 = 2E_{0x}E_{0y}\cos\delta \quad 2.20$$

$$S_3 = 2E_{0x}E_{0y}\sin\delta \quad 2.21$$

The four equations given in (2.18 – 2.21) are the Stokes polarization parameters for a plane electromagnetic wave. In some references, the Stokes parameters can be expressed in letter notation as (I, Q, U, V) . Where the first parameter I is the total irradiance of the light beam which is usually normalized to unity, the parameter Q describes the amount of horizontal or vertical linear polarization, the parameter U refers to the amount of $\pm 45^\circ$ linear polarization while V is the intensity difference between right and left circular polarization associated with the phase difference $\delta = \delta_x - \delta_y$ between the two electric field components. Thus, Eq.(2.17) can be expressed in terms of Stokes parameters as

$$S_0^2 = S_1^2 + S_2^2 + S_3^2 \quad 2.22$$

The Stokes parameters enable us to describe the degree of polarization P for any state of polarization by the definition,

$$P = \frac{\sqrt{S_1^2 + S_2^2 + S_3^2}}{S_0} \quad 2.23$$

where the value of $P = 1$ corresponds to completely polarized light, $P = 0$ corresponds to unpolarized light, and $0 < P < 1$ corresponds to partially polarized light.

The Stokes parameters can be expressed in terms of complex notation, one can start from the wave function solution of the electromagnetic wave; accordingly, the definition of the two electric field components E_x and E_y of an electromagnetic wave travelling along z direction can be represented as [48]:

$$E_x(t) = a_x e^{i(\omega t - kz + \delta_x)} = A_x e^{i(\omega t - kz)} \quad 2.24$$

$$E_y(t) = a_y e^{i(\omega t - kz + \delta_y)} = A_y e^{i(\omega t - kz)} \quad 2.25$$

Where $A_x = a_x e^{i\delta_x}$ and $A_y = a_y e^{i\delta_y}$ represent the complex amplitudes of the x and y components of a given beam. Thus, the four Stokes parameters can be expressed in terms of A_x and A_y as:

$$S_0 = \langle E_x E_x^* \rangle + \langle E_y E_y^* \rangle = \langle |A_x|^2 + |A_y|^2 \rangle \quad 2.26$$

$$S_1 = \langle E_x E_x^* \rangle - \langle E_y E_y^* \rangle = \langle |A_x|^2 - |A_y|^2 \rangle \quad 2.27$$

$$S_2 = \langle E_x E_y^* \rangle + \langle E_y E_x^* \rangle = \langle 2\text{Re}(A_x A_y^*) \rangle \quad 2.28$$

$$S_3 = \langle i(E_x E_y^* - E_y E_x^*) \rangle = \langle 2\text{Im}(A_x A_y^*) \rangle \quad 2.29$$

The Stokes parameters are usually arranged in a single column which is known as the Stokes vector for polarized light which have the form

$$S = \begin{bmatrix} S_0 \\ S_1 \\ S_2 \\ S_3 \end{bmatrix} \quad 2.30$$

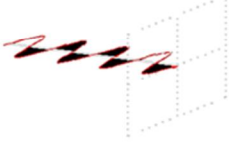
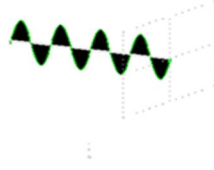

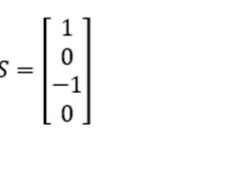
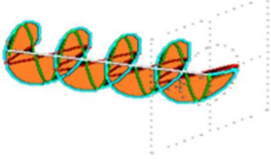
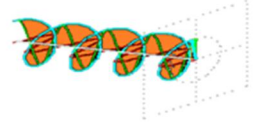
The Stokes vector for un-polarized light is defined as

$$S = \begin{bmatrix} 1 \\ 0 \\ 0 \\ 0 \end{bmatrix} \quad 2.31$$

Usually, the Stokes vectors identify the polarization state of the light in terms of intensity rather than the irradiance of the incoming beam; then, in this case, it is more convenient to use the normalized Stokes vector \hat{S} which is defined as

$$\hat{S} = \frac{S}{S_0} \quad 2.32$$

Where all the stokes parameters are divided by S_0 . Accordingly, the Stokes vectors for some common polarization states are readily found using the previous definitions as:

<p>Linear horizontal $E_{0y} = 0$,</p> $S = \begin{bmatrix} 1 \\ 1 \\ 0 \\ 0 \end{bmatrix}$ 	<p>Linear vertical $E_{0x} = 0$,</p> $S = \begin{bmatrix} 1 \\ -1 \\ 0 \\ 0 \end{bmatrix}$ 	<p>Linear at 45 $E_{0x} = E_{0y}, \delta = 0^\circ$</p> $S = \begin{bmatrix} 1 \\ 0 \\ 1 \\ 0 \end{bmatrix}$ 
<p>Linear at -45 $E_{0x} = E_{0y}, \delta = 180^\circ$</p> $S = \begin{bmatrix} 1 \\ 0 \\ -1 \\ 0 \end{bmatrix}$ 	<p>Circular right $E_{0x} = E_{0y}, \delta = 90^\circ$</p> $S = \begin{bmatrix} 1 \\ 0 \\ 0 \\ 1 \end{bmatrix}$ 	<p>Circular left $E_{0x} = E_{0y}, \delta = -90^\circ$</p> $S = \begin{bmatrix} 1 \\ 0 \\ 0 \\ -1 \end{bmatrix}$ 

2.3. Mueller Matrix Formalism

The beam emitted from a light source can be characterized in terms of its polarization which is described by the Stokes vector S . When the beam goes through an optical element its polarization can be modified and the incoming vector S is changed to a new output vector S' . The effect of the optical element is given by a 4×4 matrix which is known as the Mueller matrix, the representation is given by the relation:

$$S' = MS \quad 2.33$$

Where M is a 4×4 matrix which was introduced by Hans Mueller in 1943 [19]. The Mueller formalism can be extended to more complex optical systems, where an optical system can consist of several optical elements in series such as mirrors, polarizers, and retarders; and its equivalent Mueller matrix M_T is given by the product of the Mueller matrix of each optical element.

$$M_T = M_n M_{n-1} M_{n-2} \dots \dots M_{n-m} \quad 2.34$$

where with M_n and M_{n-m} are indicated respectively the Mueller matrices of the first and last component encountered by the incoming light beam.

2.3.1 Mueller Matrix of a Polarizer

A polarizer is an optical tool that attenuates the two orthogonal components of an optical beam unequally. The electric field components of the incoming E and outgoing E' beam is related by relationships:

$$E'_x = a_x E_x \quad 0 < a_x < 1 \quad 2.35$$

$$E'_y = a_y E_y \quad 0 < a_y < 1 \quad 2.36$$

where a_x and a_y are the attenuation coefficients of the transverse electric (TE) and magnetic (TM) amplitude respectively. Applying the obtained results in the definition of the Stokes parameters given in equations (2.18 – 2.21) after some algebraic manipulations will give the Mueller matrix of the polarizer as:

$$M_{\text{Polarizer}} = \begin{bmatrix} \frac{|a_x|^2 + |a_y|^2}{2} & \frac{|a_x|^2 - |a_y|^2}{2} & 0 & 0 \\ \frac{|a_x|^2 - |a_y|^2}{2} & \frac{|a_x|^2 + |a_y|^2}{2} & 0 & 0 \\ 0 & 0 & a_x a_y & 0 \\ 0 & 0 & 0 & a_x a_y \end{bmatrix} \quad 2.37$$

2.3.2 Mueller Matrix of a Phase Retarder

A retarder or phase shifter resolves a light wave into two orthogonal linear polarization components by producing a phase difference $\Delta\delta = \delta_y - \delta_x$ between them. Theoretically, the phase retarder element introduces a phase shift of $\frac{\delta}{2}$ along the x -axis and of $-\frac{\delta}{2}$ along the y -axis. These axes of the retarder are referred to as the fast and slow axes, respectively. The components of the emerging beam are related to the incident beam by the following relationships:

$$E_x' = a_x e^{\frac{\delta}{2}} E_x \quad 2.38$$

$$E_y' = a_y e^{-\frac{\delta}{2}} E_y \quad 2.39$$

Substituting with these conditions into the Stokes parameters definition (2.18 – 2.21) after some algebraic manipulations we find the Mueller matrix of a retarder is

$$M_R = \begin{bmatrix} \frac{|a_x|^2 + |a_y|^2}{2} & \frac{|a_x|^2 - |a_y|^2}{2} & 0 & 0 \\ \frac{|a_x|^2 - |a_y|^2}{2} & \frac{|a_x|^2 + |a_y|^2}{2} & 0 & 0 \\ 0 & 0 & |a_x||a_y|\cos\delta & |a_x||a_y|\sin\delta \\ 0 & 0 & -|a_x||a_y|\sin\delta & |a_x||a_y|\cos\delta \end{bmatrix} \quad 2.40$$

2.3.3 Mueller Matrix of an Optical Rotator

In order to change the polarization state of an optical field, a rotator device is needed which rotates the orthogonal components of the polarization ellipse E_x and E_y by an angle θ . Considering the coordinate system defined in Fig. 2.2 where the electric field vector E_x is rotated by angle θ to E'_x and E_y to E'_y , similarly β define the angle between the initial position of vector E and axis x .

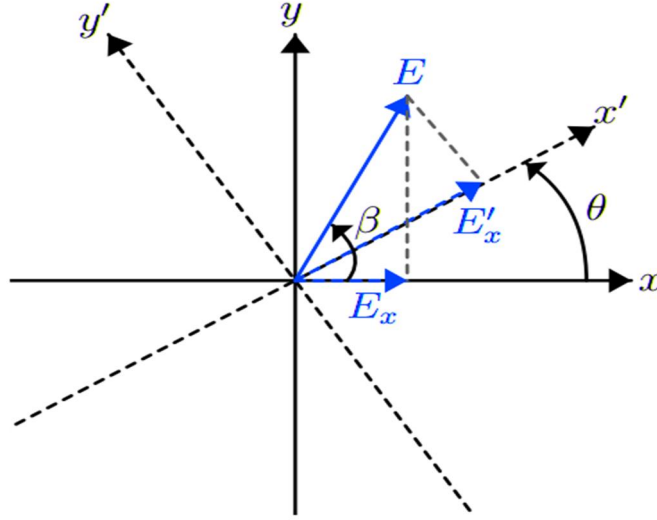


Figure 2.2. Rotation of the optical field components through a cartesian rotation.

The component of the optical field E can be analyzed to two components along x and y axis.

$$E_x = E \cos \beta \quad 2.41$$

$$E_y = E \sin \beta \quad 2.42$$

If the coordinate system x and y rotated by angle θ then, the electric field vector will be expressed as

$$E'_x = E \cos(\beta - \theta) \quad 2.43$$

$$E'_y = E \sin(\beta - \theta) \quad 2.44$$

After some algebraic manipulation by expanding the trigonometric functions of equations (2.43, 2.44) will give.

$$\hat{E}_x = E_x \cos\theta + E_y \sin\theta \quad 2.45$$

$$\hat{E}_y = E_y \cos\theta - E_x \sin\theta \quad 2.46$$

Applying the definition given in equations (2.45) and (2.46) to the definition of the Stokes parameters given in equations (2.18 – 2.21) will give the form of the rotation matrix.

$$M(2\theta) = \begin{pmatrix} 1 & 0 & 0 & 0 \\ 0 & \cos 2\theta & \sin 2\theta & 0 \\ 0 & -\sin 2\theta & \cos 2\theta & 0 \\ 0 & 0 & 0 & 1 \end{pmatrix} \quad 2.47$$

2.4. Jones Representation of Polarized Light

Although, the Mueller matrix formalism and Stokes vectors are not widely used in representations of polarized light, in 1940, R. Jones proposed a model capable of representing polarized light by reducing the degree of complexity associated with the Mueller calculus [49]. However, Jones' formalism can be applied only in case of fully polarized light, it doesn't capable to describe even partially or unpolarized light. The Jones formalism uses two complex vectors that describe the polarization state of light known as Jones vectors, and Jones matrices, its 2×2 matrices that describe optical elements. As described before, the electric field vector of arbitrarily polarized light can be described in terms of complex notation for two orthogonal linearly polarized components as

$$E_x = E_{0x} e^{i\delta_x} \quad 2.48$$

$$E_y = E_{0y} e^{i\delta_y} \quad 2.49$$

Equations (2.48) and (2.49) can be written in a form of a vector E which is known as Jones vector.

$$E = \begin{pmatrix} E_x \\ E_y \end{pmatrix} = \begin{pmatrix} E_{0x} e^{i\delta_x} \\ E_{0y} e^{i\delta_y} \end{pmatrix} \quad 2.50$$

An optical component of a given system can be represented by Jones formalism in a matrix form which is known as the Jones matrix $[J]$.

$$J = \begin{pmatrix} J_{xx} & J_{xy} \\ J_{yx} & J_{yy} \end{pmatrix} \quad 2.51$$

Thus, the polarization state E' of a wave transmitted by an optical system, described by the Jones matrix $[J]$, can be written in the following form.

$$\begin{pmatrix} E'_x \\ E'_y \end{pmatrix} = \begin{pmatrix} J_{xx} & J_{xy} \\ J_{yx} & J_{yy} \end{pmatrix} \begin{pmatrix} E_x \\ E_y \end{pmatrix} \quad 2.52$$

Where the column vector components E_x and E_y represent the initial polarization state of the wave.

As in the case of the Mueller Matrix, the representation of the Jones matrix can be extended to several optical devices with the series of the corresponding Jones matrices J_1 and J_2 , and the output polarization state will be given by

$$E' = J_1 J_2 E \quad 2.53$$

2.4.1 Jones Matrix of a Polarizer

Similarly to the Mueller matrix representation of optical polarizer, a polarizer element is characterized by the relations

$$E'_x = P_x E_x \quad 2.54$$

$$E'_y = P_y E_y \quad 2.55$$

Where $P_{x,y}$ represent the attenuation due to the optical element for the field components along x and y axes, equations (2.54) and (2.55) can be written in terms of Jones vectors as

$$\begin{pmatrix} E_x \\ E_y \end{pmatrix} = \begin{pmatrix} P_x & 0 \\ 0 & P_y \end{pmatrix} \begin{pmatrix} E_x \\ E_y \end{pmatrix} \quad 2.56$$

The polarizer behaves ideally if it has a complete transmission along only one axis and no transmission along the other axis. For an ideal polarizer with a complete transmission along the x axis, the Jones matrix can be expressed as

$$J_{LHP} = \begin{pmatrix} 1 & 0 \\ 0 & 0 \end{pmatrix} \quad 2.57$$

Similarly, for a linear vertical polarizer, the Jones matrix is

$$J_{LVP} = \begin{pmatrix} 0 & 0 \\ 0 & 1 \end{pmatrix} \quad 2.58$$

In a similar manner to the Mueller matrix, the Jones matrix for a rotator can be expressed as

$$J = \begin{pmatrix} \cos\theta & \sin\theta \\ -\sin\theta & \cos\theta \end{pmatrix} \quad 2.59$$

2.4.2 Jones Matrix of a Phase Retarder

In the same way, the Jones matrix for retarder can be expressed in the Jones formalism as

$$J_R(\delta) = \begin{pmatrix} e^{i\frac{\delta}{2}} & 0 \\ 0 & e^{-i\frac{\delta}{2}} \end{pmatrix} \quad 2.60$$

The two most common types of phase retarders are the quarter-wave retarder and the half-wave retarder with phases of $\delta = \frac{\pi}{2}$ and π respectively and have the form of Jones Matrix as

$$J_{QWR}\left(\frac{\pi}{2}\right) = \begin{pmatrix} e^{i\frac{\pi}{4}} & 0 \\ 0 & e^{-i\frac{\pi}{4}} \end{pmatrix} = e^{i\frac{\pi}{4}} \begin{pmatrix} 1 & 0 \\ 0 & -i \end{pmatrix} \quad 2.61$$

$$J_{HWR}(\pi) = \begin{pmatrix} e^{i\frac{\pi}{2}} & 0 \\ 0 & e^{-i\frac{\pi}{2}} \end{pmatrix} = i \begin{pmatrix} 1 & 0 \\ 0 & -1 \end{pmatrix} \quad 2.62$$

Chapter.3

Multi-Angle FUV-EUV Ellipsometry

Spectroscopic ellipsometry has taken a considerable attention in material science analyses due to its favorable advantages in structural characterization of thin films and optical coating developments [50]. In the visible and the UV spectral regions, several configurations are available for such measurements, most of them share some common optical elements such as polarizers and quarter wave retarders (QWR) [50]. The work carried out in this thesis have been done using different equipment and experimental techniques, which will be described throughout this chapter. The first part of this chapter presents an EUV reflectometer facility implemented for the polarimetric measurements over 90-160 nm spectral range. The monochromator facility located in the Institute for Photonics and Nanotechnologies-CNR Padua (Italy) was upgraded by coupling an FUV-EUV linear polarizer. The second part of this chapter discusses the design and performance of the optical polarizer.

3.1. The FUV-EUV Normal Incidence Reflectometer

The normal incidence reflectometer facility gives the possibility of different measurements such as transmittance and reflectance over a wide spectral range from (FUV) to (EUV). A schematic diagram of the facility is shown in Fig. 3.1. It consists of a 600 groove/mm toroidal Pt-coated grating with a main radius of 0.5 m at a subtended angle of about 25° between the entrance and the exit slits. A toroidal mirror working at a 45° incidence angle reflects the monochromatic radiation to the sample placed in the experimental chamber together with the detector. The sample and detector located in the experimental chamber are mounted on a rotating stage with suitable

holder in order to adjust the alignment and to change the incidence angle. The beam impinging on the sample is partially linearly polarized due to the geometrical arrangements of the diffraction grating and the toroidal mirror and is gathered by the channel electron multiplier type (CEM KBL10/90) manufactured by Sjuts Optotechnik [51].

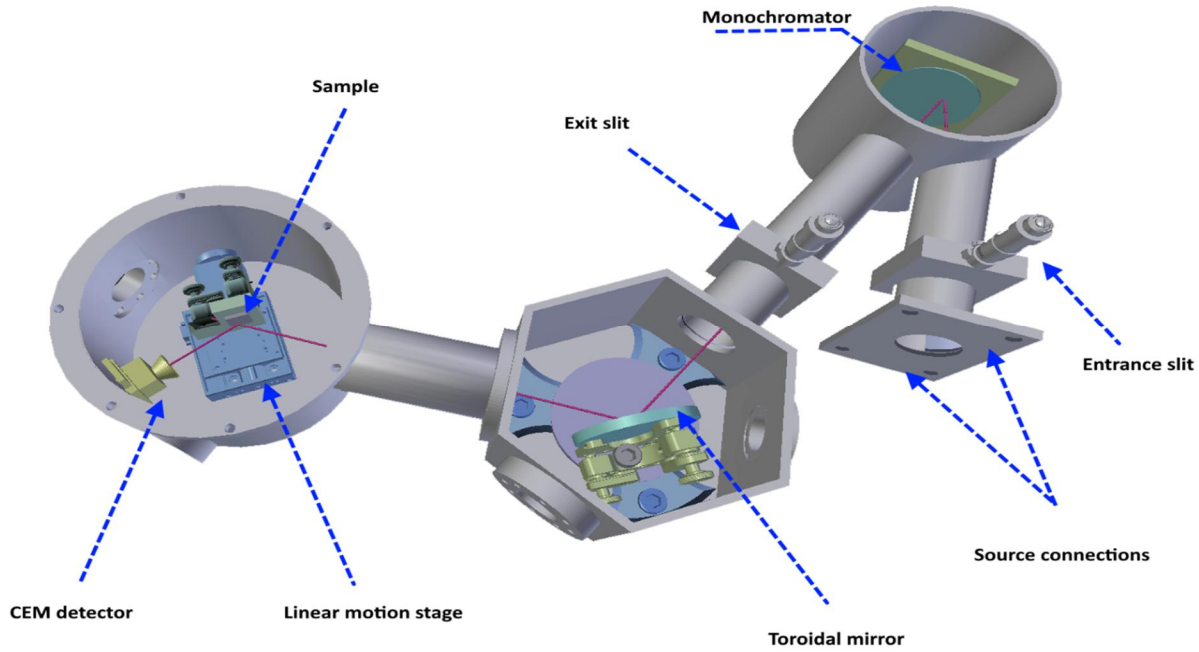


Figure 3.1. Structure of the FUV-EUV normal incidence reflectometer facility located in LUXOR, Padova, Italy.

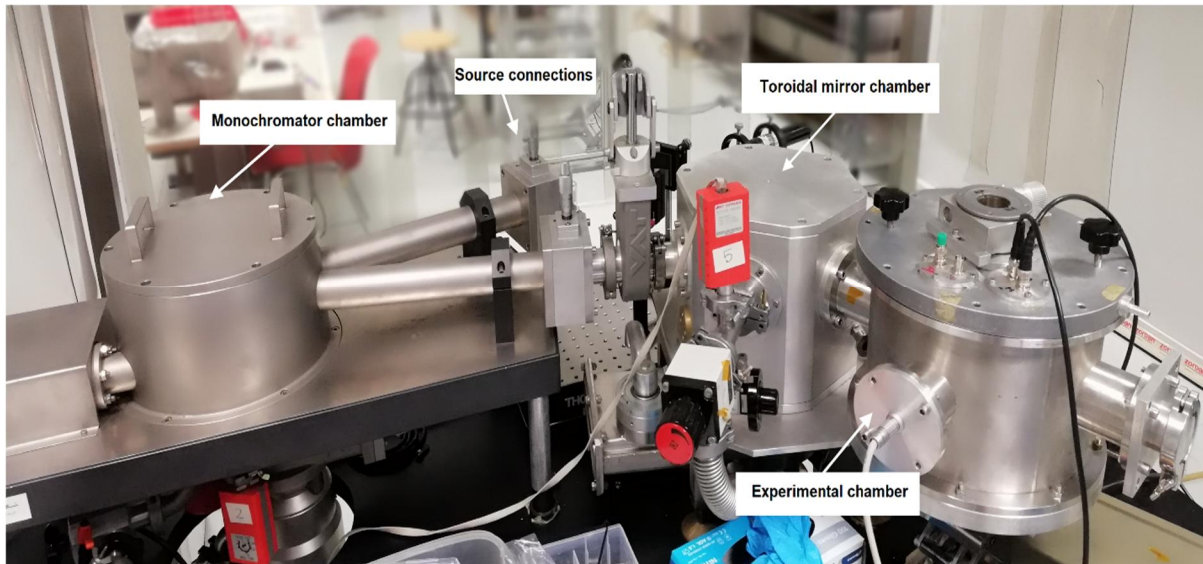


Figure 3.2. Photo of the developed table-top FUV-EUV normal incidence reflectometer facility.

3.2. FUV- EUV Radiation Source

The availability of different light sources gives the possibility to access many spectral ranges from FUV to EUV. In the presented work, the FUV radiation was produced by a deuterium lamp with a MgF_2 window emitting a strong 121.6 nm line superimposed on a spectrally continuous weaker emission [52]. However, other light sources such as Hollow cathode lamp (HCL) can be used to cover the shorter wavelengths in EUV region down to 30 nm.

3.2.1 Hollow Cathode Lamp

The hollow cathode lamp emits lines with adequate spectral purity and intensity [53]. The plasma occurs between two electrodes through a gas discharge. For the reflectometer facility, a homemade hollow cathode lamp (HCL) has been designed at Luxor laboratory [54]. A schematic diagram of the designed lamp is shown in Fig. 3.3. The lamp consists of two terminals acting as electrodes placed inside a cylindrical glass tube. The tube is filled with desired working gases according to the required spectral line emission. A direct voltage source applied between the two electrodes causes ionization of the gas and plasma formation. The gas ions are accelerated toward the cathode and sputter atoms from its surface. Both the gas ions and the sputtered cathode atoms are excited by collisions with each other and with electrons in the plasma medium. The excited gas atoms lose their energy in the form of photons at wavelengths depending on the gas used.

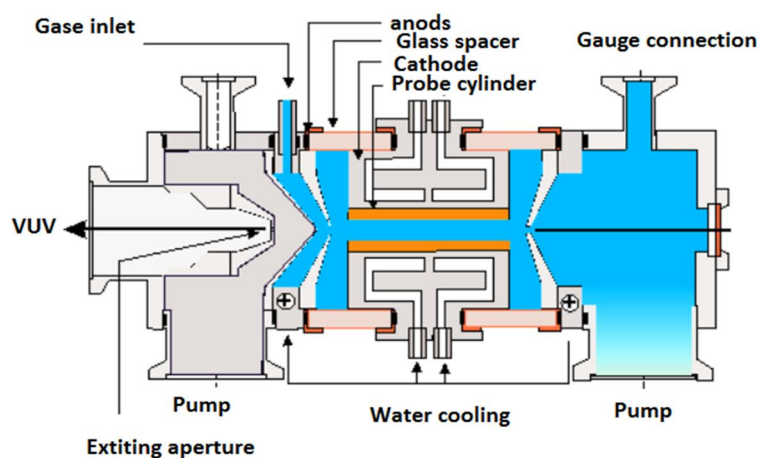


Figure 3.3. The layout of the hollow cathode lamp designed at Luxor laboratories in CNR Padua, Italy [55].

3.2.2 Deuterium lamp

The deuterium lamp is a continuous radiation source filled with a deuterium gas D_2 which emits an intense and continuous spectrum in the range between 115 and 400 nm depending on the transmissive window [52]. The lamp includes a heated tungsten filament cathode and thermionic anode both are placed together in a nickel box with a tiny aperture size. An arc discharge current excites the molecules of the deuterium gas to a higher energy state. The excited atoms relax back to the ground state losing energy in the form of light. The structure of the deuterium lamp is shown in Fig.3.4. The lamp comes with different types of transmissive windows such as fused quartz, UV glass, or Magnesium Fluoride depending on the expected applications and working temperature.

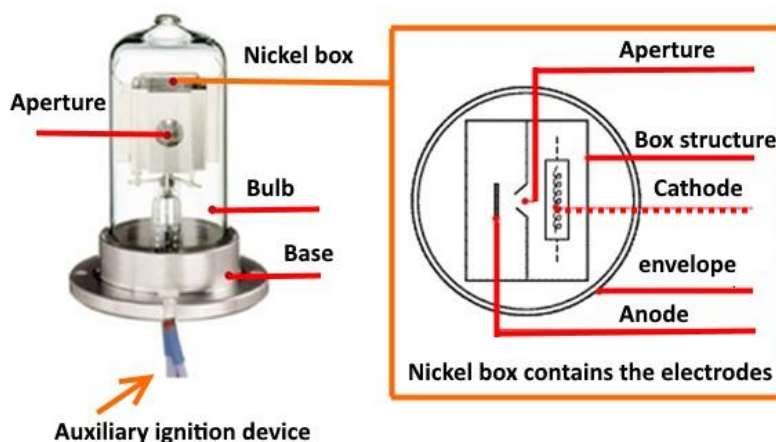


Figure 3.4. The structure of a typical deuterium lamp.

In our experiment, the FUV radiation was produced by a deuterium lamp manufactured by Hamamatsu [52]. The lamp comes with Magnesium Fluoride window with an aperture size of 0.5 mm that provides high resolution and high throughput radiation. The spectral distribution of the lamp with different transmissive windows is shown in Fig. 3.5. The lamp shows two characteristic peaks corresponding to emission lines; 121.6 nm and 160 nm in case of MgF_2 window. When wavelengths longer than 200 nm are required, silica and glass window can be used [52].

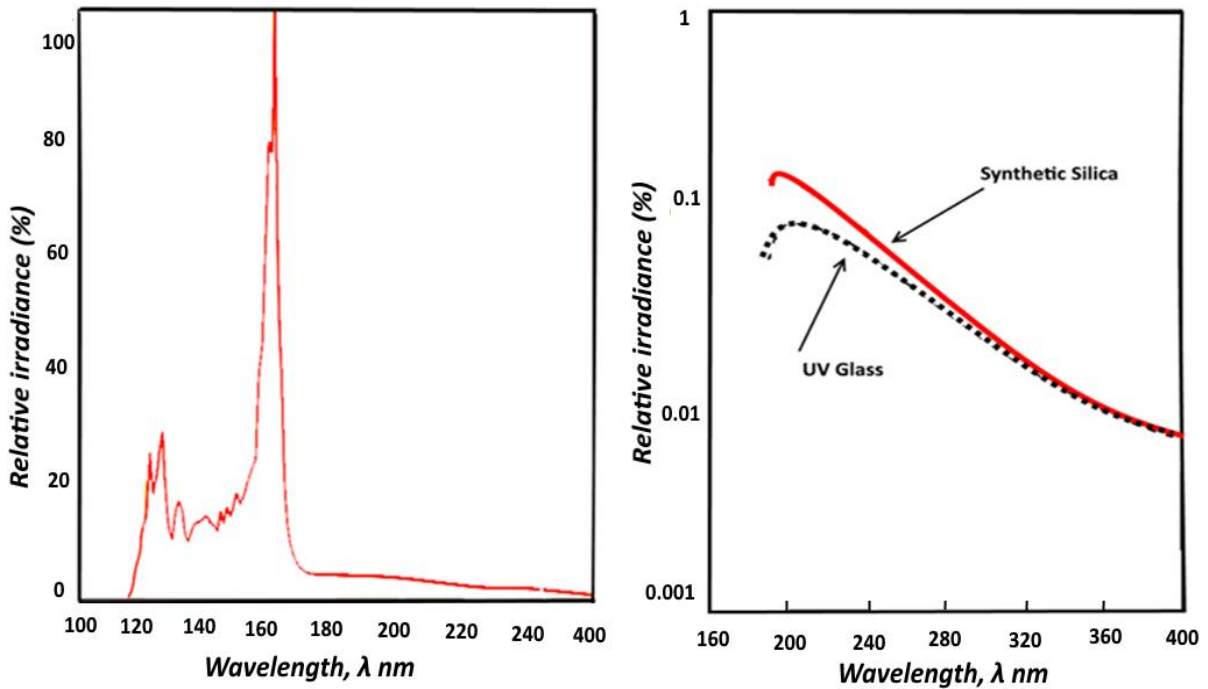


Figure 3.5. The spectral distribution of the deuterium lamp used with different transmissive windows.

The lamp is operated with a DC power supply model C9595 from Hamamatsu[52]. The power supply gives an output voltage between 85 and 90 V with a current intensity of 4 A. The current is raised slowly to reach the specified value in about 20 sec until the filament warm-up occurs. After being turned on, the lamp is allowed to stabilize, typically for about 20 min, while the lamp current is maintained at the specified value. The emission of FUV and EUV radiation requires working in an ultrahigh vacuum system, thus the deuterium lamp comes with a housing box which can be connected directly to the facility.

3.3. The Channel Electron Multiplier Detector (CEM)

Channel Electron Multipliers (CEMs) are detectors working with high efficiency over a wide spectral range from the soft x-rays to the vacuum ultraviolet spectral regions. Fig. 3.6 (a) shows the CEM detector as the incident radiation passes through the cone-shaped inlet and strikes the resistive surface of the detector. The resistive surface emits secondary electrons when impinged by primary charged particles. Accordingly, a single photon or particle can produce a cloud of electrons. The electron cloud is accelerated towards the anode under the effect of magnetic field;

then output pulses can be detected easily afterwards by using a preamplifier and a detector or as an input current in analog mode. A cross-section view of the CEM detector is shown in Fig.3.6 (b) where the generated electrons follow the tunnel so as to be collected by the anode.

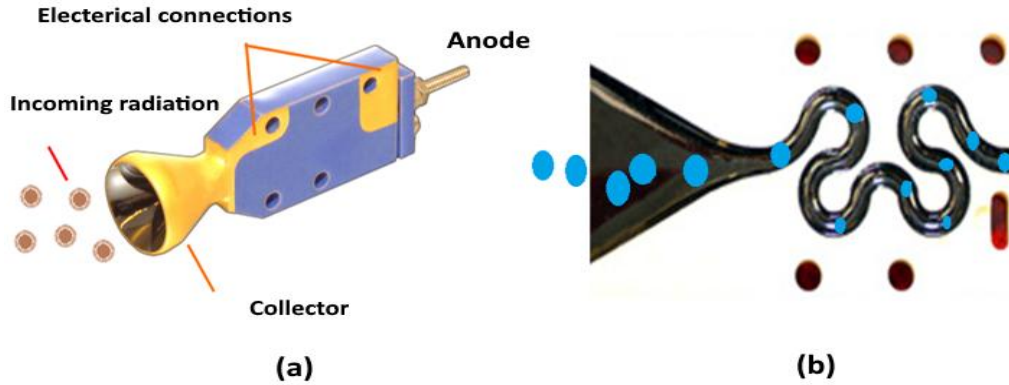


Figure 3.6. (a) Channel electron multiplier, (b) cross-section view of the CEM detector showing its working principle.

A potential difference between the detector terminals is required to accelerate the created electrons toward the anode. If the magnitude of the applied voltage has a sufficient value, the accelerated electron acquires enough energy to trigger more secondary electrons. Fig. 3.7 shows the electrical connection for a negative applied voltage with a typical resistor that should have a value of approximately $\frac{1}{25}$ of the wall resistance of the CEM detector.

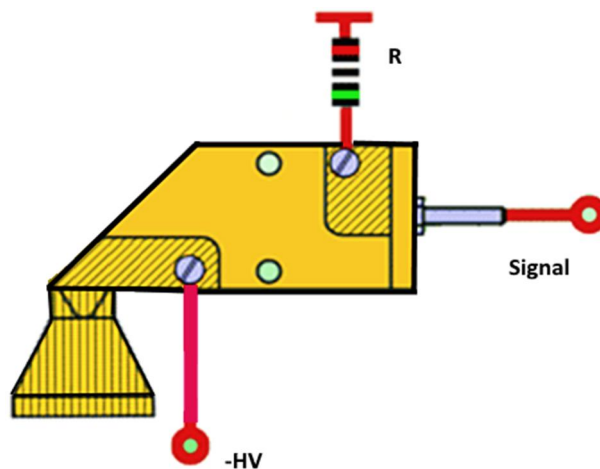


Figure 3.7. The connection to the CEM detector with a negative applied voltage using a resistor [51].

The detector was mounted inside a Teflon body to avoid any short circuit between the detector and the wall of the experimental chamber. The detector is mounted on a movable holder in a $\theta - 2\theta$ configuration to allow measurements at different angles of incidence. All the system is attached to the cover of the measuring chamber. Table 3.1 shows some working spectral lines achieved with the facility.

Table 3.1. A list of some working spectral lines at CNR with the filled gases and the used detectors [56].

Wavelengths nm	Source Type	Element	Detector
30.4	Hollow Cathode	He	CEM
46.1	Hollow Cathode	Ne	CEM
58.4	Hollow Cathode	He	CEM
73.6	Hollow Cathode	Ne	CEM
74.4	Hollow Cathode	Ne	CEM
91.9	Hollow Cathode	Ar	CEM
102.5	Hollow Cathode	He	CEM
121.6	Deuterium lamp	D2	CEM
123.3	Deuterium lamp	D2	CEM
140.0	Deuterium lamp	D2	CEM
160	Deuterium lamp	D2	CEM

3.4. Opto-Mechanical Design of the FUV-EUV Polarizer

Polarizers are the key elements in any polarimetric instrument. In order to characterize the polarization state of the beam delivered by our reflectometer facility, we manufactured a linear polarizer working within a suitable range between 80-160 nm.

In the visible range, the availability of commercial optical components such as polarizers are existed; however, in EUV spectral ranges, the choices for available coating materials are quite

limited since the materials become highly absorptive. A single metal surface at the Brewster angle of incidence is not enough for reaching a high degree of polarization. Accordingly, a four-reflection linear polarizer has been designed using gold-coated mirrors. We selected gold as a reflective coating because it is a good reflector in this range. It is very stable in the ambient environment and their optical constants are well known. The gold mirrors consist of 200 nm thick films deposited by thermal evaporation on a Si substrate. For a good adhesion of the gold, a 3-nm layer of chromium was e-beam evaporated between the substrate and the film. The design ensures that the performance of the polarizer is relatively good even over an extended spectral range from 60 nm to 160 nm. The calculated spectral reflectance, R_s , and R_p , for different materials, suitable as reflective coatings for the FUV and EUV linear polarizer, are presented in Fig. 3.8. The reflectance has been simulated at incidence angle of 60° from normal assuming the optical constants of Palik [57].

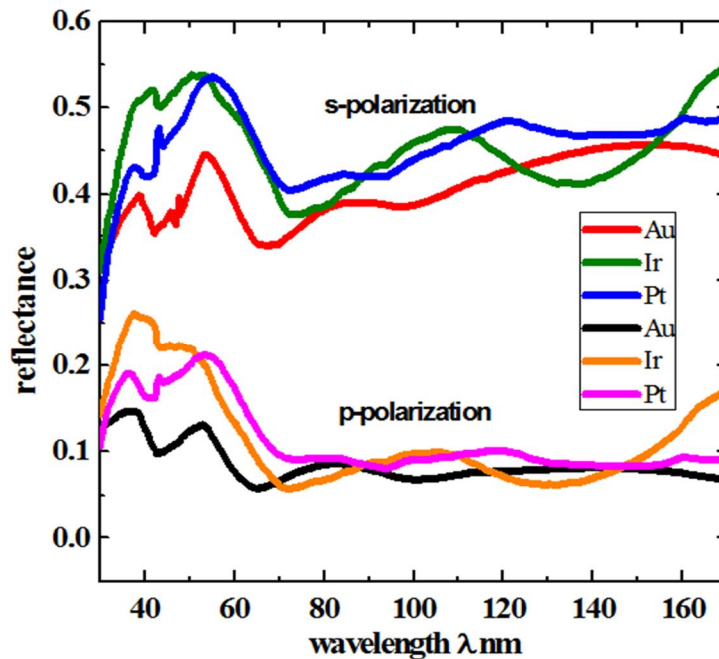


Figure 3.8. The calculated spectral reflectance R_s and R_p for un-polarized incidence beam at a normal incidence angle of 60° of Au, Ir and, Pt with 200 nm thickness on a Si substrate.

As confirmed by Fig. 3.9, shown below, the gold-coated mirrors work properly with a relatively good extinction ratio over the spectral range from 60 nm to 160 nm. However, it can be

extended to wavelengths shorter than 60 nm although they show reduced performance. Fig. 3.10 shows the extinction ratio of the gold-coated mirror for some important spectral emission lines for space exploration. The highest extinction ratio is for a working incidence angle of 60°.

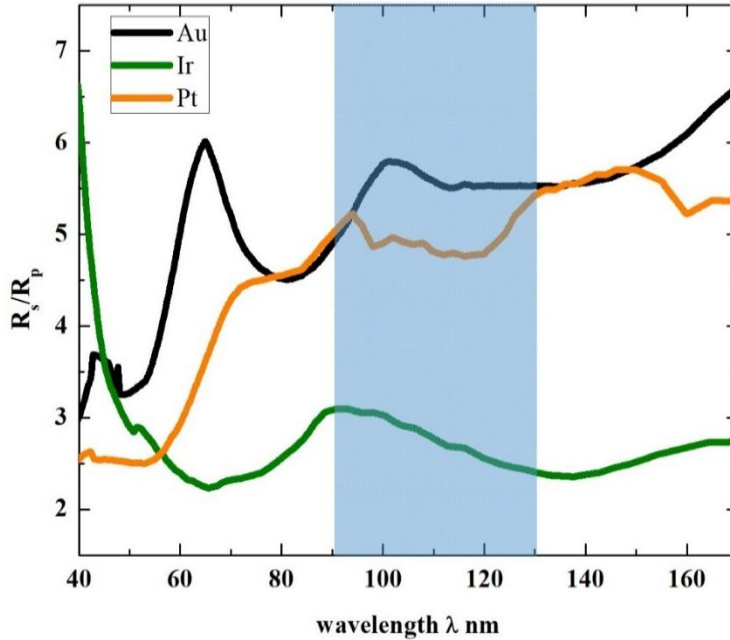


Figure 3.9. The ratio $\frac{R_s}{R_p}$ of Au, Ir and Pt coatings of 200 nm thickness on a Si substrate

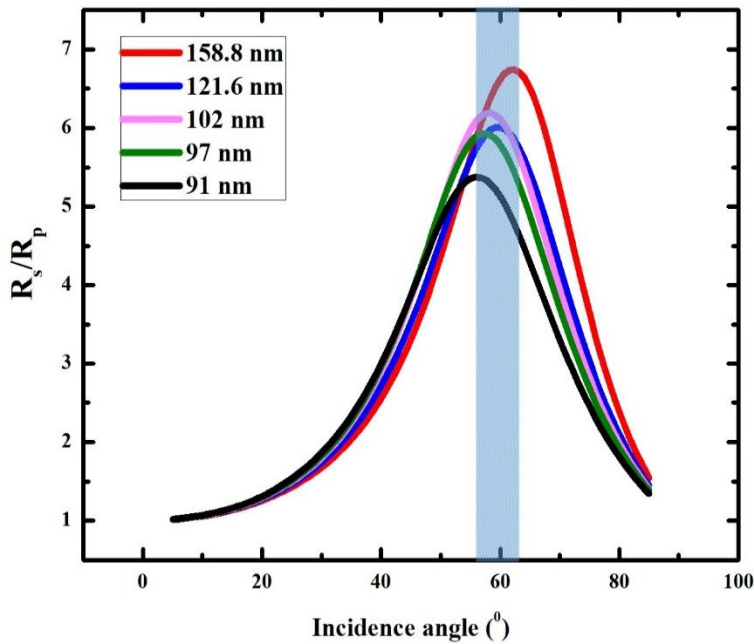


Figure 3.10. The ratio $\frac{R_s}{R_p}$ of a 200 nm gold mirror on a Si substrate for some wavelengths.

The polarization degree is usually defined by the effectiveness of a polarizer in providing linearly polarized light along a given direction of the electric field. This can be defined as [58]:

$$P = \frac{R_s - R_p}{R_s + R_p} \quad 3.1$$

The polarization degree is usually expressed as a positive value, and the optimum polarizer would have $P = 1$ for fully linearly polarized light. A contour plot of the polarization degree for the designed polarizer is shown in Fig.3.11 as a function of wavelength and the incidence angle. The more remarkable areas are those where P is larger than 0.95.

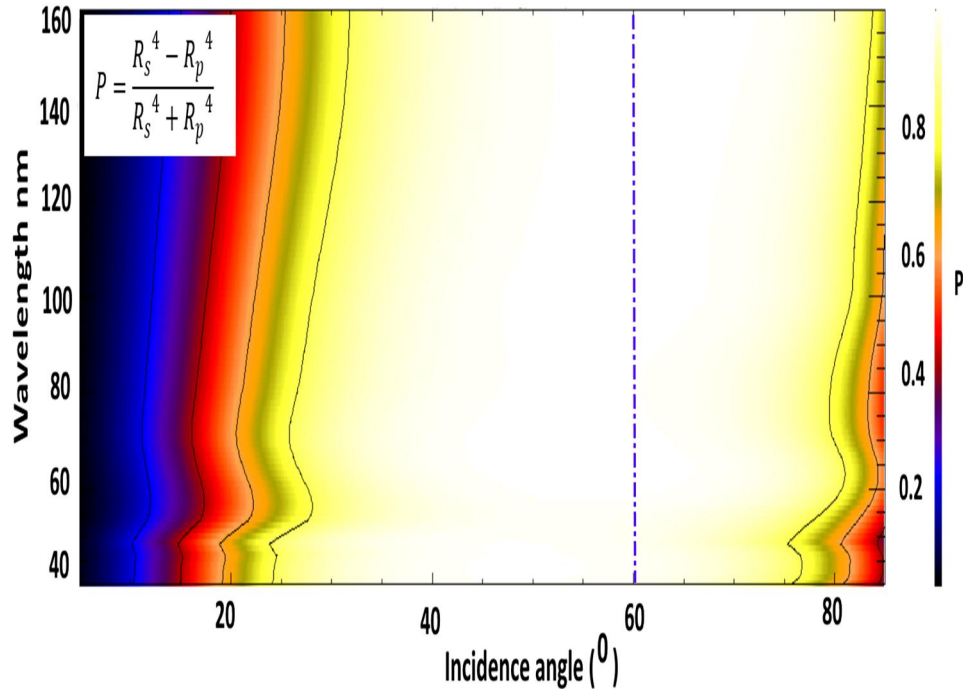


Figure 3.11. Contour plot of polarization degree of four reflection gold-coated mirror polarizer as a function of wavelength and normal incidence angle. The dashed line represents the working incidence angle at 60° .

In order to preserve the propagation direction of the incident beam after reflection, a special holder has been manufactured for mounting the two pairs of parallel mirrors. A schematic diagram of the polarizer design is shown in Fig. 3.12. It consists of four parts that can be assembled together using screws.

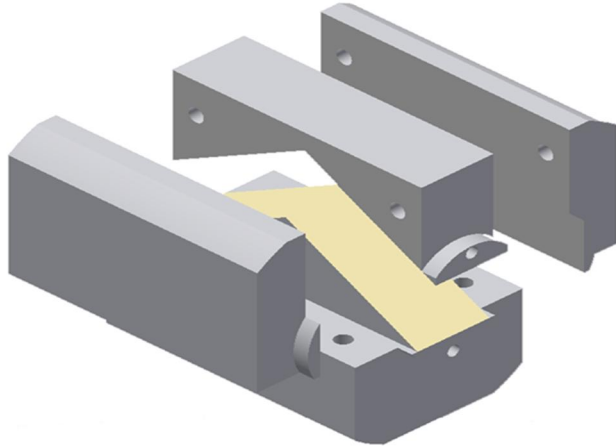


Figure 3.12. 3D design of the four-reflection linear polarizer consisting of four parts assembled together.

The gold mirrors, having a dimension of $10\text{ mm} \times 32\text{ mm}$, are mounted with 60° incidence angle from normal, as shown in Fig.3.13(a). The mirrors mounting system consists of two halves where the four mirrors are glued on four plane reference surfaces, as it appears in Fig.3.13(b). The device is mounted on vacuum compatible rotational stage with minimum angular step size of 0.0025° [59]. The total assembly of the polarizer combined with the rotation stage is shown in Fig. 3.13c. The transmitted beam intensity was collected by the channel electron multiplier (CEM), as has been already specified.

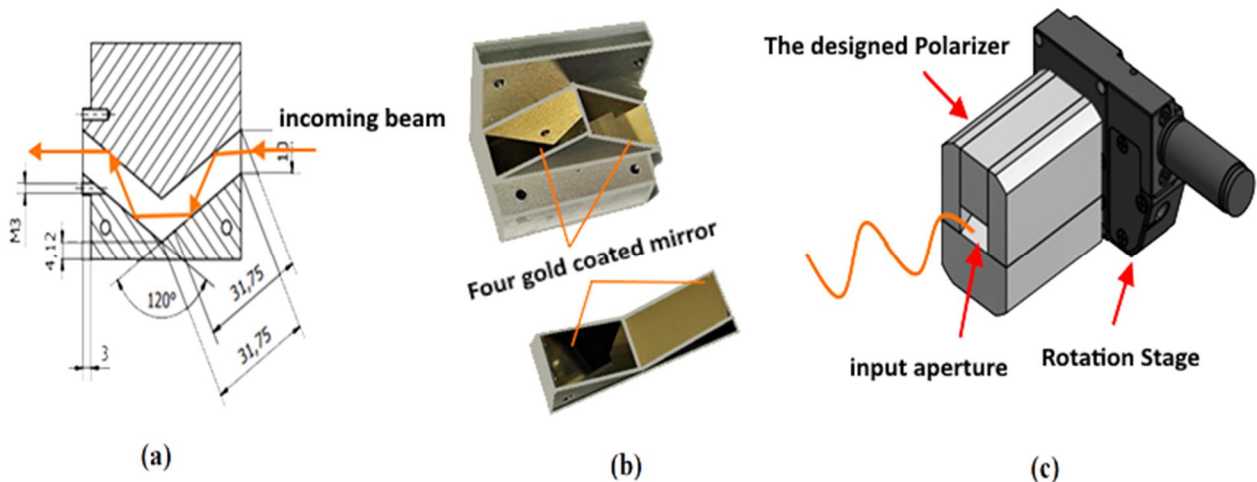


Figure 3.13. (a) Design of four reflecting-mirrors polarizer consisting of two halves, (b) all mirrors consisting of 200 nm layer of Au on Si substrate glued onto the machined surfaces. (c) The overall shape of four reflection polarizer attached to the rotation stage.

In order to mount the polarizer in the experimental chamber together with the rotation stage and CEM detector, a special holder has been designed. The whole assembly is mounted on movable holders rotated in a θ - 2θ configuration to allow measurements at different angles of incidence. A schematic diagram of the polarizer together with the CEM detector is shown in Fig. 3.14.

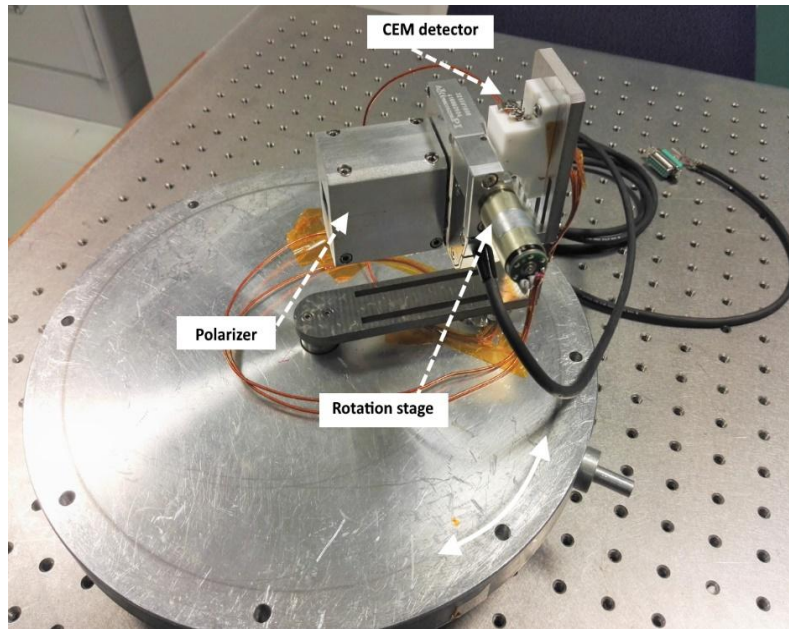
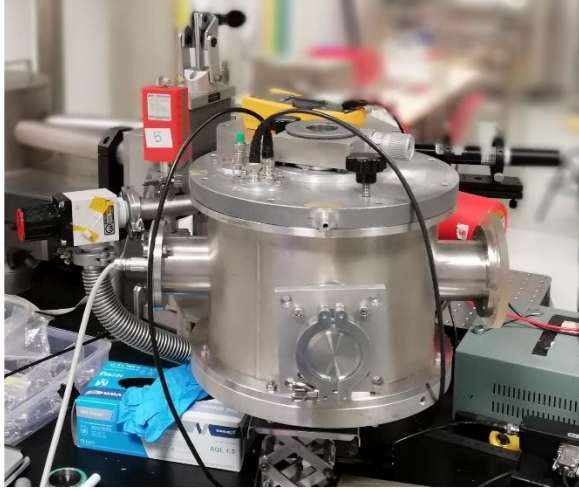
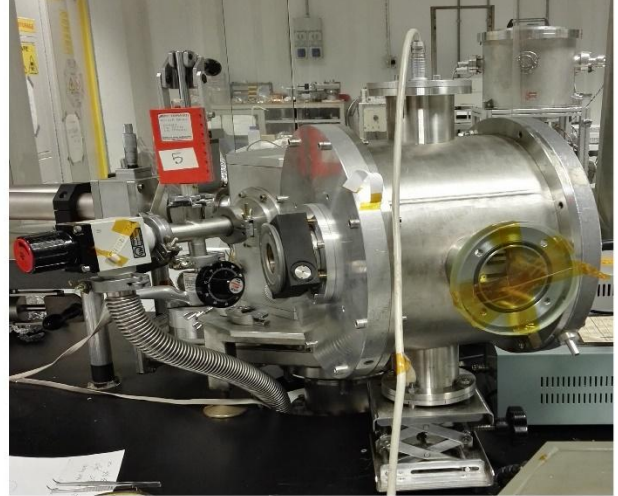


Figure 3.14. The polarizer attached with the rotation stage together with the CEM detector.

Before starting the polarimetric characterization of our reflectometer facility, we measured the specular reflectance of the gold coated mirror in order to test the performance and optical quality of the resulted mirror. The reflectance has been performed in two configurations of the experimental chamber, called *up* and *down* to get the reflectance R_s and R_p for the s-and p-polarization components. The two configurations of the reflectometer experimental chamber are shown in Fig.3.15, where the down-configuration is obtained by a rotation of 90° with respect to the up-configuration.



(a)



(b)

Figure 3.15. The two configurations of the reflectometer experimental chamber. (a) The up-configuration while in (b) the down-configuration is obtained by a rotation of 90° with respect to the up-configuration.

The experimental reflectance associated with the two possible configurations can be obtained from the following relations:

$$R_s = \frac{R_{up} + R_{down}}{2} + \frac{R_{up} - R_{down}}{2P} \quad 3.2$$

$$R_p = \frac{R_{up} + R_{down}}{2} - \frac{R_{up} - R_{down}}{2P} \quad 3.3$$

where P is the polarization degree; since the polarization degree of the reflectometer has not been characterized yet, so it is preferable to take the average value of reflectance R_{avg} corresponding to the value of R_{up} and R_{down} . This has been taken as:

$$R_{avg} = \frac{R_{up} + R_{down}}{2} \quad 3.4$$

The reflectance of gold specimen was measured at wavelengths of 121.6 nm and 160 nm as a function of the incidence angle which varied with a step of 10°. For each incidence angle, 10 measurements were recorded to take into account the possible experimental uncertainty. Afterwards the average and standard deviation were calculated for each dataset. Fig. 3.16. and

Fig.3.17 show respectively the average reflectance of the gold coated mirror compared with the simulated one versus angle of incidence at wavelengths of 121.6 nm and 160 nm; assuming the optical constant of Palik [57] and an error of about (5%) in the experimental measurements.

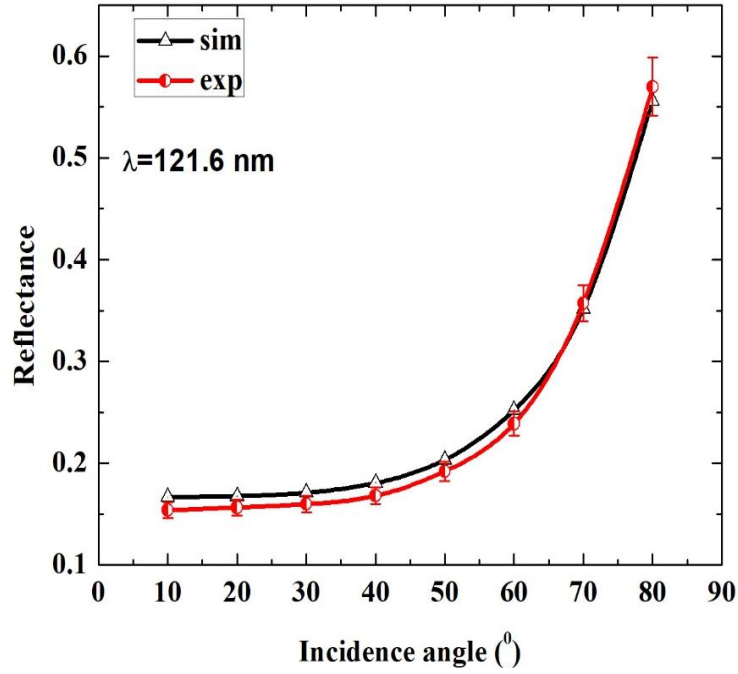


Figure 3.16. Average experimental and simulated reflectance versus the incidence angle at 121.6 nm.

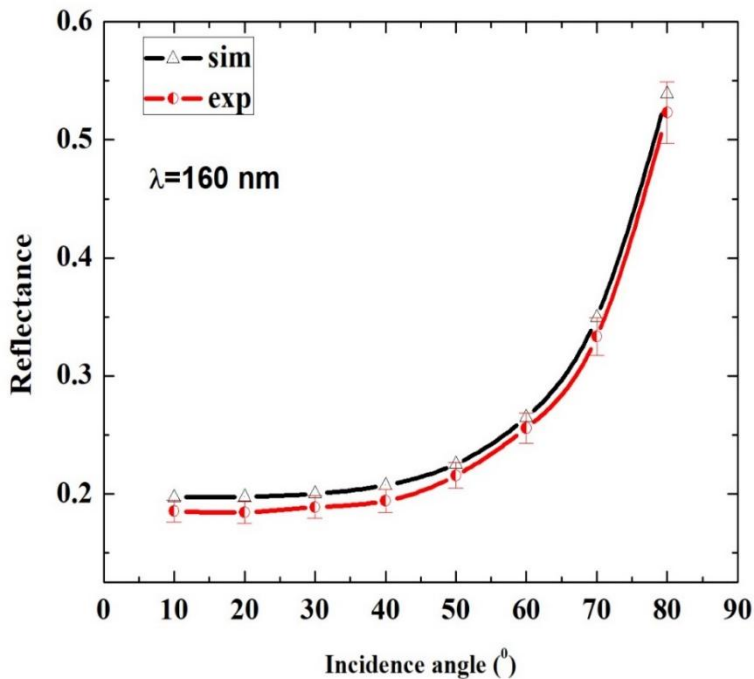


Figure 3.17. Average experimental and simulated reflectance versus the incidence angle at 160 nm.

Chapter.4

System Calibration and Phase Retarder Reflector

The beam emitted from the FUV-EUV reflectometer facility has a considerable polarization due to the geometrical arrangement of the diffraction grating and the toroidal mirror. However, few contributions due to the effects of un-polarized, or circularly polarized light have to be considered. A small contribution of un-polarized light may lead to a significant error in the determination of the optical constants and studying the structural properties of the materials. Thus for accurate ellipsometric measurements in the FUV-EUV regions, a complete polarimetric characterization of the incoming beam is necessary.

4.1. Polarimetric Characterization of The Light Source

As described in chapter two, the light source can be described in terms of the four Stokes parameters that determine the total intensity, (S_0), the two components of linear intensity, (S_1) and (S_2), while (S_3) describes the amount of right or left circular polarization [60]. The polarization effect of an instrument is described by the related Mueller matrix (M) of the optical system and the Stokes vector of the output light which is given by:

$$S_{out} = MS_{in} \quad 4.1$$

An instrument often consists of several optical elements in series, and the equivalent Müller matrix of the whole system is given by the product of the Müller matrices for each element. In case of the four-reflection linear polarizer with common incidence plane which is used in our experiment, the equivalent Müller matrix is given by the relationship:

$$M_{FRP} = (M)^4 \quad 4.2$$

Thus, the Mueller matrix of the four-reflection linear polarizer is:

$$M_{FRP} = \begin{pmatrix} \frac{|r_s|^8 + |r_p|^8}{2} & \frac{|r_s|^8 - |r_p|^8}{2} & 0 & 0 \\ \frac{|r_s|^8 - |r_p|^8}{2} & \frac{|r_s|^8 + |r_p|^8}{2} & 0 & 0 \\ 0 & 0 & r_s^4 r_p^4 & 0 \\ 0 & 0 & 0 & r_s^4 r_p^4 \end{pmatrix} \quad 4.3$$

The terms r_s^8 and r_p^8 arise because the polarizer is based on four-reflection mirrors. The polarizer can be rotated by an angle (θ_r) around its axis with respect to the beam propagation direction, in order to change the orientation of the transmitted beam through the polarizer. The Mueller matrix for a rotator is needed and, the mathematical representation of rotated polarizer is expressed by the following relationship

$$R(-\theta_r)M_{FRP}R(\theta_r) \quad 4.4$$

where $R(\pm\theta_r)$ represents the Mueller matrix of a rotator and (θ_r) is the rotation angle of the polarizer around the beam propagation axis. According to the Mueller calculus, the Mueller matrix of the four-reflection rotated polarizer is:

$$M_{FRP} = \begin{pmatrix} \frac{|r_s|^8 + |r_p|^8}{2} & \frac{|r_s|^8 - |r_p|^8}{2} \cos 2\theta_r & \frac{|r_s|^8 - |r_p|^8}{2} \sin 2\theta_r & 0 \\ \frac{|r_s|^8 - |r_p|^8}{2} \cos 2\theta_r & \frac{|r_s|^8 + |r_p|^8}{2} \cos^2 2\theta_r + r_s^4 r_p^4 \sin^2 2\theta_r & \frac{|r_s|^8 + |r_p|^8}{2} \cos 2\theta_r \sin 2\theta_r - r_s^4 r_p^4 \sin^2 2\theta_r \cos 2\theta_r & 0 \\ \frac{|r_s|^8 - |r_p|^8}{2} \sin 2\theta_r & \frac{|r_s|^8 + |r_p|^8}{2} \sin 2\theta_r \cos 2\theta_r - r_s^4 r_p^4 \cos 2\theta_r \sin 2\theta_r & \frac{|r_s|^8 + |r_p|^8}{2} \sin^2 2\theta_r + r_s^4 r_p^4 \cos^2 2\theta_r & 0 \\ 0 & 0 & 0 & r_s^4 r_p^4 \end{pmatrix} \quad 4.5$$

The mathematical representation of the Stokes parameters of the transmitted beam through the polarizer is:

$$S_{out} = R(-\theta_r)M_{FRP}R(\theta_r)S_{in} \quad 4.6$$

The output intensity of the light beam propagating through the polarizer and collected by the detector is:

$$S_0 = \frac{1}{2} \left((|r_s|^8 + |r_p|^8) S_0 + (|r_s|^8 - |r_p|^8) S_1 \cos 2\theta_r + (|r_s|^8 - |r_p|^8) S_2 \sin 2\theta_r \right) \quad 4.7$$

The Stokes parameters S_0 , S_1 , and S_2 can be retrieved by investigating the output signals coming from the rotating polarizer where S_0 is the total intensity that we can assume to be normalized.

A schematic diagram of the experimental set up for characterizing the incoming beam is shown in Fig.4.1; the toroidal mirror reflects the monochromatic radiation to the experimental chamber where are placed the polarizer and the detector. The beam is allowed to pass through the four-reflection polarizer (FRP) rotated counterclockwise with respect to the beam propagation direction around the beam axis by an angle (θ_r) and the modulated intensity is gathered by the channel electron multiplier (CEM KBL 10RSR) working in photon counting mode.

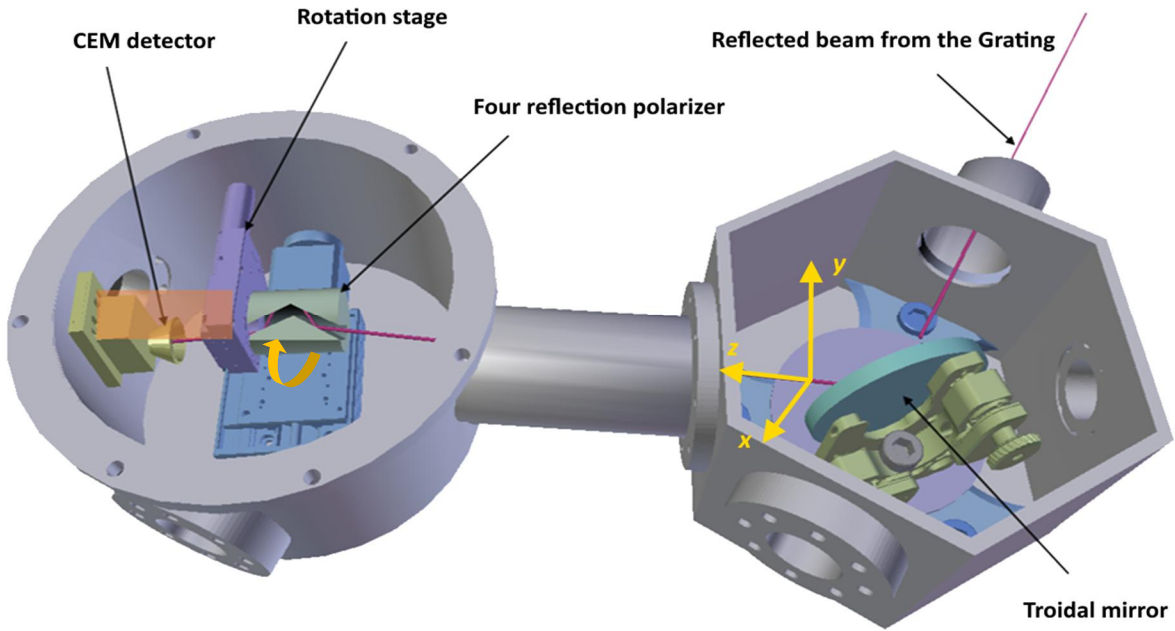


Figure 4.1. The experimental arrangements for measuring the polarization of beam delivered by reflectometer facility.

The Stokes parameter S_1 and S_2 have been explored at two wavelengths of particular interest for space applications. In order to retrieve the Stokes parameter S_2 ; we performed the

measurements by rotating the experimental chamber through angle of 45° clockwise around the direction defined by the beam propagation; for that purpose, a homemade flange was designed with different screws holes oriented at different rotation angles (30° , 45° , and 60°), (see Appendix C). Then, the light entering was (-45°) partially linearly polarized. We used a MATLAB code developed accordingly to Eq. (4.7), in order to determine S_1 and S_2 by a fitting procedure, (see Appendix B). To reduce the numerical uncertainties due to the number of free parameters, the reflectance values of the gold mirrors were experimentally measured. Fig. 4.2a and 4.2b show the measured and fitted data as a function of the rotation angle of the polarizer in two polarization states at a wavelength of 121.6 nm.

- a) almost fully polarized light along the y-axis as described by the polarization ellipse shown in Fig.4.3a.
- b) almost fully -45° polarized light as described by the polarization ellipse shown in Fig.4.3b.

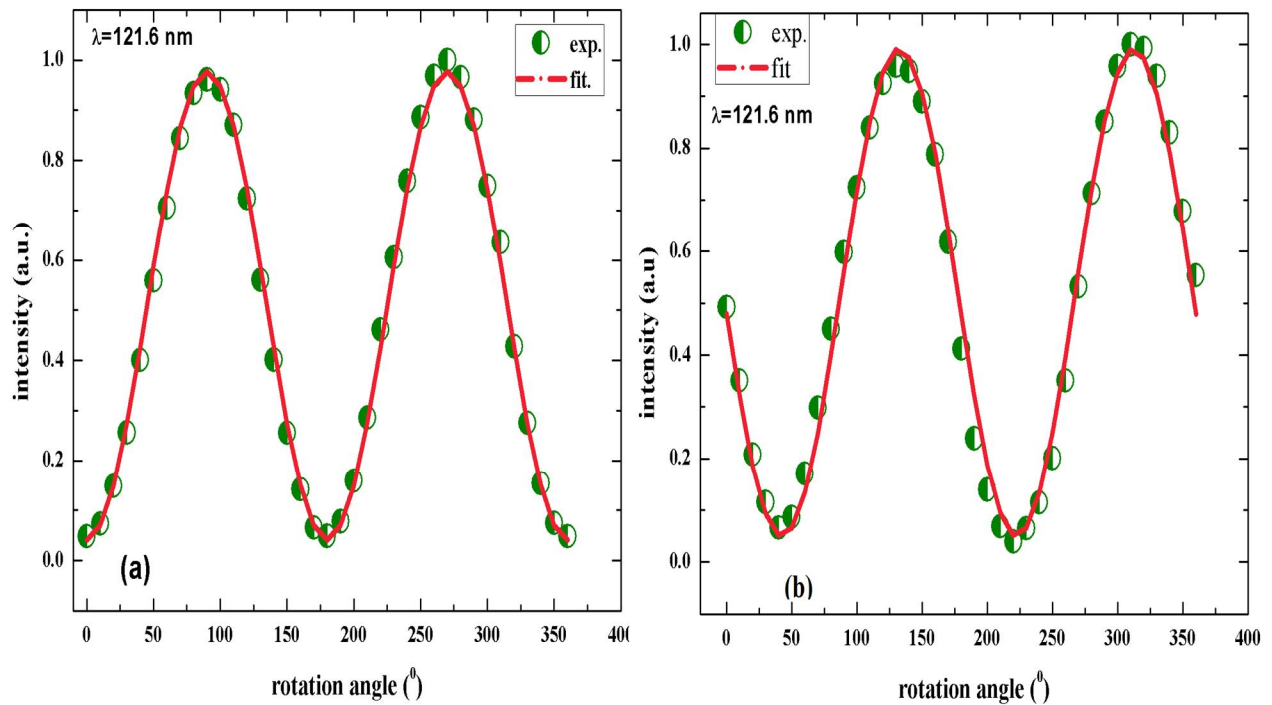


Figure 4.2. (a) Measured values and the fitted curve of the modulated intensity against the rotation angle of the polarizer at 121.6 nm in case of almost fully polarized light along the y-axis; (b) measured values and the fitted curve of the modulated intensity against the rotation angle of the polarizer at 121.6 nm in case of almost fully -45° polarized light.

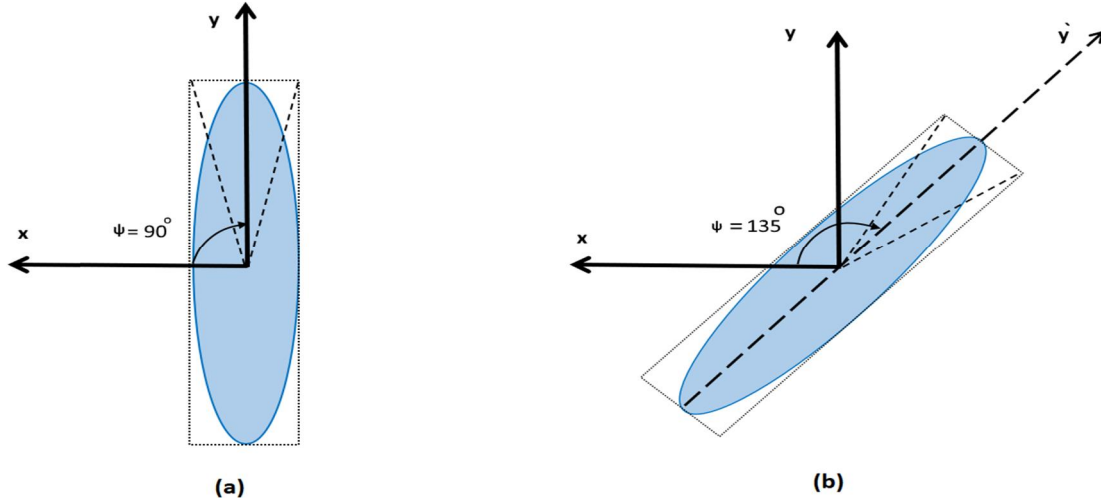


Figure 4.3. (a) The polarization ellipse represents the initial position of the experimental chamber, almost fully polarized light along the y-axis. (b) almost fully linearly polarized light oriented at 135° .

For later data analysis, we also investigated the polarization degree at a wavelength of 160 nm by using the same facility and the same spectral lamp. Fig. 4.4a and 4.4b show the measured and fitted data against the rotation angle of the polarizer in the two polarization states at a wavelength of 160 nm.

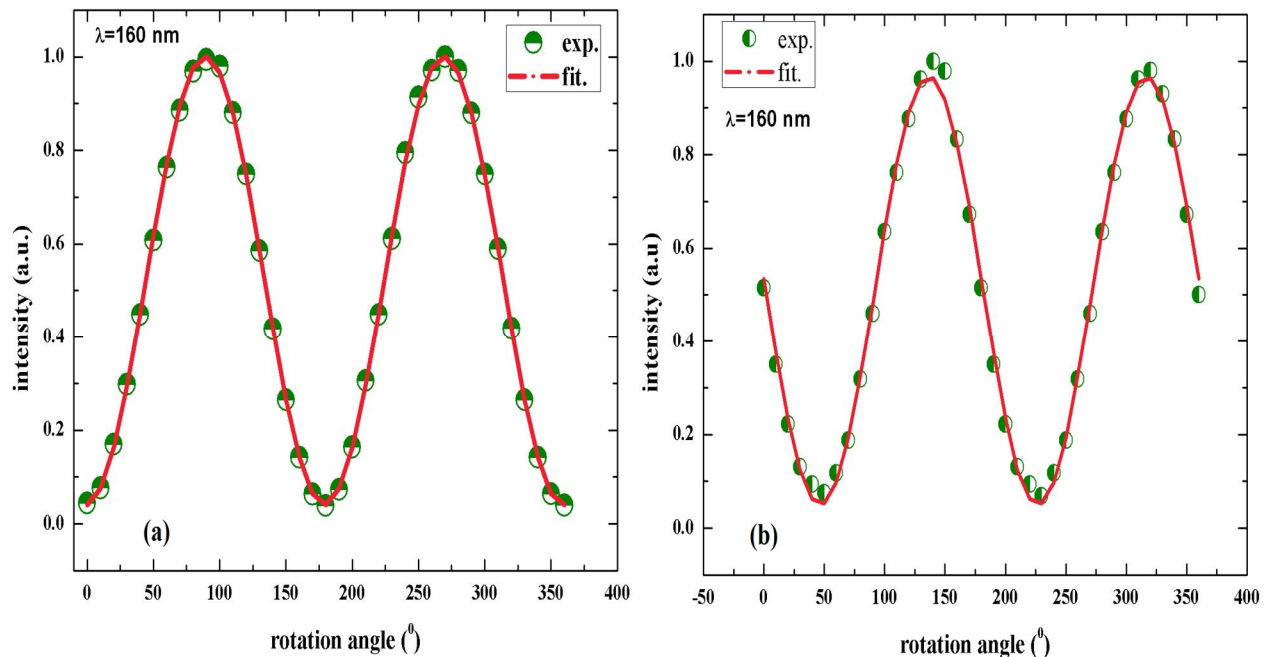


Figure 4.4. (a) The measured and the fitted curves of the modulated intensity against the rotation angle of the polarizer at 160 nm in case of almost fully polarized light along the y-axis; (b) in case of almost fully -45° polarized light.

The experimental chamber position for the two polarization states are shown in Fig.4.5 a) where the incident beam is seen to be vertically linearly polarized. b) The chamber rotated at angle 45° clockwise with respect to the propagation direction of the incoming beam.

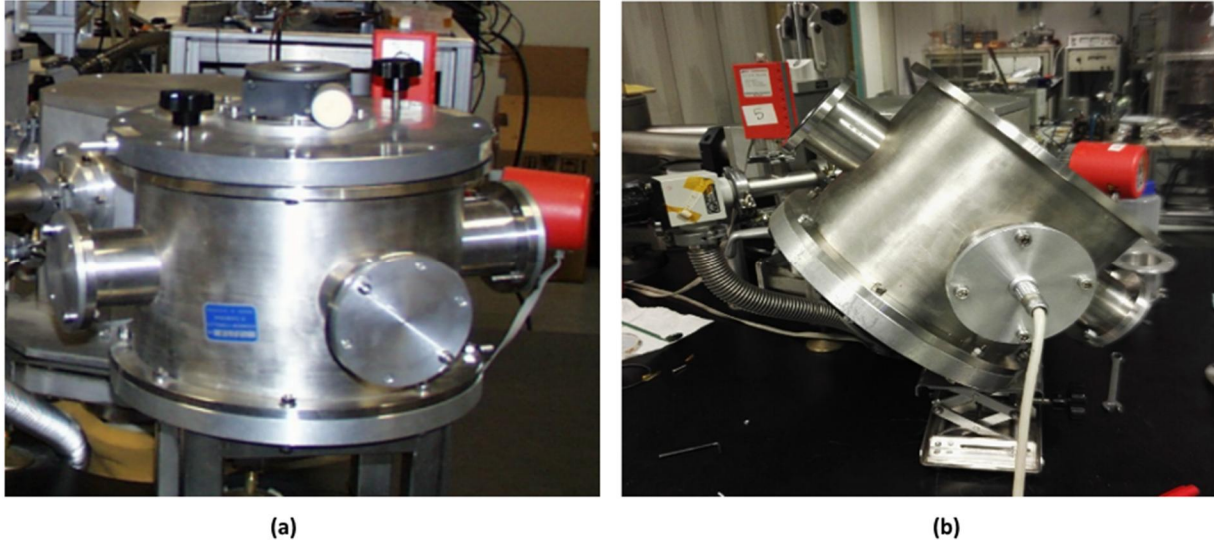


Figure 4.5. (a) The initial position of the experimental chamber where the incident beam is almost vertical linearly polarized. (b) The chamber rotated at an angle (45°) clockwise with respect to the propagation of the incoming beam.

The fitting procedures are based on the Levenberg–Marquardt algorithm. For each free parameter, we defined the limits which can have a lower and upper bound lb , and ub , respectively. We performed the fitting procedure several times by randomly changing the starting guess of the parameters between the selected intervals. The output parameters were determined from the fitting procedures are summarized in Table 4.1.

Table 4.1. The Stokes parameters of the incident beam at wavelengths of 121.6 nm and 160 nm

Experimental chamber position	Wavelength 121.6 nm		Wavelength 160 nm	
	S_1	S_2	S_1	S_2
0	-0.92	.002	-0.90	-0.003
45	.002	-0.908	-.052	-0.903

4.2. Characterization of Al Phase Retarder Reflector

In the previous section, we pointed out that the polarizer has allowed a preliminary characterization of the facility and the definition of the first three Stokes parameters. However, a complete characterization of the system requires the use of a quarter-wave plate for the estimation of the fourth Stokes parameter [61].

Aluminum coatings are known to have phase retarder properties, although these are subject to oxidation and aging processes. Thus, to estimate the potential of our tabletop ellipsometry system; we used a single layer of aluminum as a phase retarder reflector. The nominal structure of the sample is shown in Fig.4.6. It consists of ~ 100 nm thick films deposited by e-beam evaporation on a Si substrate with a 3 nm layer of chromium interposed as an adhesion layer.

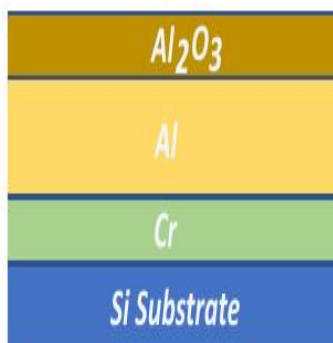


Figure 4.6. The nominal structure of the sample as monitored with the quartz microbalance during the deposition.

The deposition chamber was pumped using a high vacuum Varian turbomolecular pump in series with a scroll pump. We used as evaporation material, 3-6 mm sized pieces of *Al* with a purity of 99.9%. The base pressure in the chamber was 10^{-6} mbar. The distance between the evaporation source and the substrate was 40 cm, and the substrate holder was rotating during the deposition process. For this work, we used *Si* (100) polished wafers cut into sizes of about 1 cm^2 . The deposition parameters set for our sample and the thicknesses of the existing layers are shown in Table 4.2. The Film thickness was controlled during the deposition with a quartz-crystal monitor calibrated using a *KLA – Tencor P – 16 +* Profilometer, which measures the difference in thickness between the substrate and the deposited thin film.

Table 4.2. The deposition parameters for the aluminum sample.

Evaporated Material	Pressure work (mbar)	Deposition rate (Å/sec)	Measured thickness (nm)
Al	2.0×10^{-6}	10	100
Cr	3.7×10^{-6}	0.4	3.2
Si Substrate			

The aluminum phase retarder sample was introduced along the optical path, then the beam reflected by the phase retarder element was analyzed by the polarizer and recorded by the CEM detector, in order to estimate S_3 and determine the ellipsometric parameters δ and ψ . Accordingly, the output signal is described as follows in terms of the Stokes parameters and Mueller matrix:

$$S_{out} = R(-\theta_r)M(FRP)R(\theta_r)M(QWR)S_{in} \quad 4.8$$

Where $M(QWR)$ is the Mueller matrix of the phase retarder element and $R(\pm\theta)$ are the rotation matrices. From the general point of view, the Mueller matrix of a reflector can be derived by describing its behavior as a polarizer with the amplitude reflection coefficients r_s^R and r_p^R , in series to a phase retarder with δ as the phase delay:

$$M_{Retardar} = \begin{pmatrix} \frac{|r_s^R|^2 + |r_p^R|^2}{2} & \frac{|r_s^R|^2 - |r_p^R|^2}{2} & 0 & 0 \\ \frac{|r_s^R|^2 - |r_p^R|^2}{2} & \frac{|r_s^R|^2 + |r_p^R|^2}{2} & 0 & 0 \\ 0 & 0 & |r_s^R||r_p^R|\cos\delta & |r_s^R||r_p^R|\sin\delta \\ 0 & 0 & -|r_s^R||r_p^R|\sin\delta & |r_s^R||r_p^R|\cos\delta \end{pmatrix} \quad 4.9$$

The properties of phase retarders and quarter wave plates can be described by the ellipsometric parameters, ψ and δ derived by ellipsometric measurements and defined by the following relationship [62]:

$$\tan\psi = \frac{r_p}{r_s} \quad \Delta = \delta_p - \delta_s \quad 4.10$$

Referring to the experiment, if the light emitted by the deuterium lamp was reflected by the sample under investigation, then the detected intensity in our case is described as following, according to the Stokes formalism and Mueller calculus.

$$S_0 = \frac{1}{4} \begin{bmatrix} \left[\left(|r_s|^8 + |r_p|^8 \right) \left(|r_s^R|^2 + |r_p^R|^2 \right) + \left(|r_s|^8 - |r_p|^8 \right) \left(|r_s^R|^2 - |r_p^R|^2 \right) \cos 2\theta_r \right] S_0 \\ + \left[\left(|r_s|^8 + |r_p|^8 \right) \left(|r_s^R|^2 - |r_p^R|^2 \right) + \left(|r_s|^8 - |r_p|^8 \right) \left(|r_s^R|^2 + |r_p^R|^2 \right) \right] \cos 2\theta_r S_1 \\ + 2 \left[\left(|r_s|^8 - |r_p|^8 \right) r_s^R r_p^R \cos \delta \sin 2\theta_r \right] S_2 + 2 \left[\left(|r_s|^8 - |r_p|^8 \right) r_s^R r_p^R \sin \delta \sin 2\theta_r \right] S_3 \end{bmatrix} \quad 4.11$$

where:

- S_0 is the first term of the Stokes vector of the output light.
- $S_0, S_1, S_2,$ and S_3 are the Stokes parameters describing the incoming light.
- r_s and r_p the polarized reflection coefficients of the gold coating.
- r_s^R and r_p^R the polarized reflection coefficients of the sample under investigation.
- θ is the rotation angle of the polarizer.
- δ is the relative phase between s-and p-reflected components.

Eq. (4.11) can be conveniently rewritten in terms of the ratio $\frac{r_p}{r_s}$, to handle only three unknown parameters: the ratio, the phase δ and, the Stokes parameters S_3 . The experimental equipment for testing the aluminum sample is shown in Fig. 4.7, the incident beam was configured to have almost fully -45° linear polarization impinging the sample [63,64]. The electric field vector E propagates along the z axis and can be represented regarding s-and p- polarization as described in Fig.4.8.

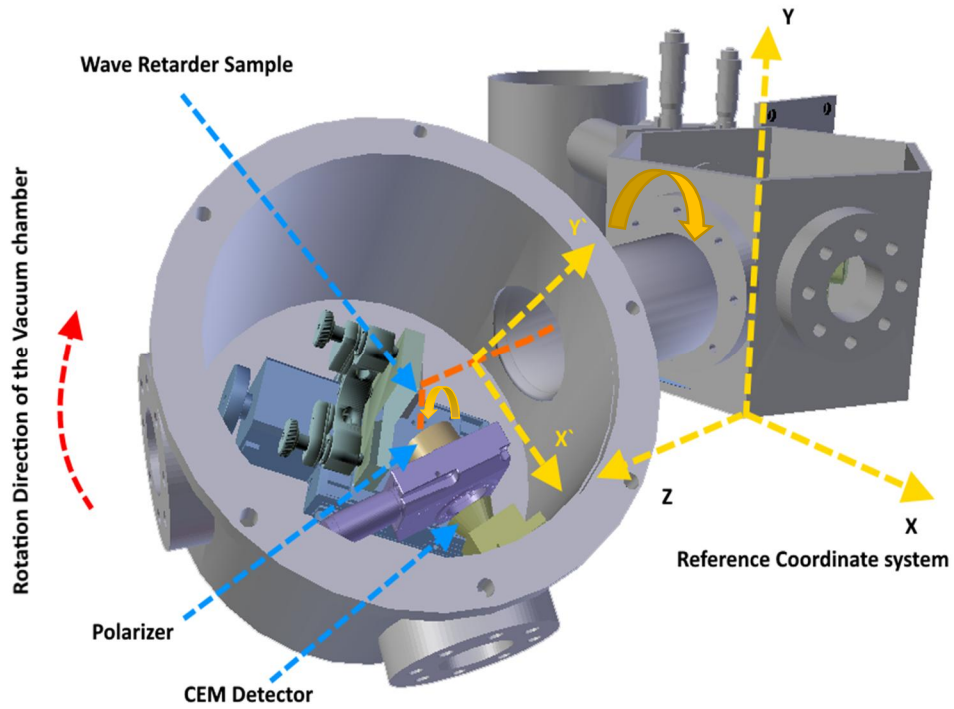


Figure 4.7. The experimental arrangement for testing a phase retarder by using the improved VUV-EUV normal incidence reflectometer facility.

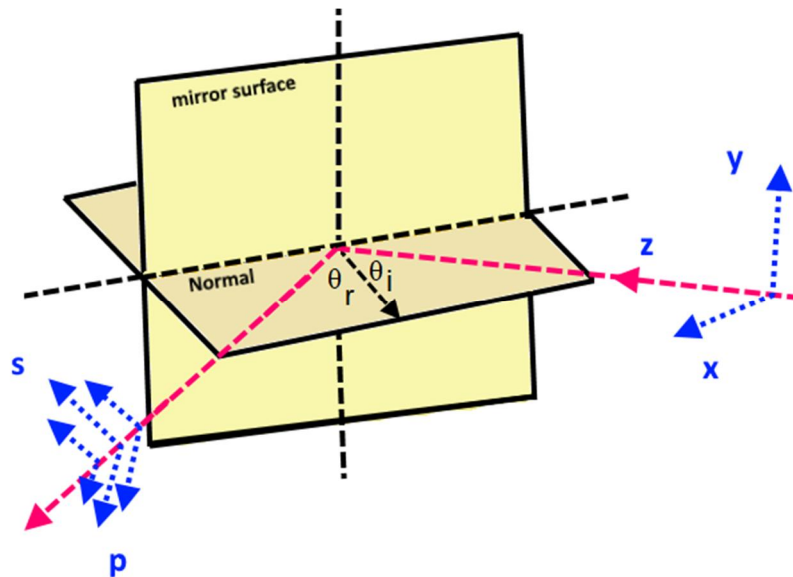


Figure 4.8. The reference system used in the experiment. Incident linearly polarized light with an electric field vector E_i propagates along the z axis. The two orthogonal s, and p component of the reflected beam are seen respectively along the y-and x- axis.

The aluminum sample has been measured at four different incidence angles. At each incidence angle on the sample, the analyzer was rotated from 0° to 360° with 10° steps. For each incidence angle; 5 measurements were recorded, then the average and standard deviation were calculated for each dataset. The output intensity at each angle was recorded versus the rotation angle of the polarizer acting as an analyzer. The fitted and measured curves are shown in Fig.4.9 and Fig.4.10.

In order to determine the parameters ψ and δ of the sample for each incidence angle and to estimate S_3 , we performed the fitting procedure by using a MATLAB code based on the Levenberg–Marquardt algorithm and developed according to the Eq. (4.11). We defined the limits for each free parameter and performed the fitting procedure 300 times by randomly changing the starting guess of the parameters between the selected intervals. The standard deviations (STDV) were calculated over 300 iterations. For more details about the MATLAB code see Appendix (B). The output values of the ellipsometric parameters are reported in Table 4.3.

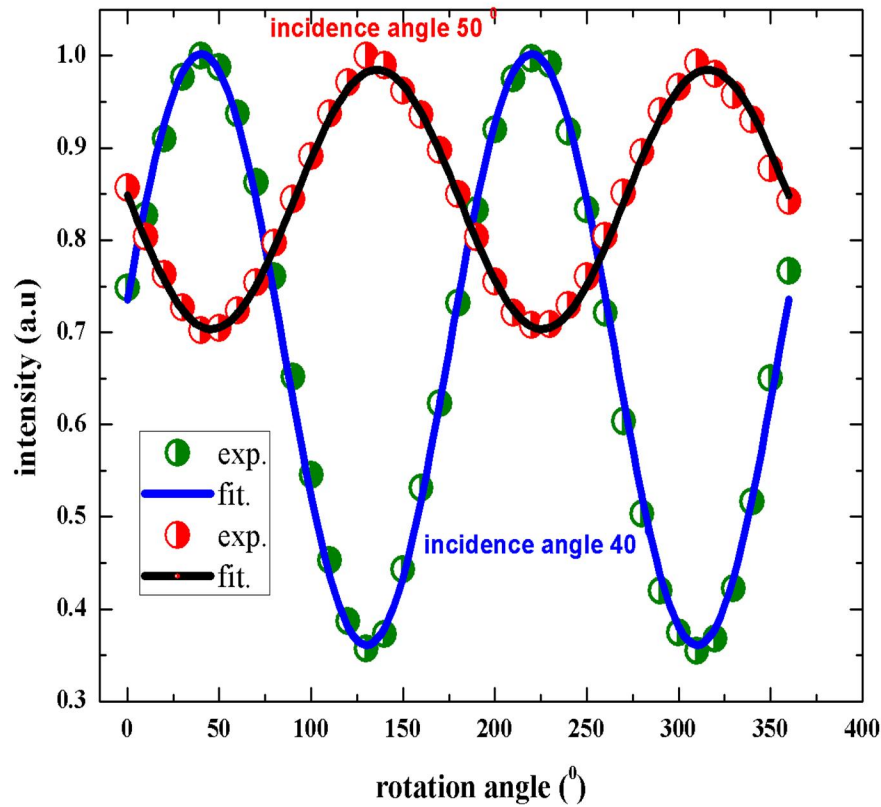


Figure 4.9. Measured and fitted data of aluminum samples at two different incidence angle 40° and 50° .

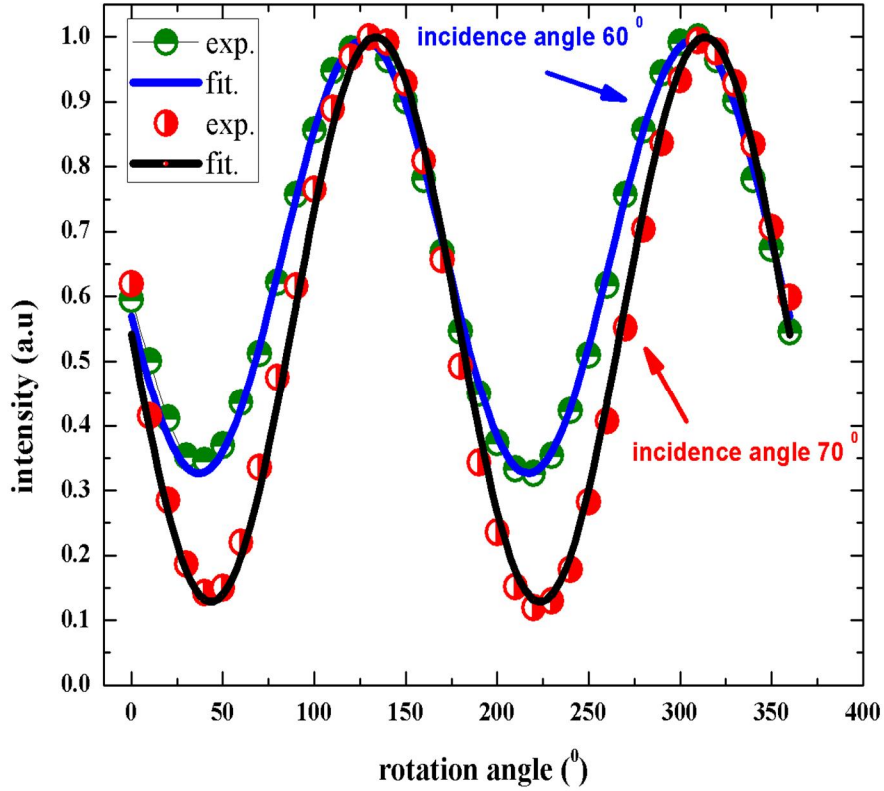


Figure 4.10. Measured and fitted curves of aluminum samples at two different incidence angle 60° and 70°

Table 4.3. The fitted values of ratio, phase and S_3 with the standard deviation STDV.

Incidence angle	$\tan\psi = \frac{r_p}{r_s}$	STDV ratio	$\Delta\delta^0$	STDV $\Delta\delta^0$	S_3	STDV S_3
40	1.12	8×10^{-7}	68	6	0.020	0.12
50	1.08	2×10^{-4}	101	6	0.005	0.097
60	0.94	1.5×10^{-5}	120	6	-0.033	0.098
70	1.04	2×10^{-7}	142	5	-0.063	0.082

The approach allows to estimate the value of S_3 even the associated uncertainties is quite bigger, the fourth Stokes parameter resulted to be rather small. This value is reasonable if we consider that the beam coming from the reflectometer is emitted by an incoherent source and becomes almost fully linearly polarized. Fig.4.11 shows the variation of the phase difference plotted against the Stokes parameters S_3 . Usually the value of S_3 fluctuates between the constraints

of the lower and upper limits $-1 \leq S_3 \leq 1$; the best fits are obtained when the values of S_3 encountered lie between $-0.05 \leq S_3 \leq 0.05$ as described by the blue rectangular area inside Figure 4.11. The figure shows also that a small variation in S_3 can induce considerable phase deviation with about 5° .

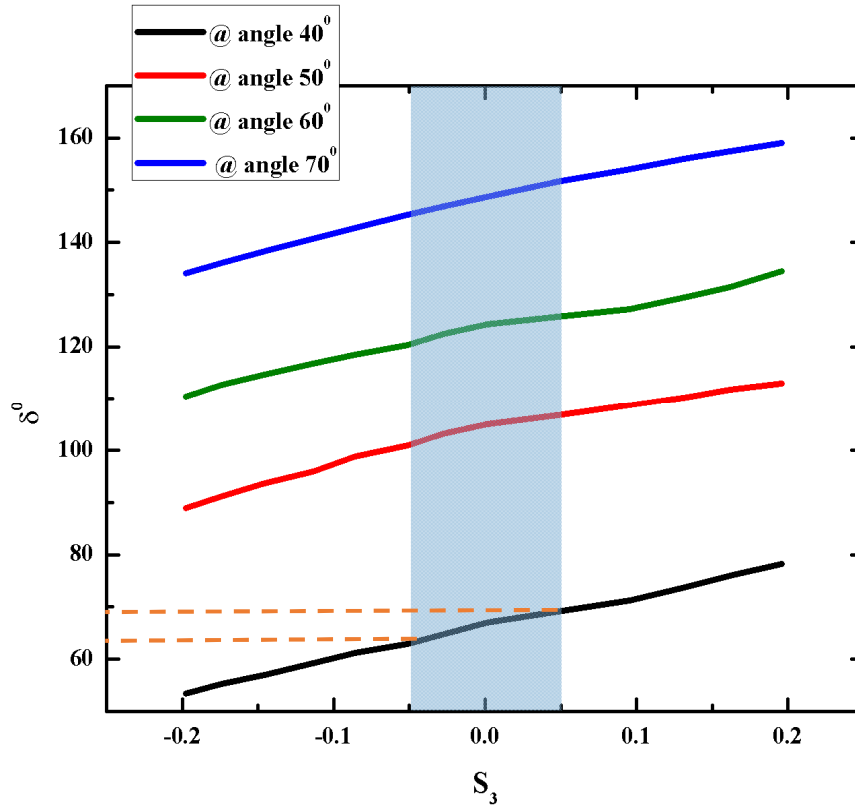


Figure 4.11. The variation of phase plotted versus the Stokes parameters S_3 at different working incidence angles on the Al mirror.

The ellipsometric parameters of the sample can be determined quite accurately. The uncertainty associated with the phase is around (3%) depending on the incidence angles, while the uncertainty for the ratio is negligible. We use the phase derived from the ellipsometric measurements in order to retrieve the properties of the sample under investigation and to evaluate the potential of the method and the experimental system capabilities.

Aluminum is well known to have a thin oxide layer on its surface due to the reaction with air which strongly affects the optical properties of the film [65]. We fitted the experimental phase by using IMD software [66] in order to retrieve the thickness of the oxide layer. Usually, IMD uses

the Levenberg-Marquardt algorithm to calculate the confidence intervals against the goodness of the fit parameter chi-square χ^2 . For the structure considered here, the nonlinear curve fitting in IMD is repeated until the probability of finding the fit parameter values with high level of confidence. Fig. 4.12 shows the measured phase versus the incidence angle at a wavelength of 121.6 nm and the fitted curve by IMD. The thicknesses of the oxide layer determined by the fitting procedure are given in the legend of Fig. 4.12. The thicknesses mainly depend on the optical constants; thus, they can affect the exact determination of the layer thickness. We used the optical constants reported by Palik [57] and Hegemann [67].

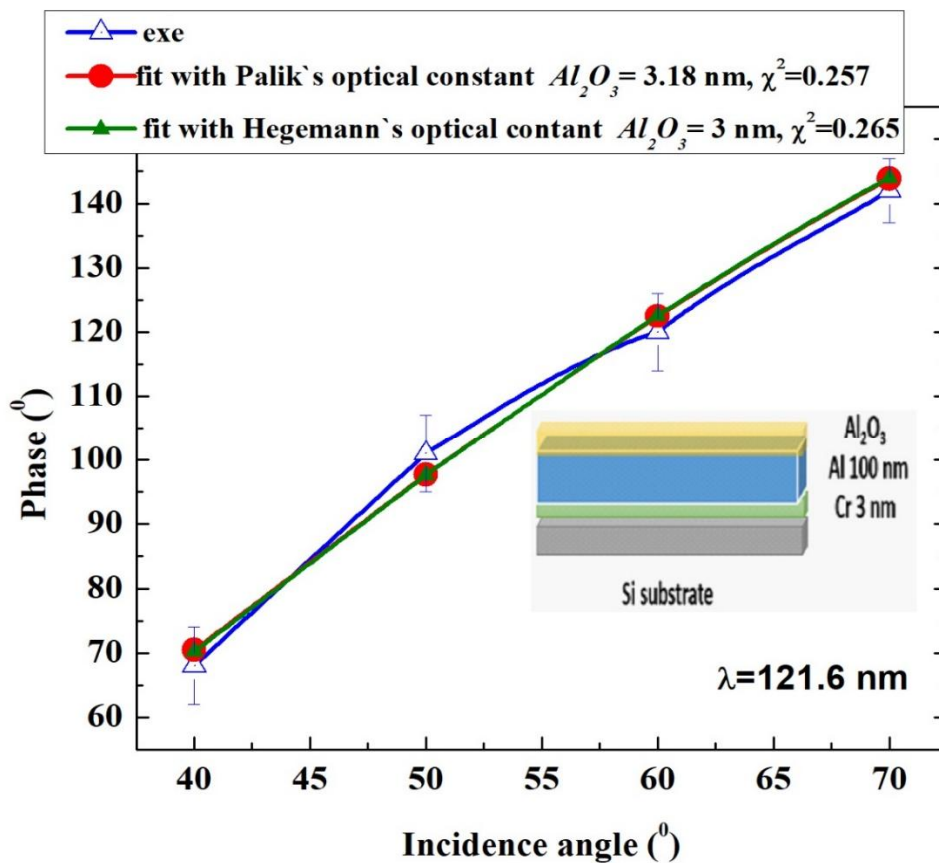


Figure 4.12. The phase shift of the aluminum sample plotted against the incidence angle at a wavelength of 121.6 nm; the measured data were fitted by IMD software in order to determine the thickness of the oxide layer on top of the aluminum surface.

Additionally, we performed specular reflectance measurements for the sample at the same wavelength to verify the result obtained by analyzing the phase. Fig. 4.13 shows the experimental and the simulated reflectance of the determined structures.

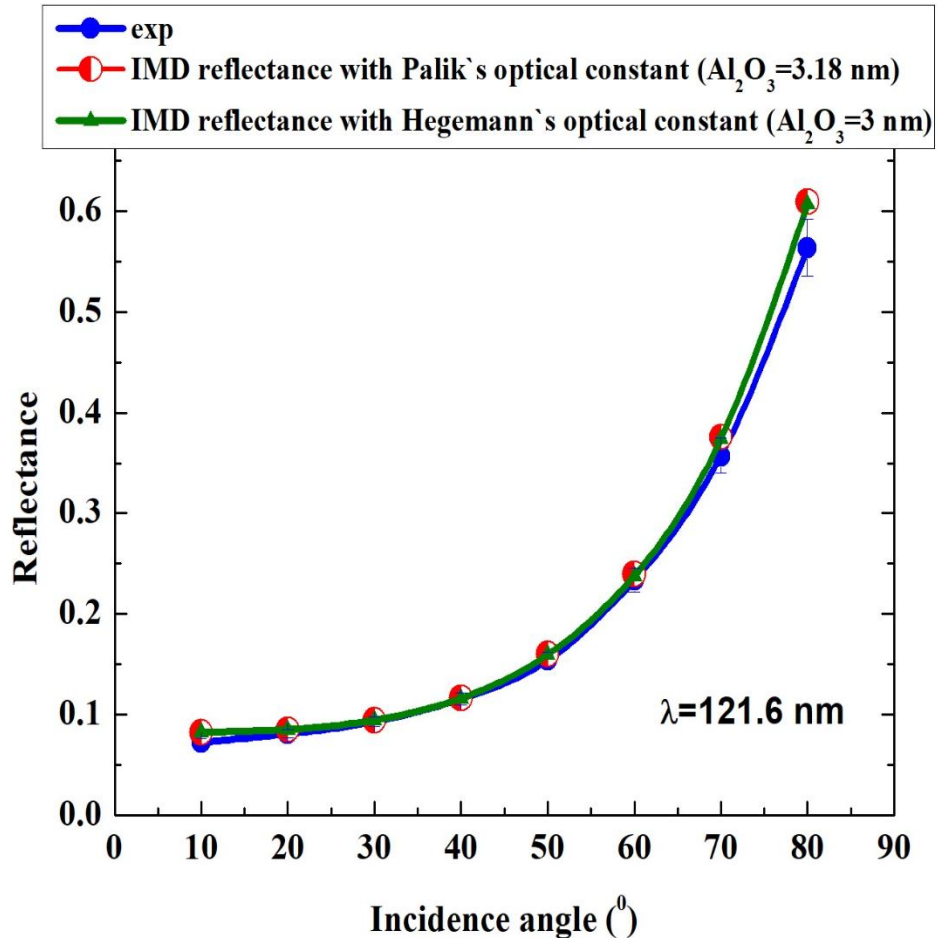


Figure.4.13. Reflectance measurements and simulation by IMD of aluminum sample for both optical constants for the structure shown in the legend of Fig. 4.12 with sharp interfaces.

In order to verify the reliability and accuracy of the method, Table 4.4 shows the fitted parameters derived from the ellipsometric measurements compared with the results of the reflectance simulation performed by IMD with the optical constants reported by Palik and Hegemann [57,67]. The data are in good agreement for both sets of the optical constants however in case of the ratio, the best fit that can match our model is that of Palik's optical constant. The deviations between the values obtained from the ellipsometric measurements and the IMD ones can be reasonably attributed to small variations in optical constants, due to the sample fabrication process and storage, and experimental alignment errors.

Table 4.4. The fitted parameters obtained by MATLAB Code compared with those retrieved by IMD software.

Incidence angle	Simulation by IMD ($Al_2O_3=3.18$ nm) Palik's optical constant		Simulation by IMD ($Al_2O_3=3$ nm) Hegemann's optical constant		Fitted data by using ellipsometric measurements (MATLAB code)	
	$\tan\psi = \frac{r_p}{r_s}$	$\Delta\delta^0$	$\tan\psi = \frac{r_p}{r_s}$	$\Delta\delta^0$	$\tan\psi = \frac{r_p}{r_s}$	$\Delta\delta^0$
40	1.20	71	1.23	70	1.12	68±6
50	1.24	98	1.27	98	1.08	101±6
60	1.21	122	1.23	122	0.94	120±6
70	1.14	144	1.16	144	1.04	142±5

In terms of the structure of the sample, the sensitivity in determining the thickness of the aluminum oxide is estimated to be 0.3 nm. Such sensitivity comes out from analyzing the trend of the ratio that requires a thinner oxide thickness (2.90 nm instead of 3.18 nm) to be matched. The simulated ratio and phase corresponding to 2.90 nm of Al_2O_3 on top of the Al film and retrieved by IMD with different optical constants are reported in Table 4.5. The corresponding reflectance is graphed in Fig. 4.14.

Table 4.5. The fitted parameters obtained by MATLAB Code compared with those retrieved by IMD software for Al_2O_3 thickness of 2.90 nm.

Incidence angle	Simulation by IMD ($Al_2O_3=2.9$ nm) Palik's optical constant		Simulation by IMD ($Al_2O_3=2.9$ nm) Hegemann's optical constant		Fitted data by using ellipsometric measurements (MATLAB code)	
	$\tan\psi = \frac{r_p}{r_s}$	$\Delta\delta^0$	$\tan\psi = \frac{r_p}{r_s}$	$\Delta\delta^0$	$\tan\psi = \frac{r_p}{r_s}$	$\Delta\delta^0$
40	1.10	66	1.18	68	1.12	68±6
50	1.13	92	1.21	95	1.08	101±6
60	1.13	117	1.20	120	0.94	120±6
70	1.09	140	1.14	142	1.04	142±6

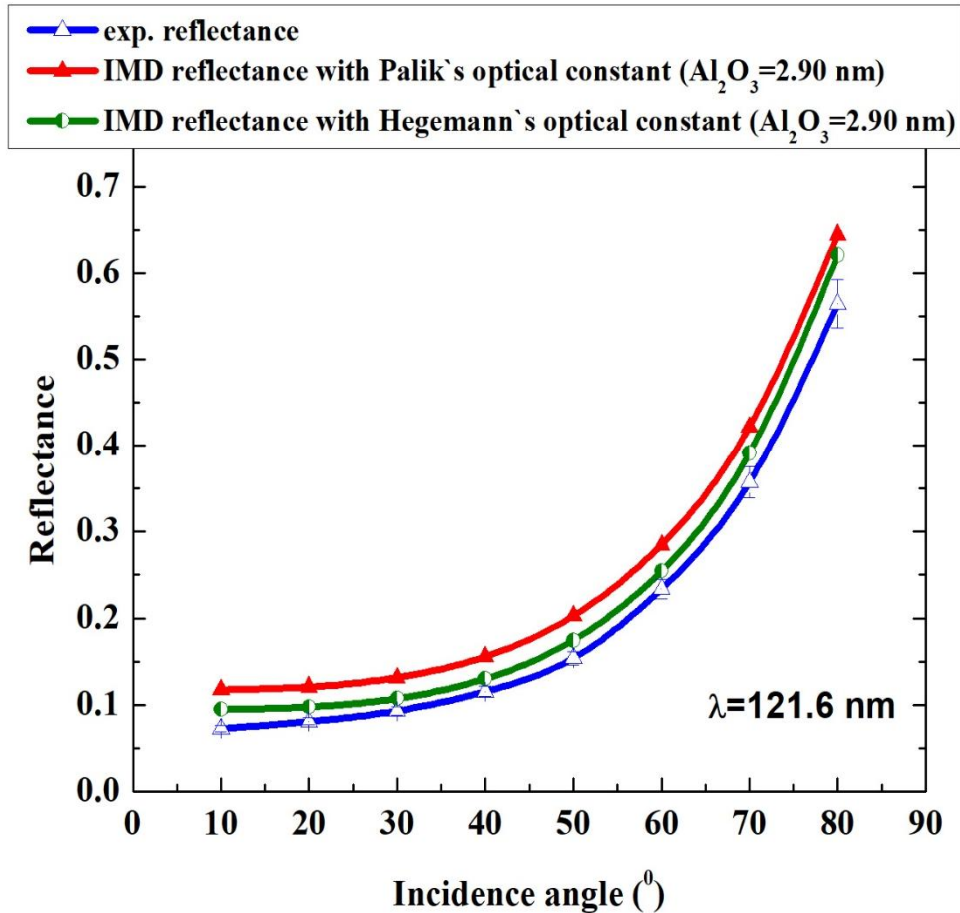


Figure.4.14. Experimental reflectance and simulation of 2.90 nm of (Al_2O_3) on top of the Al film for both optical constants, assuming the structure shown inset of Fig. 4.12 with sharp interfaces.

It is worth mentioning that the proposed method considers the uncertainties presenting the whole system, including the uncertainty associated with the polarization state of the radiation delivered by the EUV ellipsometry system and the error due to the bandwidth of the monochromator. In order to take into consideration the uncertainty due to the monochromator bandwidth error, we simulated the phase difference at different wavelength for each working incidence angle. Fig. 4.15 shows the calculated phase difference derivative against wavelength for the structure shown in the legend of Fig. 4.12 assuming the optical constants reported by Palik. The output results are presented in Table 4.6. we assumed the bandwidth for the monochromator of around 2 nm.

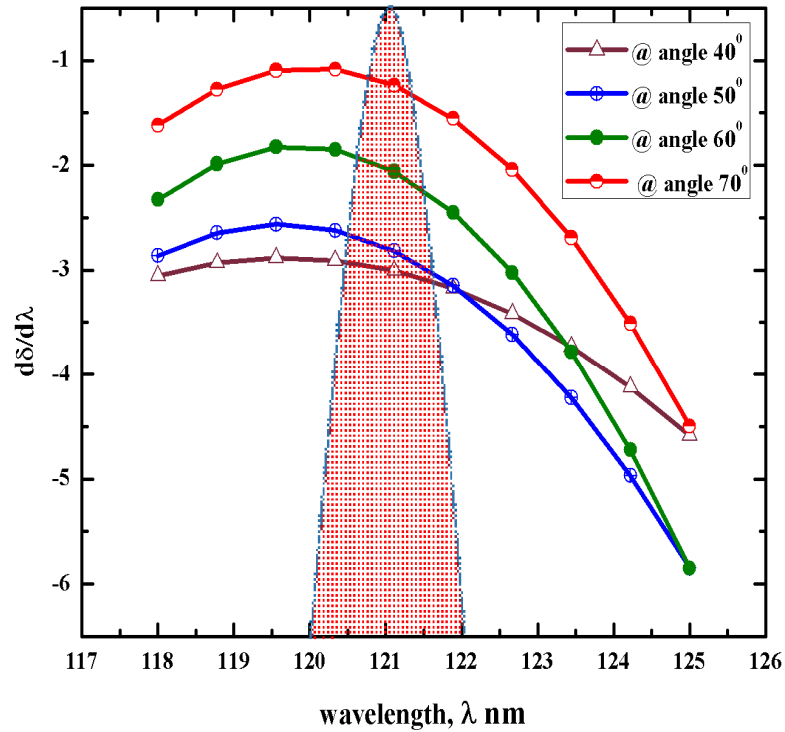


Figure 4.15. The calculated phase difference derivative versus wavelength for the structure shown in the inset of Figure 4.12 with 3.18 nm of (Al_2O_3) on top of the Al .

Table 4.6. The calculated phase difference versus incidence angles at a different wavelength.

Incidence angle/wavelength	$\Delta\delta^{\circ}$					
	118 nm	119 nm	120 nm	121 nm	122 nm	123 nm
40	81	78	75	72	69	66
50	107	105	102	99	96	93
60	130	128	126	124	121	119
70	148	147	146	145	143	142

Concerning the aluminum film, the sample has an oxide layer due to exposure to air as expected. The oxide layer reduces the reflectance of the sample and changes the phase shift properties: for example, the bare Al coating acts as Quarter Wave Plats (QWPS) at 59° incidence

angle, while the sample Al_2O_3/Al is thus for $\sim 47^\circ$. However, the scientific literature [65,68] demonstrated the good stability of this type of sample once the oxide is formed and the sample under investigation exhibits good properties as a phase retarder. The performance strongly depends on the incidence angle as is shown in Fig.4.16 where the first derivative of the simulated phase difference with respect to the incidence angle is reported. It is worth to note that small angular displacements can induce considerable phase deviation. Then an accurate alignment of the sample is required. This is especially true around 47.5° where, as we already said, the sample acts as a QWP with a phase shift of 90° and a ratio close to 1 and where small incidence angle deviation can induce phase variations of about 2.7° .

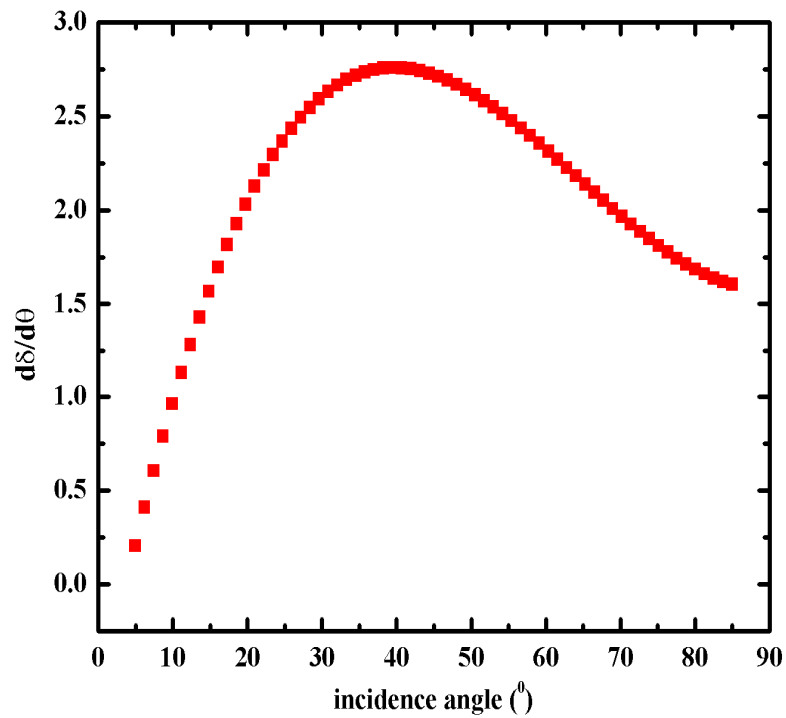


Figure 4.16. Theoretical phase difference derivative is plotted versus the incidence angle for the structure shown in the inset of Figure 4.12 with native oxide layer of 3.18 nm.

4.3. Conclusion

Considering the results presented in this chapter, we can assert that: An ellipsometric method based on the Stokes formalism and Mueller matrices has been tested and experimentally verified. The polarimetric properties of an Al sample with an oxide layer on the top were experimentally tested and characterized by using the proposed arrangement and method analysis. The Al_2O_3/Al

specimen behaves as *QWP* at 47.5° incidence angle and 121.6 nm wavelength. It can be a useful element for implementing optical system devoted to metrology and to change the polarization state of VUV/EUV radiation.

Chapter.5

Quarter Wave Plates Based on *SnTe/Al* bilayer

5.1. Introduction

Quite recently great efforts have been paid to produce circularly polarized light at small-scale experiments [69]. In order to manipulate the circularly polarized beams effectively, it is necessary to develop appropriate optical coatings able to control either the reflectance or the phase retardance using components such as quarter wave plates (QWPs) [70]. Whatever the spectral range, the QWPs convert linearly polarized light to circularly polarized, by introducing a phase difference of $\frac{\pi}{2}$ between the two orthogonal components of the electric field vector, which should remain at equal intensity [71]. Since materials are mostly absorptive in the FUV and EUV spectral regions, it is not trivial to satisfy both requirements. Thus, the availability of high-performance optical coatings for short wavelengths is quite restricted for this reason.

In the previous chapter, we tested the robustness of our reflectometer facility as an EUV ellipsometry system by characterizing a single layer of *Al*, highlighting that one of the problems encountered is the formation of aluminum oxide (Al_2O_3) due to reaction with air [65]. The presence of an oxide layer can strongly affect the optical performances of the film. Then, to preserve the pristine high reflectance of *Al*, a protective capping layer is usually added on the top to avoid the oxidation without affecting the optical throughput.

Fluorides are often used in the design of the FUV optical coatings for this aim [72,73]. MgF_2 and LiF have been and are still often applied as protective capping layer for Al in the 90–130 nm wavelength range although the cut-off, around 115 nm in the case of MgF_2 and 106 nm in the case of LiF which limit their use in some cases. Furthermore, the deposition process of such material requires high heats, which can affect the quality of the coatings underneath; as the material cools, the material stresses through tension [74,75]. Despite these drawbacks and due to the shortage of knowledge of optical constants in the FUV and EUV inhibiting the use of alternative materials, MgF_2 and LiF are widely used in optical components development as well [31,76].

For this reason, we have investigated the realization of a reflective quarter wave plate based on a $SnTe/Al$ bilayer to get uniform high reflectivity with a suitable phase difference between the two reflected s and p perpendicular components. $SnTe/Al$ is a $IV-VI$ narrow bandgap semiconductor with a direct bandgap of 0.18 eV. This material is interesting for applications in infrared photodetector development, laser diode manufacturing and thermoelectric devices [77]. Several deposition methods have been used for $SnTe$ and $SnTe$ alloys, such as molecular beam epitaxy, chemical vapor deposition, and metal organic vapor deposition [78,79]. To our knowledge, the deposition by the electron beam technique has not been so deeply investigated. Furthermore, many fundamental properties of this semiconductor, such as the surface reactivity, remain poorly explored.

The simulations performed by the IMD software [66]; assuming the optical constants of Palik [57]; show that $SnTe$, in principle, does not strongly affect the properties of an Al coating and, if sufficiently resistant to ageing and oxidation, should be considered as a possible capping layer. Figure 4.1 shows the calculated reflectivity over a wide spectral range versus incidence angle for a 3 nm capping layer of $SnTe$ on top aluminum. In this case, the efficiency is nearly uniform for the inter spectral range. Thus, we fabricated the $SnTe/Al$ bilayer by electron beam deposition and characterized its optical performance.

Furthermore, the experimental characterization of phase retarders and QWPs is a rather difficult task to be performed in the FUV–EUV spectral range. At visible wavelengths, a common method is based on interferometric techniques [80], but these procedures are not easily achievable for shorter wavelengths. Total electron yield and reflectance measurements can also be combined and properly analyzed to retrieve the phase [81]. This last approach, suitable only in the case of

conductive materials, is not readily achievable in the laboratory and requires beam time approval at synchrotron large-scale facilities.

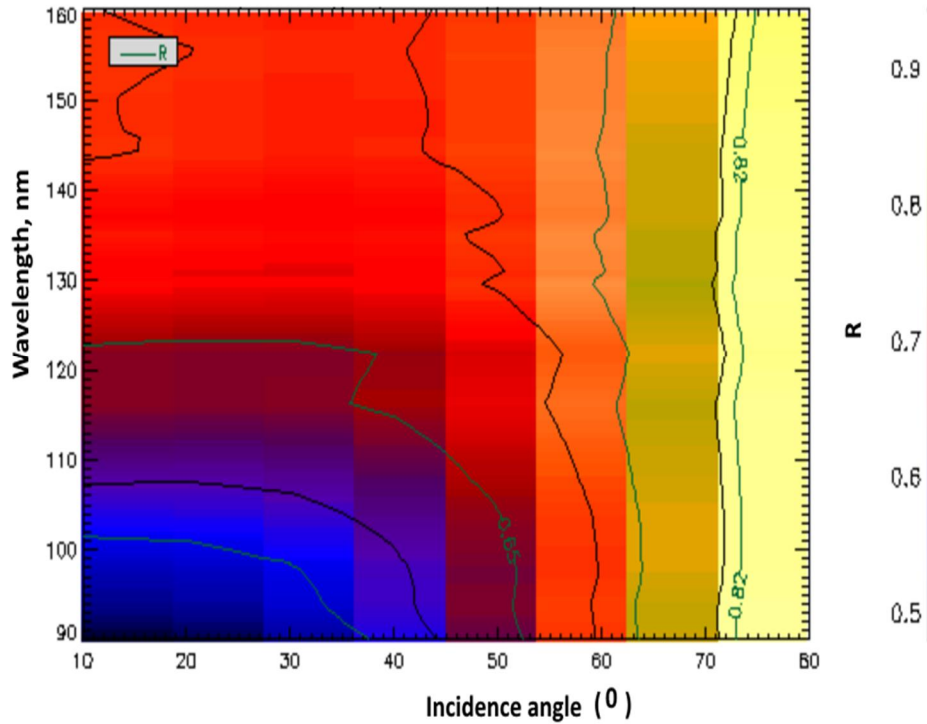


Figure 5.1. The calculated reflectivity for unpolarized light over a wide spectral range versus the incidence angle of 3 nm capping layer of *SnTe* on top of aluminum.

5.2. Experimental Methods

SnTe has been used as a capping layer for *Al* coatings. We deposited two different thicknesses of capping layer i.e. 3 nm, and 6 nm for different samples but unfortunately the deposition quality of the 3 nm capping layer was not good, so we decided to continue our research only for 6 nm *SnTe* as the capping layer. The nominal structure of the *SnTe/Al* sample is shown in Fig. 5.2. It consists of a 80 nm thick aluminum layer deposited by e-beam evaporation on a Si substrate; 3 nm of Cr was deposited between the aluminum coating and the Si substrate as an adhesion layer. The structure was capped with 6.2 nm of *SnTe*.



Figure 5.2. The nominal structure of the sample as monitored with a quartz microbalance during the deposition.

The specimen was fully characterized by means of polarimetric measurements using the improved EUV reflectometer located at the Institute for Photonics and Nanotechnology Padova. In this experiment, the FUV radiation was produced by a deuterium lamp with an MgF_2 window emitting the strong line at 121.6 nm.

The polarimetric measurements allow the detection of the ellipsometric parameters r and δ . The optical scheme of the experimental arrangement is shown in Fig. 5.3. The experimental chamber can be rotated around the direction of the propagating beam in order to change the angle between the incidence plane and the polarization direction of the radiation. As it was shown in the previous chapter that the radiation delivered by the system is nearly fully linearly polarized (92%), the equipment was configured to deliver nearly linearly polarized light at (-45°) w.r.t incidence plane [64]. The radiation reflected by the sample under investigation goes through the rotating analyzer. Then, it is collected by a channel electron multiplier (CEM) working in photon counting mode. The polarized reflectivity of the sample was investigated at several incidence angles between 40° to 70° . At each incidence angle, the analyzer was rotated from 0° to 360° in steps of 10° . The analysis that we performed is based on the Stokes vectors and Müller matrix formalism.

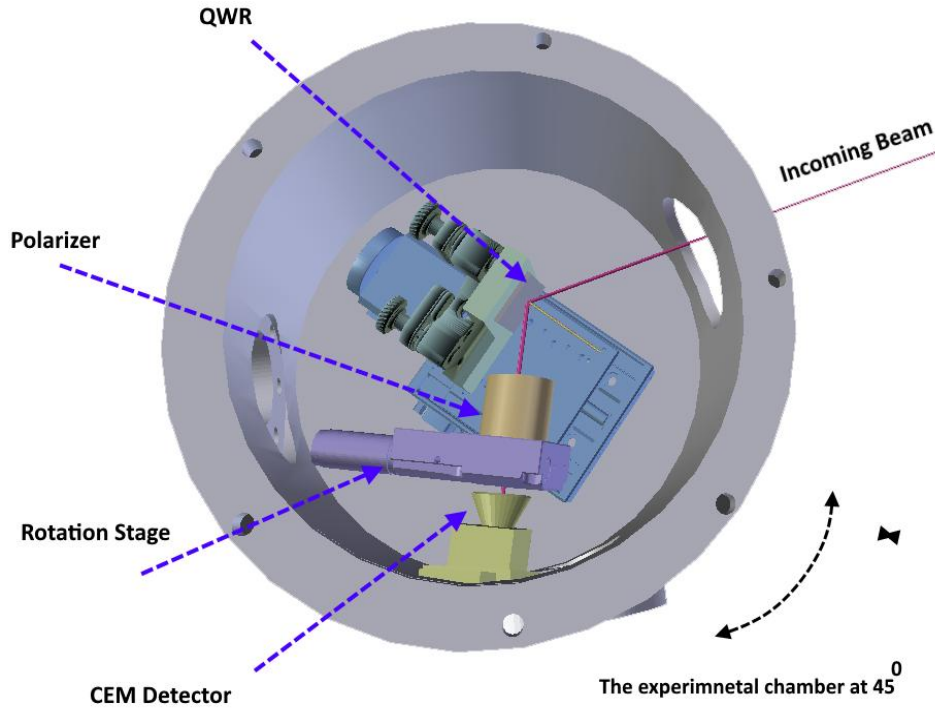


Figure 5.3. The set-up arrangement for testing the QWRs, the testing chamber was rotated by 45° with respect to the incidence plane.

The polarimetric analyzes of the sample were investigated at several incidence angles between 40° and 70° for the wavelengths of at 121.6 nm and 160 nm . The analysis that we performed is also based on the Stokes vectors and Müller matrix formalism. Concerning the reflectance measurements, they were performed by removing the polarizer and directly collecting the beam reflected by the sample. Further investigations have been performed at the *ELETTRA* synchrotron-*BEAR* beamline in Trieste [82] to characterize the optical properties of the *SnTe* and compare the results with those reported by Palik [57].

5.3. Structural Characterization

Since *SnTe* is rarely employed in the FUV and EUV applications, before commencing the study of the QWP performance in details, we undertook a complete characterization of the *SnTe* and *SnTe/Al* samples. The properties of the optical coatings in these spectral ranges are often retrieved by analyzing the reflectance data or by combining reflectance and transmittance measurements with the optimization of proper fit procedures [8]. Such an approach has been

applied in the study of optical constants and properties of thin films, although the analysis of reflectance or transmittance is often not enough to gather full knowledge [83]. For example, the determination of the phase difference introduced by an optical element is one of the optical properties that cannot be determined by analyzing only the reflectance data [84].

We firstly characterized thick layers of *SnTe* to retrieve the n and k values at 121.6 nm. For this purpose, two samples of 50 nm and 100 nm thicknesses *SnTe* were deposited on a silicon substrate using the same deposition system. The reflectance measurements performed at the BEAR beam-line were analyzed [82]. We fitted the experimental data using the IMD software [66]. As before the fitting procedures use the Levenberg-Marquardt algorithm to calculate the fit parameters according to the χ^2 . The experimental and fitted reflectance for the two samples is shown in Fig.5.4a and Fig.5.4b, respectively.

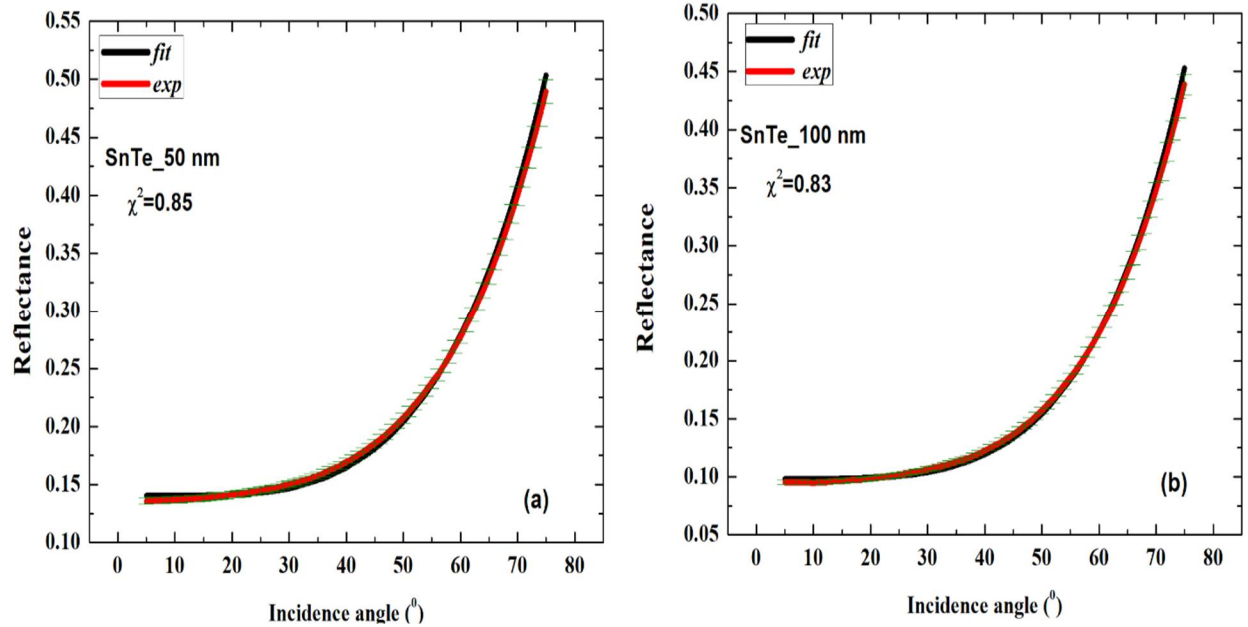


Figure 5.4. Experimental reflectance for unpolarized incident beam at wavelength of 121.6 nm; fitted and measured curves for the two samples structure.

The optical constants retrieved by the fitting are listed in Table 5.1 together with the optical constants available in the literature [57]. We immediately observe that n and k are not unequivocally determined, as their values slightly change depending on the sample thickness and history.

Table 5.1. The optical constants of *SnTe* at a wavelength of 121.6 nm are collected from different literature sources.

Optical constant of <i>SnTe</i> at a wavelength of 121.6 nm	<i>n</i>	<i>k</i>	χ^2
<i>SnTe</i> layer of 50 nm thickness	0.87	0.75	0.85
<i>SnTe</i> layer of 100 nm thickness	0.94	0.64	0.83
Palik [57]	0.78	0.93	-
Schoolar and Dixon [57,85]	0.68	0.90	-

Referring to the *SnTe/Al* specimen, we performed specular reflectance measurements for the sample at 121.6 nm in two mutually orthogonal configurations of the experimental chamber to determine the reflectance of the specimen for un-polarized light. We used anyway both set to simulate the nominal structure (see Fig. 5.5) and we observed that the experimental trend does not match the theoretical curve. This result confirms that the nominal structure is not the real one.

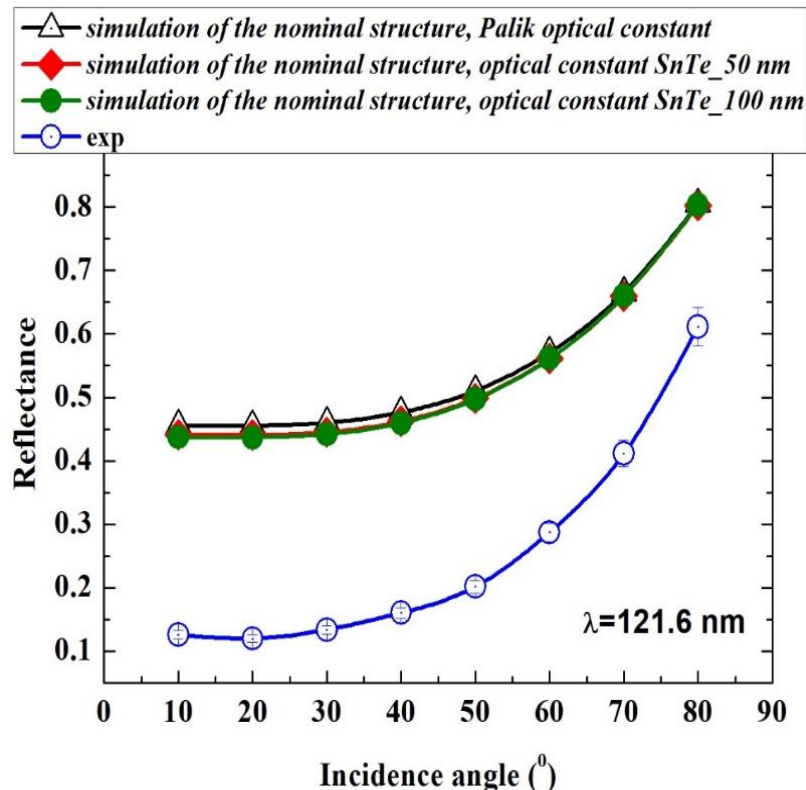


Figure 5.5. Experimental reflectance and simulated curves of the nominal structure refer to the sample as described in Fig.5.2.

Accordingly, three possible designs can be reasonably considered: the first one accounts a carbon contamination on the top layer, the second, the formation of an aluminum oxide interlayer between the *SnTe* and *Al* coating, and the third one a combination of both:

- i. $a - C(xnm)/SnTe(xnm)/Al(80nm)/Cr(3nm)/Si$
- ii. $SnTe(xnm)/a - Al_2O_3(xnm)/Al(80nm)/Cr(3nm)/Si$
- iii. $a - C(xnm)/SnTe(xnm)/a - Al_2O_3(xnm)/Al(80nm)/Cr(3nm)/Si$

It is well known that vacuum pressure, deposition conditions, air exposure and handling can strongly affect the properties of optical coatings [74]. The presence of carbon has already been observed in *SnTe* coatings and could be mainly due to contamination during deposition and handling [86]. An aluminum oxide interlayer in *MgF₂/AL/MgF₂* stack has been observed by Kim et al. [26], even in case of high vacuum deposition process. Then, the options are therefore equally reasonable. Fig. 5.6 shows the experimental and fitted reflectance for the supposed structures. The thicknesses of the layers determined by the fitting procedure are given in the legend of Fig. 5.6. In case of the design that includes both contaminations, we report only one of the fitted curves. It has been selected according to the data in Table. 5.2; analysis and results will be described further below. The approach adopted for defining the structure (iii) was to select different intervals of existence (I.E.) and starting guess (S.G.) in the fit procedure. All the parameters are listed in Table. 5.2 together with the determined thicknesses for $a - C$ and $a - Al_2O_3$ and the χ^2 . We can conclude that:

- The thickness of $a - Al_2O_3$ ‘tends’ to reach the lowest value of the selected I.E.
- by increasing the lower limit of the I.E., the χ^2 increases.

Considering the obtained results, the χ^2 values, and the fitted curves the following structures could be acceptable:

- i. $a - C(2.74nm)/SnTe(7.5nm)/Al(80nm)/Cr(3nm)/Si$
- ii. $SnTe(8nm)/a - Al_2O_3(2.41nm)/Al(80nm)/Cr(3nm)/Si$
- iii. $a - C(> 2.5nm)/SnTe(8nm)/a - Al_2O_3(\leq 0.5nm)/Al(80nm)/Cr(3nm)/Si$

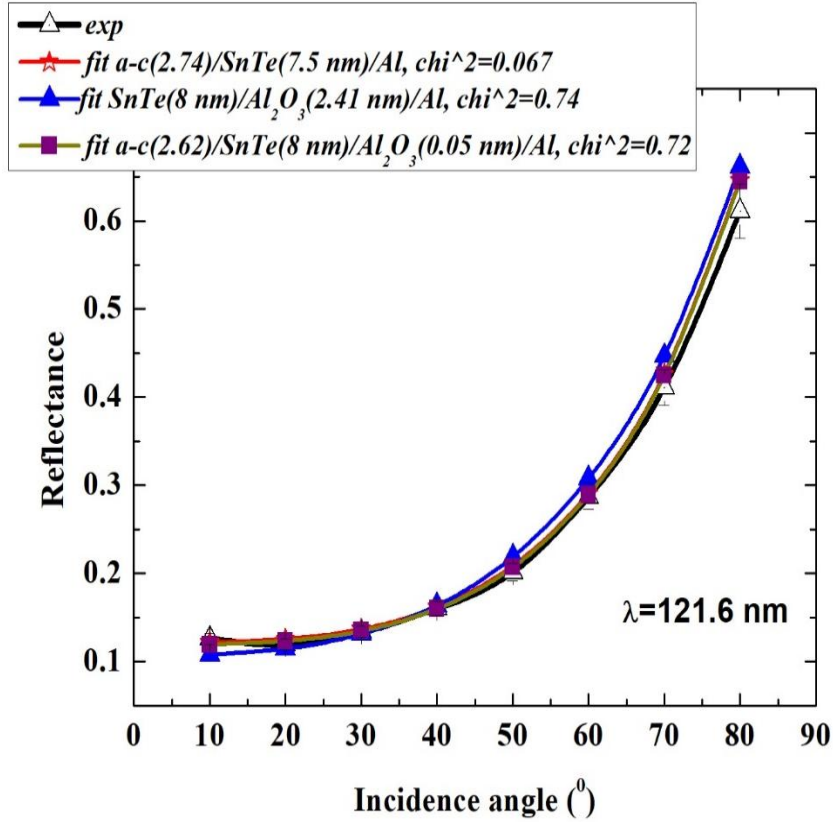


Figure 5.6. The experimental and fitted reflectance of the proposed structures.

Table 5.2. The output parameters obtained from the fitting procedures: where I.E. the interval of existence, S.G. refers to the starting guess, and F.V. to the final value of the thickness obtained by the fit procedure.

<i>a - C</i>			<i>SnTe</i>			<i>a - Al₂O₃</i>			
I.E. (nm)	S.G. (nm)	F.V. (nm)	I.E. (nm)	S.G. (nm)	F.V. (nm)	I.E. (nm)	S.G. (nm)	F.V. (nm)	χ^2
0.05-3	1.5	2.62	5-8 nm	6	8	0.05-3	1.5	0.05	0.729
0.1-3	1.5	2.56	5-8 nm	6	8	0.1-3	1.5	0.1	0.761
0.5-3	1.5	2.17	5-8 nm	6	8	0.5-3	1.5	0.5	1.07
1-3	1.5	1.65	5-8 nm	6	8	1-3	1.5	1	1.52

Considering the results shown in Fig. 5.6 and Table 5.2, the reflectance data are not sufficient to discriminate between the proposed models. All they are plausible, since they satisfy the

experimental reflectance curve. We will see hereinafter that the ellipsometric measurements as well as providing a characterization of the QWP throughputs will help to settle between the possible options.

The fitted and measured polarimetric curves at different incidence angles on the sample are shown in Fig.5.7 and Fig. 5.8. The output intensity at each angle was recorded versus the rotation angle of the polarizer. The polarimetric data were then used to retrieve the ellipsometric parameters of the sample by using the MATLAB code developed according to Eq. (4.11) and based on the Levenberg–Marquardt algorithm. We performed the fitting procedure 300 times by randomly changing the starting guess of the parameters between the defined intervals of existence to test the robustness of the fitting procedure. The output values of the ellipsometric parameters, r , and δ , of the sample at each incidence angle are reported in Table.5.3 together with the errors. In determining the uncertainty, it was assumed to consider the standard deviation obtained in the fitting procedure for the phase, while for the ratio, which can also be measured by reflectance, the error reported in the table is the experimental one.

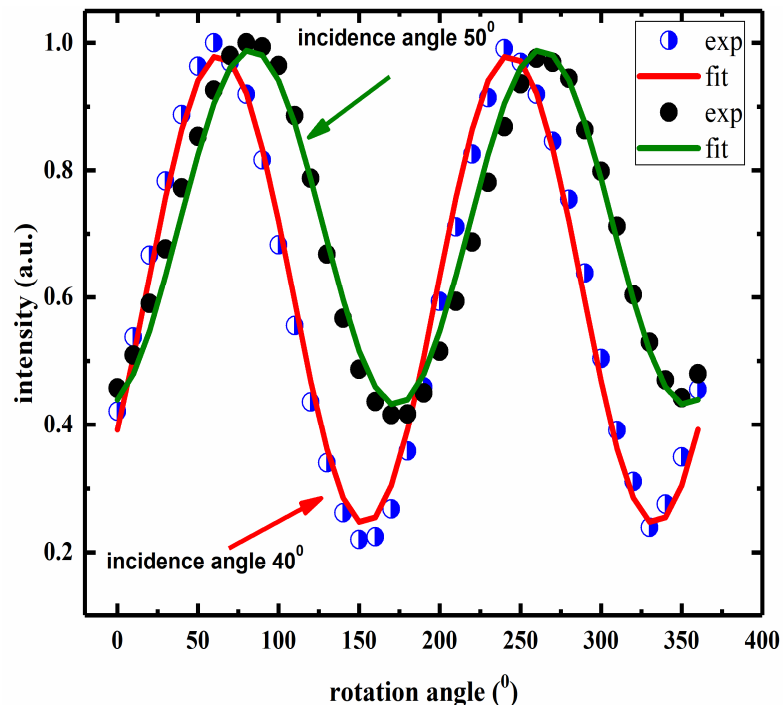


Figure 5.7. Measured and fitted data for the *SnTe/Al* specimen at two different incidence angle 40° and 50° .

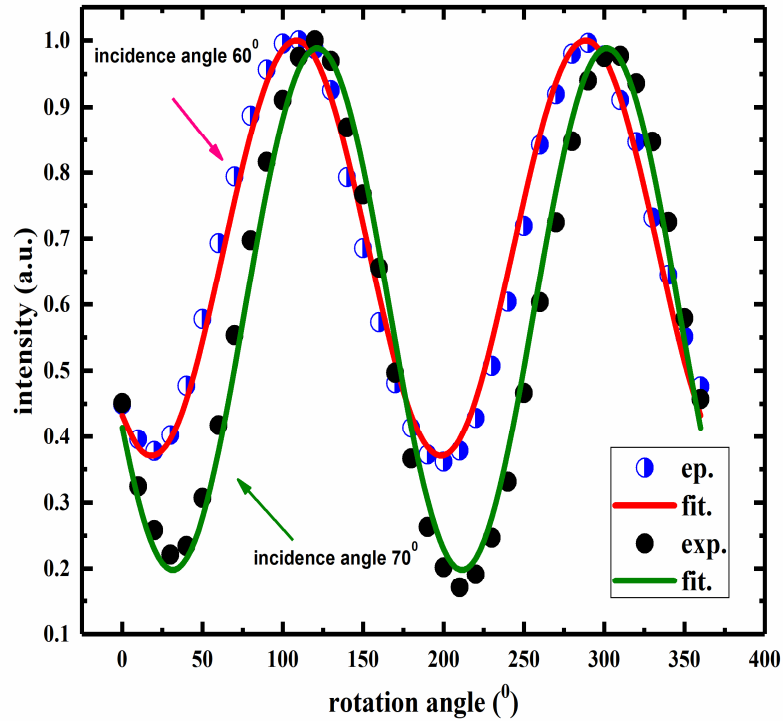


Figure 5.8. Measured and fitted data for the $SnTe/Al$ specimen at two different incidence angle 60° and 70° .

The ellipsometric parameters obtained by the fit of the ellipsometric data are compared with those retrieved by the IMD simulation software for the structures satisfying the experimental reflectance throughputs in Fig.5.6 and defined by the thickness values in Table 5.2. The Phase and ratio for all the structures are reported in Table 5.3. In addition, the values of simulations corresponding to the presence of only a-C layer or a $-Al_2O_3$ layer are reported.

Table 5.3. The fitted parameters obtained by ellipsometric measurements compared with those retrieved by IMD software.

Incidence angle	a-C 2.74 nm & a- Al_2O_3 0 nm		a-C 2.62 nm & a- Al_2O_3 0.05 nm		a-C 2.56 nm & a- Al_2O_3 0.1 nm		a-C 2.17 nm & a- Al_2O_3 0.5 nm		a-C 1.65 nm & a- Al_2O_3 1 nm		a-C 0 nm & a- Al_2O_3 2.41 nm		ellipsometric measurements	
	ratio	phase ($^\circ$)	ratio	phase ($^\circ$)	ratio	phase ($^\circ$)	ratio	phase ($^\circ$)	ratio	phase ($^\circ$)	ratio	phase ($^\circ$)	ratio	phase ($^\circ$)
40	0.74	58	0.73	58	0.73	57	0.71	58	0.69	58	0.63	56	0.74±0.01	58±6
50	0.73	85	0.71	84	0.71	85	0.70	85	0.67	85	0.60	84	0.72±0.01	84±6
60	0.75	111	0.74	110	0.74	111	0.73	111	0.71	112	0.65	111	0.73±0.01	108±7
70	0.82	136	0.81	135	0.81	136	0.80	136	0.79	136	0.74	136	0.80±0.01	129±6

We can observe that the ratio r and the phase δ are in close agreement with the structures accounting of more than 2.5 nm of a-C contamination and sub-nanometer interlayer of $a - Al_2O_3$ between $SnTe$ and Al (three columns, left side of the Table 5.3). In particular, the drop observed in the experimental reflectance throughput are mainly due to the presence of a-C on the top of the sample, although a slight oxidation of the aluminum can be considered. On the other side, we observe that by increasing the thickness of the $a - Al_2O_3$ and decreasing the thickness of a-C, only the phase agrees with the ellipsometric results. By summarizing the main achievement of this study, we can state that the structure that better describes the sample is:

$$a - C(2.74 - 2.56 \text{ nm})/SnTe(7.5 - 8 \text{ nm})/a - Al_2O_3(0 - 0.5 \text{ nm})/Al(80\text{nm})/Cr(3\text{nm})/Si$$

The thickness ranges consistent with the analysis are in the brackets and allow to evaluate the sensitivity and accuracy of the proposed method in determining the structure of the sample.

To reinforce the conclusions derived from these results, we performed further optical investigation in-house by using the same facility and the same spectral lamp and by selecting 160 nm wavelength. Fig. 5.9 shows the measured reflectance and the simulation of the supposed models. The conclusions derived by the ellipsometric method are here confirmed: the curves that better approach the experimental data are those referring to the structure contaminated by a-C and accounting a possible sub-nanometer interlayer of $a - Al_2O_3$.

The discrepancies between the measured values and the simulated ones can be reasonably attributed to the set of the optical constants used in the fitting. As noted, the optical constants strongly depend on the sample's history, thus they can affect, for example, the exact determination of the layer thickness and the simulation of the optical throughput. The optical constants of the $SnTe$ at 160 nm have been extracted from the Palik optical constants book [57].

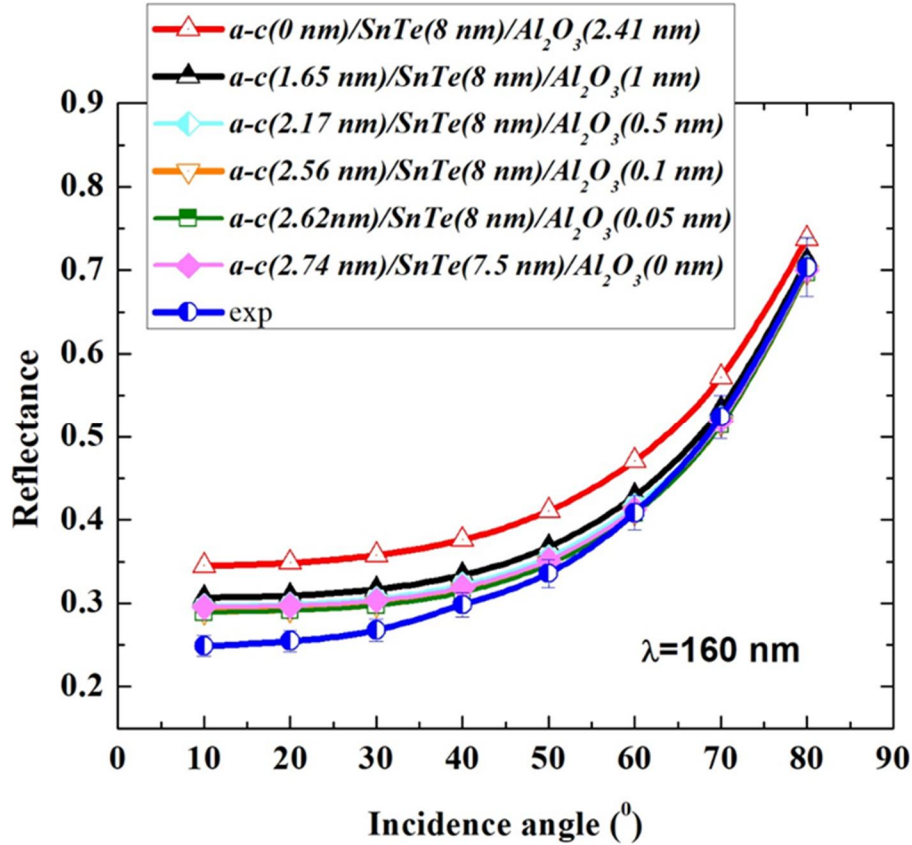


Figure.5.9. The specular reflectance measurements and simulation by IMD of the possible structures at a wavelength of 160 nm assuming extrapolated Palik's optical constants and sharp interfaces [57].

Concerning the study of the *SnTe/Al* as a QWP, the phase difference introduced by the sample on the *s* and *p* components is shown in Table 5.3. It is worth to note that around 55° the specimen under investigation retards the components by ~90°, although the ratio is 0.74 and not 1 as required. We have recently published a study describing the performances of QWP based on a single layer of *Al*, inevitably covered by a native oxide layer [64]. In terms of performance, the pure *Al* with a native oxide layer on the top seems to show better performance as a QWP than the *SnTe/Al*. By observing Fig. 5.10a), we note that the phase difference can be easily tuned for both structures, by adjusting the incidence angle to set the required 90°.

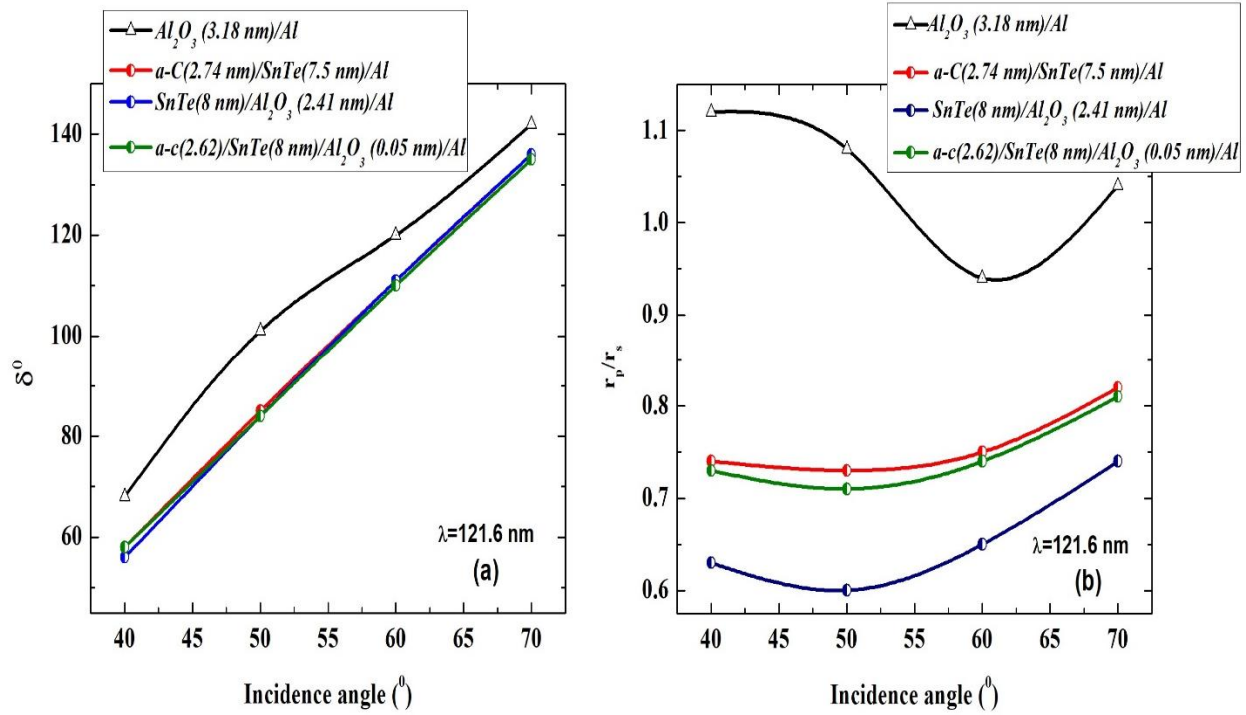


Figure. 5.10. (a) phase and (b) ratio introduced by the proposed two structures compared with a single layer of aluminum with native oxide layer of 3.18 nm.

5.4. Conclusion

In summary, the *SnTe/Al* bilayer was fully characterized, and its structure determined with low uncertainty. The model that better describes the sample accounts of a-C contamination on the top and sub-nanometer *a* – Al_2O_3 layer between the *SnTe* and the Al underneath. The contaminations compromise the performances of the sample as QWP, then, if the phase retarder can be properly selected by changing the incidence angle on the sample, for the ratio, that is required to be ~ 1 , this is not possible. The comparison of the present sample with a specimen based on a single layer of aluminum exposed to the environment and then oxidized, shows that, despite the oxidation, the performance of single aluminum is better than the present sample. However, although the sample's performances are not as expected, it still behaves as a good phase retarder. Moreover, this study clearly shows that, by opportunely combining reflectance and ellipsometry measurements, it is possible to characterize in laboratory the optical properties and structures of mirrors, polarizers and phase retarders.

Chapter.6

Thesis Summery

Ellipsometry is one of the promising and leading technology which is developed for material science analyses; it can be considered as multipurposes technique provides a lot of information about the structural properties and optical characterization of materials.

Within the framework of the presented thesis, multi-angle FUV-EUV reflectometer facility has been implemented and characterized as an ellipsometric system for polarimetric measurements in the spectral range between 90 and 160 nm. The FUV-EUV reflectometer facility available in the Institute for Photonics and Nanotechnologies-CNR Padua, Italy has been coupled with a four reflection EUV linear polarizer designed in our laboratory in order to be used as a tabletop EUV ellipsometry system. The proposed method is suitable to be used for the study of the physical and structural properties of any FUV/EUV reflective coating as discussed by studying the Al and SnTe/Al samples. Obviously, complex studies require proper ellipsometric models in order to rightly interpret the experimental data and derive the desired parameters.

The method based on the Stokes parameters and Mueller matrices formalism has been successfully applied to characterize different sample's surface contamination. The proof is the experimental results described in this thesis about the properties of the aluminum optical coating with a native oxide layer: the oxide layer thickness was determined by fitting the phase retrieved from the ellipsometric measurements. Furthermore, the $\text{Al}_2\text{O}_3/\text{Al}$ specimen behaves as QWR at 47.5° incidence angle and a wavelength of 121.6 nm. The specimen can be used for implementing optical system devoted to EUV metrology and to manipulate the polarization state of FUV/EUV radiation.

The other study proposed in this thesis comes from the desire to explore new optical materials employed as capping layer for optical coatings in the vacuum ultraviolet (VUV) and extreme ultraviolet (EUV) spectral regions. The materials are mostly absorptive in these spectral regions, thus the availability of high-performance optical coatings for the short wavelengths is quite restricted for this reason.

we presented a phase retarder optical component based on SnTe/Al bilayer covering the spectral range between 90 nm and 160 nm. The specimen has been fully characterized at hydrogen Lyman alpha line (121.6 nm) in terms of reflectance and ellipsometric parameters, i.e. the ratio r , ratio of the Fresnel coefficient, and the phase difference δ introduced between the -s and -p reflected components.

To our knowledge, such structure based on SnTe compound hasn't been studied as capping layer for a wide spectral range in the vacuum ultraviolet, although the throughputs are not those expected for this structure. The drop-in performances are attributed to a-C contamination on the top and sub-nanometer Al_2O_3 layer between the SnTe and the Al underneath. The real structure of the sample has been identified by performing additional reflectance measurements at 160 nm wavelength. The results also confirm the potentialities and the advantages of such non-invasive optical approach.

Regarding the optimization of data acquisition, The FUV-EUV ellipsometric system presents the greatest potential for more precise reconstruction of layer structures and thin films investigation. The system can be a very promising laboratory equipment, and a simple alternative tool for fast and preliminary experiments compared to measurements sessions at large scale facilities. It is suitable to characterize phase retarders, polarizers and other optics in the EUV region as it has been proved for the sample under investigation.

Appendices

Appendix A. Deposition Facilities

The work carried out in this thesis have been done using different equipment and experimental facilities, which will be described throughout this part. This part shows the main features of the deposition techniques used to develop our optical coating mirrors.

Thin film deposition techniques

Many techniques have been developed and used for thin film deposition, some of them have been explored extensively, while others have attracted less attention. EUV mirrors require a dedicated deposition technique capable of delivering high-quality thin films by controlling the thickness and the purity of the films. In fact, thin films growth at crystals surfaces or interfaces, including the nucleation process on a substrate like all phase transformation. The nucleation growth is well explained through three modes Island or Volmer-Weber growth, Frank–van der Merwe (layer-by-layer) and Stranski–Krastanov (layer-plus-island) [87]. The nucleation process has a serious effect on the overall quality of the resultant film; it plays a pivotal role in determining the crystallinity and microstructure. In practice, the interaction between the film and substrate plays a very important role in determining the initial nucleation and the film growth[87].

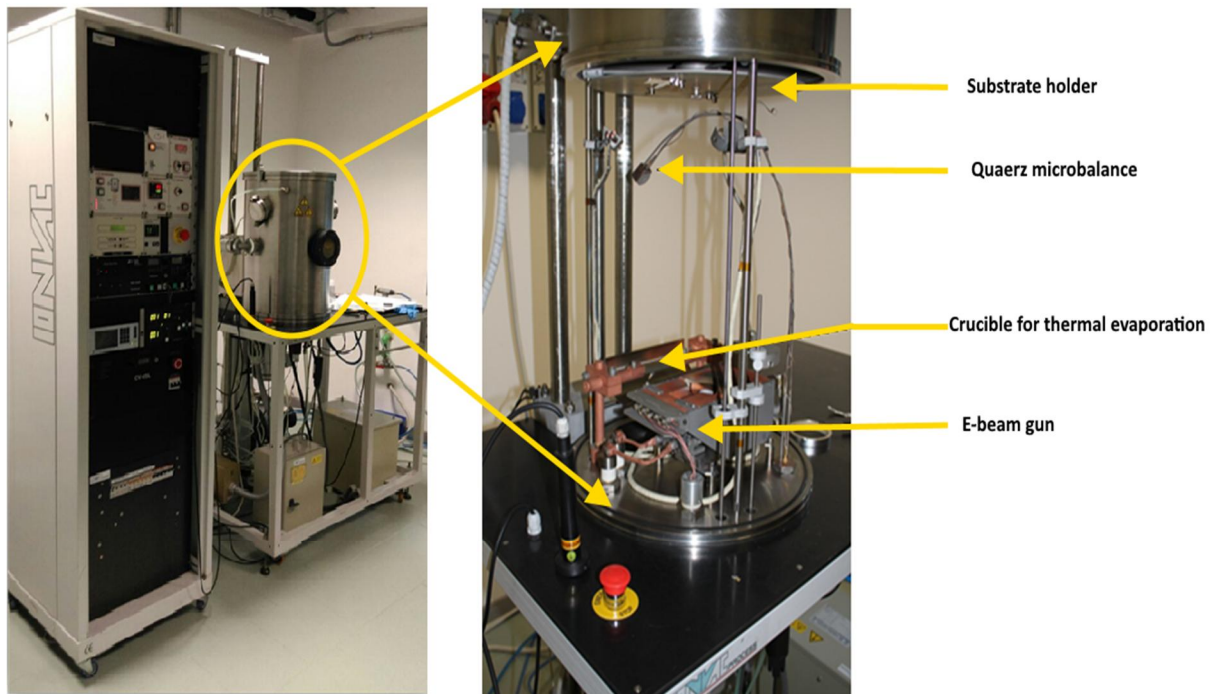
In general, physical vapor deposition is the common way to deposit thin films and multilayers with finite thickness; the basic idea is to create a vapor. Usually, the vaporization process can be achieved through electron acceleration or by heating the material to the melting point via electric current as in thermal evaporation technique [88]. The samples that have been investigated in this thesis were deposited in a high vacuum deposition facility. At CNR- IFN, Padova, two deposition facilities are currently in use; INOVAC electron-beam evaporator and the sputtering deposition facility.

Electron beam evaporation

The main feature in electron beam evaporation is the electron source which generates electrons through thermionic emission or field electron emission method, accelerates them as electron beam,

and focus them via electric and magnetic fields into the crucible section that holds the evaporated material.

A typical diagram of an E-beam evaporator facility available at our disposal is shown in Fig. A.1 the E-beam facility consists mainly of two sections; an electron source (electron gun) and the deposition chamber. The deposition chamber section is a low-pressure chamber it was pumped using a high vacuum Varian turbomolecular pump in series with a scroll pump. The substrate is placed at 40 cm distance from the target materials on a rotting plate to assure homogenous distribution of the thickness all over the deposited area. The substrate is shielded from the target by a shutter, which is opened when a stable flux is achieved. The shutter is again closed when the required layer thickness is achieved. The deposition rate is monitored during the evaporation process via a quartz-crystal monitor. However, the deposition rate usually fluctuates since the vapor pressure is highly dependent on small changes in temperature and morphology of the target that occur over time.



(a) External view of the e-beam evaporation system

(b) Internal view of the evaporation chamber

Figure A. 1: a) Image of the structure of an electron beam evaporation device IONVAC e-beam and Joule evaporation system at CNR- IFN, Padova, b) internal view of the deposition chamber.

Thermal evaporation

The electron-beam facility which is located in CNR is adapted to work with thermal evaporation regime, in conventional thermal evaporation, the material to be deposited is heated to the melting temperatures until a suitable vapor pressure is created. The materials are placed on a source of evaporation like a boat or filament by which an electric current of great intensity is circulated so that its temperature is increased by Joule effect. Typical materials used for sources of evaporation are high melting point metals, such as tantalum, molybdenum, and tungsten (3290 K, 2896 K, and 3683 K, respectively). The choice of source material will depend on the nature of the material to be evaporated, to avoid, as far as possible, the formation of alloys with lower evaporation temperature. Fig. A.2 shows an outline of this technique of thin film deposition.

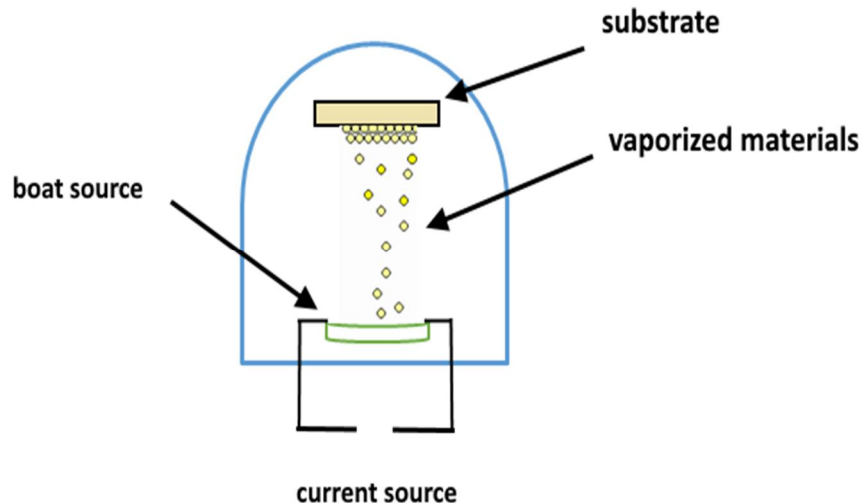


Figure A.2 The basic principle of the thermal evaporation technique.

Magnetron sputtering

The other deposition techniques available in our laboratory is the RF magnetron sputtering. In magnetron sputtering, positively and negatively ions are created usually using a plasma of an inert gas such as argon, the positively charged ions from the plasma are accelerated to the

negatively charged electrode or "target material." via an electrical field. The positive ions are more energetic enough to strike the surface of the target material ejecting its atoms.

The ejected atoms emigrate the target surface haven't any charge and can travel without affected by the magnetic field inside the deposition chamber to be condensed on a substrate that is placed near to the magnetron-sputtering cathode. Fig A.3a illustrates the deposition mechanism by magnetron sputtering.

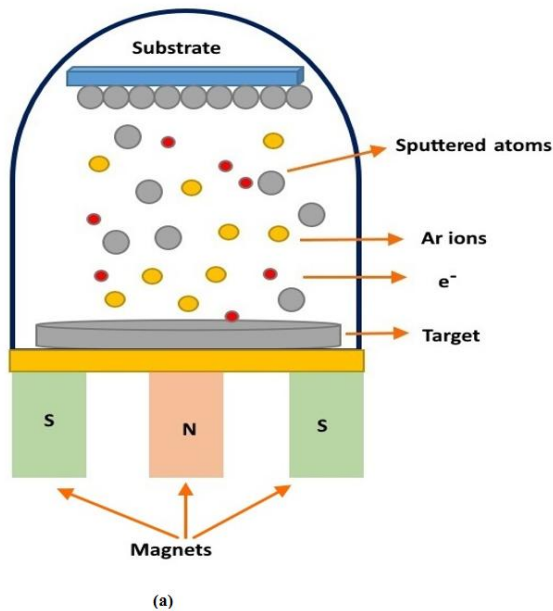


Figure A.3a) The basic principle of the sputtering deposition technique, b) Typical diagram of the Magnetron sputtering facility located at CNR-Padova, Italy.

In CNR, the facility is equipped with two target holders of 4-inch diameter, that can be operated alternatively producing multilayers of two different materials. The oscillating signal is controlled via radio frequency generator that produces 600 W impulses at 13.56 MHz to manage the sign of the anode-cathode bias that generates the plasma; the magnetron utilizes strong electric and magnetic fields to confine charged plasma particles close to the surface of the sputtered target. A typical diagram for the Magnetron sputtering facility is shown in Fig.A.3b.

Appendix B. MATLAB Code

1. The developed MATLAB Code which is used to determine the Stokes parameters

```
clc;
clear all;

%121.6 nm
load XY121.txt;
z = XY121(:,1);
xdata = pi * z/180.;
ydata = XY121(:,2);
M = max(ydata);
ydata = XY121(:,2)./M;
figure;
plot(xdata, ydata, 'b', 'LineWidth', 1.5);
axis([0 2 * pi 0 1.005]);
xlabel('rotation angle (rad)', 'FontSize', 12);
ylabel('intensity(a. u.)', 'FontSize', 12);
hold on;

x0 = [1; -0.0001; -0.8]; %starting guess
lb = [20; -1; -2]; %low constraints
ub = [10000; 1; 1]; %up constraints
Rs = 0.42^4; %IMD ^4 121.6 nm
Rp = 0.074^4; %IMD ^4 121.6 nm

myfun = @(x, xdata)(x(1) * 0.5 * ((Rs + Rp) + (Rs - Rp) * cos(2 * xdata) * x(2)
+ (Rs - Rp) * sin(2 * xdata) * x(3))); % x(1) coefficient; x(2)
= S1; x(3) = S2;
x = lsqcurvefit(myfun, x0, xdata, ydata, lb, ub);
[x, resnorm] = lsqcurvefit(myfun, x0, xdata, ydata);
F = (x(1) * 0.5 * ((Rs + Rp) + (Rs - Rp) * cos(2 * xdata) * x(2) + (Rs - Rp) * sin(2
* xdata) * x(3)));

plot(xdata, F, 'r', 'LineWidth', 1.5);
legend('exp', 'fit');
```

2. The developed MATLAB Code which is used to retrieve the ellipsometric parameters

$$\tan\psi = \frac{r_p}{r_s} \quad \Delta = \delta_p - \delta_s$$

```
clc;
clear all;

load A.txt; % A is the file name (remember to change for each sample)!!!
z=A(:,1);
xdata= pi*z/180.;
ydata=A(:,2);
M=max(ydata); %max exp data
m=min(ydata); %min exp data
ydata=A(:,2)/(M);

Rs=(0.42)^4; %gold
Rp=(0.074)^4; %gold
DR=Rs-Rp; %gold
R=Rs+Rp; %gold

l1=10; %To be changed for each sample
l2=0.82; %To be changed for each sample
l3=0; %To be changed for each sample
l4=-0.08;

u1=500; %To be changed for each sample
u2=1; %To be changed for each sample
u3=pi;%To be changed for each sample
u4=0.08;
s=400;

% x1=40;
% x2=0.6;
% x3=1;
% x4=0.2;

r=rand(s,1);
m=100;

for n=1:1:m

    x1(n)=l1+(u1-l1).*r(n);
    x2(n)=l2+(u2-l2).*r(100+n);
    x3(n)=l3+(u3-l3).*r(200+n);
    x4(n)=l4+(u4-l4).*r(300+n);

end
```

```

y =[x1' x2' x3' x4']; %starting guess
x0 =y'; %starting guess

lb= [11;12;13;14]; %low constraints
ub= [u1;u2;u3;u4]; %up constraints

% lb= [30;0.5;0;-0.4]; %low constraints
% ub= [50;1;pi;0.4]; %up constraints

myfun=@(x,xdata)((x(1)/4.)*(R*((x(2))^2+1)+DR*((x(2))^2-
1)*cos(2*xdata)+(R*((x(2))^2-1)+DR*((x(2))^2+1)*cos(2*xdata))*(-
0.0793)+2*DR*cos(x(3))*x(2)*sin(2*xdata)*(0.902)+2*DR*sin(x(3))*x(2)*sin(2*xdata)*x(4));% function for fitting; S0=1; S3=0.92; rp/rs=x(2) sample;
phi=x(3); x(4)=S3; x(1)=normalization factor %low constraints
options=optimset('Display','Iter','TolX',1e-16);

p1= lsqcurvefit(myfun,x0(:,1),xdata,ydata,lb,ub,options); %only in
case of fit with constraints
p2= lsqcurvefit(myfun,x0(:,2),xdata,ydata,lb,ub,options);
p3= lsqcurvefit(myfun,x0(:,3),xdata,ydata,lb,ub,options);
p4= lsqcurvefit(myfun,x0(:,4),xdata,ydata,lb,ub,options);
p5= lsqcurvefit(myfun,x0(:,5),xdata,ydata,lb,ub,options);
p6= lsqcurvefit(myfun,x0(:,6),xdata,ydata,lb,ub,options);
p7= lsqcurvefit(myfun,x0(:,7),xdata,ydata,lb,ub,options);
p8= lsqcurvefit(myfun,x0(:,8),xdata,ydata,lb,ub,options);
p9= lsqcurvefit(myfun,x0(:,9),xdata,ydata,lb,ub,options);
p10= lsqcurvefit(myfun,x0(:,10),xdata,ydata,lb,ub,options);

p290= lsqcurvefit(myfun,x0(:,290),xdata,ydata,lb,ub,options);
p291= lsqcurvefit(myfun,x0(:,291),xdata,ydata,lb,ub,options);
p292= lsqcurvefit(myfun,x0(:,292),xdata,ydata,lb,ub,options);
p293= lsqcurvefit(myfun,x0(:,293),xdata,ydata,lb,ub,options);
p294= lsqcurvefit(myfun,x0(:,294),xdata,ydata,lb,ub,options);
p295= lsqcurvefit(myfun,x0(:,295),xdata,ydata,lb,ub,options);
p296= lsqcurvefit(myfun,x0(:,296),xdata,ydata,lb,ub,options);
p297= lsqcurvefit(myfun,x0(:,297),xdata,ydata,lb,ub,options);
p298= lsqcurvefit(myfun,x0(:,298),xdata,ydata,lb,ub,options);
p299= lsqcurvefit(myfun,x0(:,299),xdata,ydata,lb,ub,options);
p300= lsqcurvefit(myfun,x0(:,300),xdata,ydata,lb,ub,options);

%Cost is the vector of 100 fitted constants
Cost=[p1(1) p2(1) p3(1) p4(1) p5(1) p6(1) p7(1) p8(1) p9(1) p10(1) p11(1) p12(1) p13(1) p14(1)
p15(1) p16(1) p17(1) p18(1) p19(1) p20(1) p21(1) p22(1) p23(1) p24(1) p25(1) p26(1) p27(1) p28(1)
p29(1) p30(1) p31(1) p32(1) p33(1) p34(1) p35(1) p36(1) p37(1) p38(1) p39(1) p40(1) p41(1) p42(1)
p43(1) p44(1) p45(1) p46(1) p47(1) p48(1) p49(1) p50(1) p51(1) p52(1) p53(1) p54(1) p55(1) p56(1)

```



```

p254(3) p255(3) p256(3) p257(3) p258(3) p259(3) p260(3) p261(3) p262(3) p263(3) p264(3) p265(3)
p266(3) p267(3) p268(3) p269(3) p270(3) p271(3) p272(3) p273(3) p274(3) p275(3) p276(3) p277(3)
p278(3) p279(3) p280(3) p281(3) p282(3) p283(3) p284(3) p285(3) p286(3) p287(3) p288(3) p289(3)
p290(3) p291(3) p292(3) p293(3) p294(3) p295(3) p296(3) p297(3) p298(3) p299(3) p300(3)];

%Phase is the vector of 100 fitted phase difference (degrees)
Phase=Phaserad*180./pi;
P=Phase'; %transpose of the matrix Phase

%S3 is the vector of 100 fitted S3
S3=[p1(4) p2(4) p3(4) p4(4) p5(4) p6(4) p7(4) p8(4) p9(4) p10(4) p11(4) p12(4) p13(4) p14(4)
p15(4) p16(4) p17(4) p18(4) p19(4) p20(4) p21(4) p22(4) p23(4) p24(4) p25(4) p26(4) p27(4) p28(4)
p29(4) p30(4) p31(4) p32(4) p33(4) p34(4) p35(4) p36(4) p37(4) p38(4) p39(4) p40(4) p41(4) p42(4)
p43(4) p44(4) p45(4) p46(4) p47(4) p48(4) p49(4) p50(4) p51(4) p52(4) p53(4) p54(4) p55(4) p56(4)
p57(4) p58(4) p59(4) p60(4) p61(4) p62(4) p63(4) p64(4) p65(4) p66(4) p67(4) p68(4) p69(4) p70(4)
p71(4) p72(4) p73(4) p74(4) p75(4) p76(4) p77(4) p78(4) p79(4) p80(4) p81(4) p82(4) p83(4) p84(4)
p85(4) p86(4) p87(4) p88(4) p89(4) p90(4) p91(4) p92(4) p93(4) p94(4) p95(4) p96(4) p97(4) p98(4)
p99(4) p100(4) p101(4) p102(4) p103(4) p104(4) p105(4) p106(4) p107(4) p108(4) p109(4) p110(4)
p111(4) p112(4) p113(4) p114(4) p115(4) p116(4) p117(4) p118(4) p119(4) p120(4) p121(4) p122(4)
p123(4) p124(4) p125(4) p126(4) p127(4) p128(4) p129(4) p130(4) p131(4) p132(4) p133(4) p134(4)
p135(4) p136(4) p137(4) p138(4) p139(4) p140(4) p141(4) p142(4) p143(4) p144(4) p145(4) p146(4)
p147(4) p148(4) p149(4) p150(4) p151(4) p152(4) p153(4) p154(4) p155(4) p156(4) p157(4) p158(4)
p159(4) p160(4) p161(4) p162(4) p163(4) p164(4) p165(4) p166(4) p167(4) p168(4) p169(4) p170(4)
p171(4) p172(4) p173(4) p174(4) p175(4) p176(4) p177(4) p178(4) p179(4) p180(4) p181(4) p182(4)
p183(4) p184(4) p185(4) p186(4) p187(4) p188(4) p189(4) p190(4) p191(4) p192(4) p193(4) p194(4)
p195(4) p196(4) p197(4) p198(4) p199(4) p200(4) p201(4) p202(4) p203(4) p204(4) p205(4) p206(4)
p207(4) p208(4) p209(4) p210(4) p211(4) p212(4) p213(4) p214(4) p215(4) p216(4) p217(4) p218(4)
p219(4) p220(4) p221(4) p222(4) p223(4) p224(4) p225(4) p226(4) p227(4) p228(4) p229(4) p230(4)
p231(4) p232(4) p233(4) p234(4) p235(4) p236(4) p237(4) p238(4) p239(4) p240(4) p241(4) p242(4)
p243(4) p244(4) p245(4) p246(4) p247(4) p248(4) p249(4) p250(4) p251(4) p252(4) p253(4) p254(4)
p255(4) p256(4) p257(4) p258(4) p259(4) p260(4) p261(4) p262(4) p263(4) p264(4) p265(4) p266(4)
p267(4) p268(4) p269(4) p270(4) p271(4) p272(4) p273(4) p274(4) p275(4) p276(4) p277(4) p278(4)
p279(4) p280(4) p281(4) p282(4) p283(4) p284(4) p285(4) p286(4) p287(4) p288(4) p289(4) p290(4)
p291(4) p292(4) p293(4) p294(4) p295(4) p296(4) p297(4) p298(4) p299(4) p300(4)];

Stokes3=S3';
AvCost=sum(Cost(:))./n
STDCost=std(Cost(:))
Avratio=sum(ratio(:))./n
STDratio=std(ratio(:))
AvPhase=sum(Phase(:))./n
STDPhase=std(Phase(:))
AvS3=sum(S3(:))./n
STDS3=std(S3(:))

%only for graphs fitted curve

F=((p40(1)/4.)*(R*(p40(2))^2+1)+DR*(p40(2))^2-
1)*cos(2*xdata)+(R*(p40(2))^2-1)+DR*(p40(2))^2+1)*cos(2*xdata))*(-
0.0793)+2*DR*cos(p40(3))*p40(2)*sin(2*xdata)*(0.902)+2*DR*sin(p40(3))*p40(2)*
sin(2*xdata)*p40(4)); % fitted curve
Mf=max(F); %max fitted curve
mf=min(F); %min fitted curve
Dmf=mf-m; %difference between max of the exp data and max of the fitted ones
DMf=Mf-M; %difference between min of the exp data and min of the fitted ones

figure;
plot(xdata,ydata,'b','LineWidth',1.5);
hold on;
plot(xdata,F,'r','LineWidth',1.5);
xlabel('rotation angle (°)','FontSize',12);

```



```

ylabel('intensity (a.u.)','FontSize',12);
legend ('exp','fit');

% Hist Phase
figure;
n=4; %numbers of bins
hist(Phase,n)
hold on;
xlabel('phase (°)','FontSize',12);
ylabel('counts','FontSize',12);

% Hist S3
figure;
n=4; %numbers of bins
hist(S3,n)
hold on;
xlabel('S3','FontSize',12);
ylabel('counts','FontSize',12);

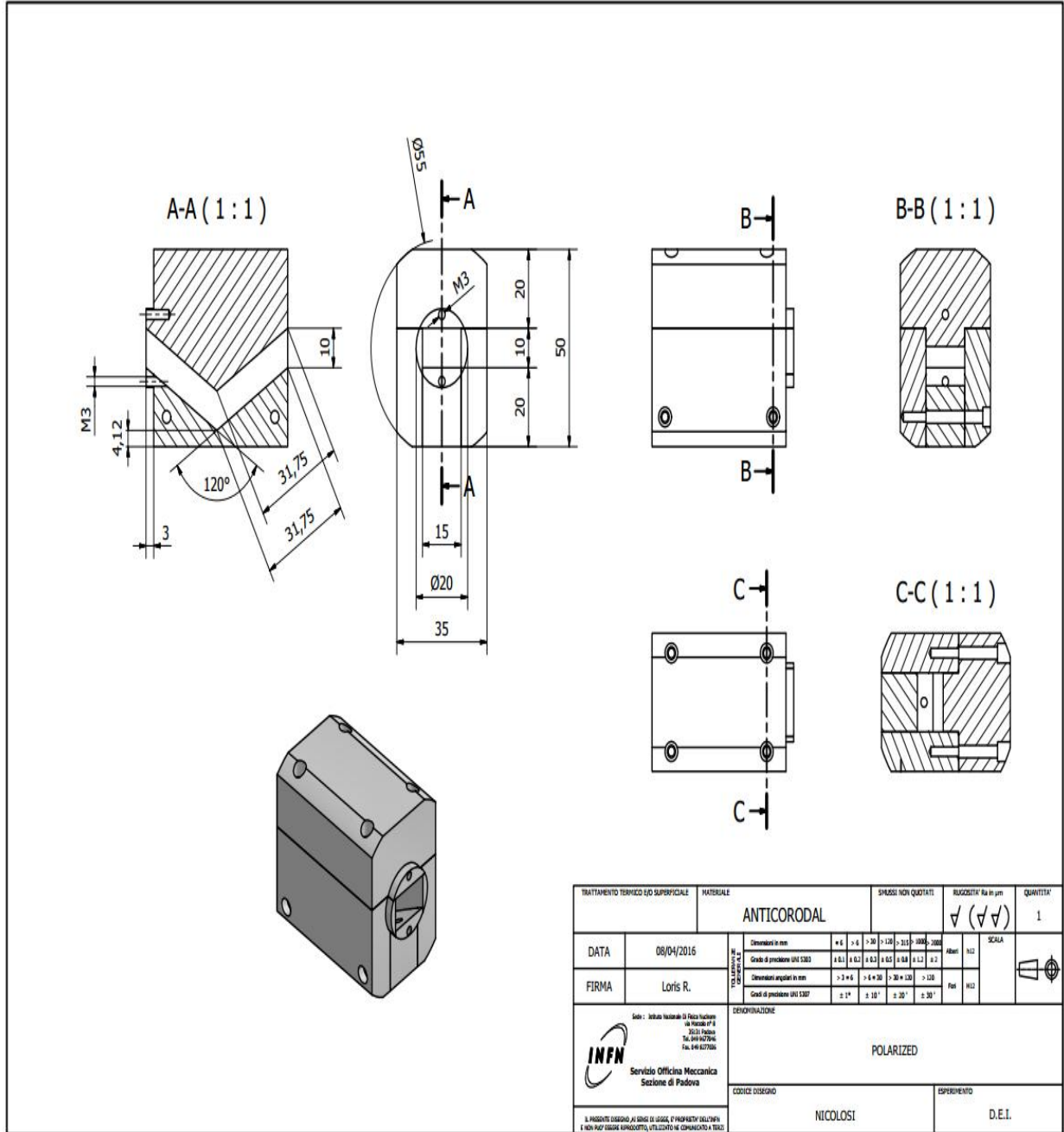
figure;
xlin = linspace(min(S3),max(S3),33);
ylin = linspace(min(Phase),max(Phase),33);
[X,Y] = meshgrid(xlin,ylin);
Z = griddata(S3,Phase, ratio,X,Y, 'cubic');
plot3(S3,Phase, ratio, 'd', 'LineWidth',1.5);
xlabel('S3','FontSize',12);
ylabel('phase(°)', 'FontSize',12);
legend ('exp','fit');

figure;
plot(S3,Phase, 'd', 'LineWidth',1.5);
xlabel('S3','FontSize',12);
ylabel('phase(°)', 'FontSize',12);
legend ('exp','fit');

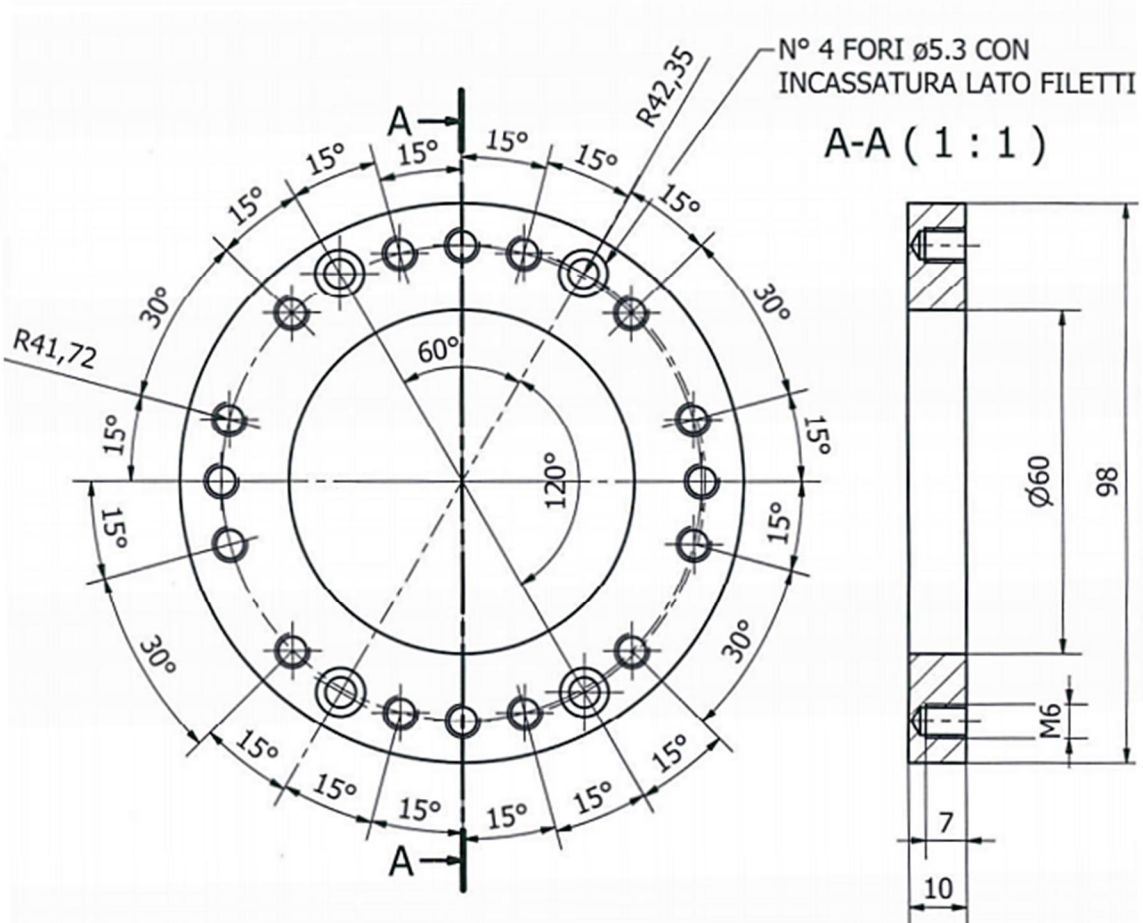
```

Appendix C. Opto-Mechanical Designs

1. The polarizer design

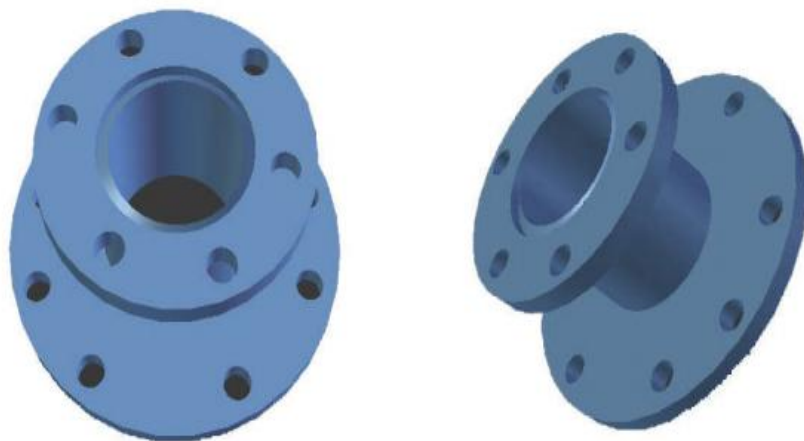
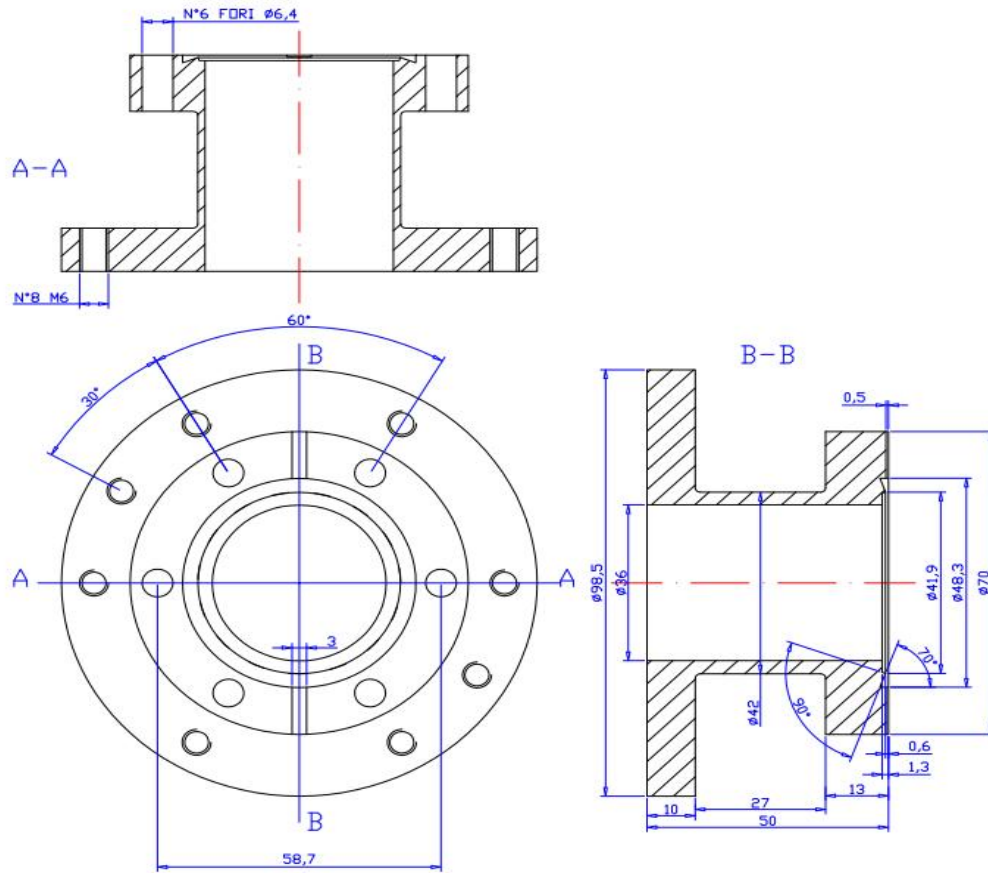


2. Experimental chamber rotation flange



TRATTAMENTO TERMICO E/O SUPERFICIALE		MATERIALE		SMUSSI NON QUOTATI		RUGOSITA' Ra in µm		QUANTITA'		
		ALLUMINIO				✓ (✓✓)		1		
DATA	06/05/2016	TOLERANZE GENERALI	Dimensioni in mm	± 0.1	± 0.2	± 0.3	± 0.5	± 0.8	± 1.2	
FIRMA	Loris R.		Grado di precisione UNI 5303	> 3 = 6	> 6 = 30	> 30 = 120	> 120			
			Dimensioni angolari in mm	± 1°	± 10'	± 20'	± 30'			
Sede: Istituto Nazionale Di Fisica Nucleare via Marconi n° 8 35131 Padova Tel. 049 9657046 Fax. 049 8277036		DENOMINAZIONE								
		FLANGIA CON ATTACCO A 30° - 45° - 60°								
		CODICE DISEGNO				ESPERIMENTO				
		NICOLOSI				DII				

3. Vacuum adaptive flange



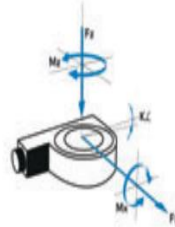
4. Rotation stage

5.132 Rotation Stage RS-40 Vacuum



FACTS

Load characteristics	$F_x(N)$	$F_z(N)$	$M_x(Nm)$	$M_z(Nm)$	$k_{ax}(\mu rad/Nm)$
FV	5	10	1	0.2	270
10-6	5	10	1	0.2	270
HV	5	10	1	0.2	270
UHVG	5	10	1	0.2	270



The RS-40 Vacuum rotation stage is very compact but offers a big 20 mm (25 mm holding diameter) aperture. A precision bearing guarantees a perfectly smooth move. The RS-40 Vacuum rotation stages have nearly zero backlash worm gear reduction. All RS-40 Vacuum motorized rotation stages are equipped with a reference switch and are offered with a special 2-phase geared vacuum stepper motor.

Please see "GLOSSARY Vacuum Specification" for all vacuum specification.



KEY FEATURES

- Vacuum up to 10⁻⁹ hPa
- Clear aperture 20 mm
- Uni-directional repeatability down to 0.005°
- Maximum speed 1.5°/sec
- Load capacity up to 1 kg
- Integrated hall reference switch
- Optionally rotary encoder on the rotation axis

TECHNICAL DATA

Travel range (°)	360
Flatness (Bearings) (μm)	±5
Eccentricity (Bearings) (μm)	±5
Wobble (Bearings) (μrad)	±35
Weight (kg)	0.4

Vacuum type	FV	10-6	HV	UHVG
Speed max. (°/sec)	1.5	0.6	0.6	0.27
Resolution calculated (°)	0.0021961 (FS)	0.0021961 (FS)	0.02 (FS)	0.02 (FS)
Resolution typical (°)	0.015	0.005	0.002	0.002
Bi-directional Repeatability (°)	±0.04	±0.04	±0.03	±0.03
Uni-directional Repeatability (°)	0.005	0.005	0.015	0.015
Nominal Current (A)	0.25	0.25	1.2	1.2

Accuracy	on request
Velocity range (mm/sec)	0.002 ... 1.5
Material	Aluminum, stainless steel, red brass

Vacuum Note: FS = full step, RE = rotary encoder

More info: Detailed information concerning motors and encoders, see appendix.

PI | micos

Bibliography

- [1] R. Saathof, G.J.M. Schutten, J.W. Spronck, R.H. Munnig Schmidt, Design and characterisation of an active mirror for EUV-lithography, *Precis. Eng.* 41 (2015) 102–110. doi:10.1016/j.precisioneng.2015.03.004.
- [2] N. V Edwards, Status and Prospects For VUV Ellipsometry (Applied to High K and Low K Materials), in: *AIP Conf. Proc.*, AIP, 2003: pp. 723–737. doi:10.1063/1.1622551.
- [3] C. Von Korff Schmising, D. Weder, T. Noll, B. Pfau, M. Hennecke, C. Strüber, I. Radu, M. Schneider, S. Staeck, C.M. Günther, J. Lüning, A.E.D. Merhe, J. Buck, G. Hartmann, J. Viefhaus, R. Treusch, S. Eisebitt, Generating circularly polarized radiation in the extreme ultraviolet spectral range at the free-electron laser FLASH, *Rev. Sci. Instrum.* 88 (2017). doi:10.1063/1.4983056.
- [4] B. Vodungbo, A. Barszczak Sardinha, J. Gautier, G. Lambert, C. Valentin, M. Lozano, G. Iaquaniello, F. Delmotte, S. Sebban, J. Lüning, P. Zeitoun, Polarization control of high order harmonics in the EUV photon energy range., *Opt. Express.* 19 (2011) 4346–4356. doi:10.1364/OE.19.004346.
- [5] B. De Pontieu, A.M. Title, J.R. Lemen, G.D. Kushner, D.J. Akin, B. Allard, T. Berger, P. Boerner, M. Cheung, C. Chou, J.F. Drake, D.W. Duncan, S. Freeland, G.F. Heyman, C. Hoffman, N.E. Hurlburt, R.W. Lindgren, D. Mathur, R. Rehse, D. Sabolish, R. Seguin, C.J. Schrijver, T.D. Tarbell, J.P. W??lser, C.J. Wolfson, C. Yanari, J. Mudge, N. Nguyen-Phuc, R. Timmons, R. van Bezooijen, I. Weingrod, R. Brookner, G. Butcher, B. Dougherty, J. Eder, V. Knagenhjelm, S. Larsen, D. Mansir, L. Phan, P. Boyle, P.N. Cheimets, E.E. DeLuca, L. Golub, R. Gates, E. Hertz, S. McKillop, S. Park, T. Perry, W.A. Podgorski, K. Reeves, S. Saar, P. Testa, H. Tian, M. Weber, C. Dunn, S. Eccles, S.A. Jaeggli, C.C. Kankelborg, K. Mashburn, N. Pust, L. Springer, R. Carvalho, L. Kleint, J. Marmie, E. Mazmanian, T.M.D. Pereira, S. Sawyer, J. Strong, S.P. Worden, M. Carlsson, V.H. Hansteen, J. Leenaarts, M. Wiesmann, J. Aloise, K.C. Chu, R.I. Bush, P.H. Scherrer, P. Brekke, J. Martinez-Sykora, B.W. Lites, S.W. McIntosh, H. Uitenbroek, T.J. Okamoto,

- M.A. Gummin, G. Auker, P. Jerram, P. Pool, N. Waltham, The Interface Region Imaging Spectrograph (IRIS), *Sol. Phys.* 289 (2014) 2733–2779. doi:10.1007/s11207-014-0485-y.
- [6] U. Schühle, The Lyman-alpha telescope of the extreme ultraviolet imager on Solar Orbiter, *SPIE Opt.* 8148 (2011) 81480K–81480K–11. doi:10.1117/12.893573.
- [7] David Attwood, *Soft X-rays and extreme ultraviolet radiation*, 1999.
- [8] J. Larruquert, *Optical properties of thin film materials at short wavelengths*, Woodhead Publishing Limited, 2013. doi:10.1533/9780857097316.2.290.
- [9] O. Kfir, P. Grychtol, E. Turgut, R. Knut, D. Zusin, Generation of phase-matched circularly-polarized extreme ultraviolet high harmonics for magnetic circular dichroism spectroscopy, *ArXiv*. (2014) 1–20. doi:10.1038/nphoton.2014.293.
- [10] J.A. Samson, D.L. Ederer, *Vacuum ultraviolet spectroscopy I*, Academic Press, 1998.
- [11] J.A. Samson, D.L. Ederer, *Vacuum Ultraviolet Spectroscopy II*, Academic Press, 1999.
- [12] M.A. Barstow, S.L. Casewell, J.B. Holberg, M.P. Kowalski, The status and future of EUV astronomy, *Adv. Sp. Res.* 53 (2014) 1003–1013. doi:10.1016/j.asr.2013.08.007.
- [13] P. Hyden, *Extreme Ultraviolet Source Development Using Laser Plasmas Containing Tin*, 2006.
- [14] Z. Huang, K.-J. Kim, Review of x-ray free-electron laser theory, *Phys. Rev. Spec. Top. Beams.* 10 (2007) 34801.
- [15] E. Allaria, L. Badano, S. Bassanese, F. Capotondi, D. Castronovo, P. Cinquegrana, M.B. Danailov, G. D’Auria, A. Demidovich, R. De Monte, G. De Ninno, S. Di Mitri, B. Diviacco, W.M. Fawley, M. Ferianis, E. Ferrari, G. Gaio, D. Gauthier, L. Giannessi, F. Iazzourene, G. Kurdi, N. Mahne, I. Nikolov, F. Parmigiani, G. Penco, L. Raimondi, P. Rebernik, F. Rossi, E. Roussel, C. Scafuri, C. Serpico, P. Sigalotti, C. Spezzani, M. Svandrlík, C. Svetina, M. Trovó, M. Veronese, D. Zangrando, M. Zangrando, The FERMI free-electron lasers, *J. Synchrotron Radiat.* 22 (2015) 485–491. doi:10.1107/S1600577515005366.
- [16] J. Peatross, M. Ware, *Physics of Light and Optics*, 2010. doi:10.1364/FIO.2010.JWA64.

- [17] N.I. Chkhalo, S.A. Gusev, A.N. Nechay, D.E. Pariev, V.N. Polkovnikov, N.N. Salashchenko, F. Schäfers, M.G. Sertsu, A. Sokolov, M. V. Svechnikov, D.A. Tatarsky, High-reflection Mo/Be/Si multilayers for EUV lithography, *Opt. Lett.* 42 (2017) 5070. doi:10.1364/OL.42.005070.
- [18] E. Louis, A.E. Yakshin, T. Tsarfati, F. Bijkerk, Nanometer interface and materials control for multilayer EUV-optical applications, *Prog. Surf. Sci.* 86 (2011) 255–294. doi:10.1016/j.progsurf.2011.08.001.
- [19] D. Goldstein, *Polarized light*, 2nd ed., Marcel Dekker, 2003.
- [20] P.J. Ouseph, K. Driver, J. Conklin, Polarization of light by reflection and the Brewster angle, *Am. J. Phys.* 69 (2001) 1166. doi:10.1119/1.1397457.
- [21] H.L. Marshall, R. Heilmann, N.S. Schulz, *A Soft X-ray Polarimeter*, (2010) 1–15.
- [22] E. Allaria, R. Appio, L. Badano, W.A. Barletta, S. Bassanese, S.G. Biedron, A. Borga, E. Busetto, D. Castronovo, P. Cinquegrana, S. Cleva, D. Cocco, M. Cornacchia, P. Craievich, I. Cudin, G. D’Auria, M. Dal Forno, M.B. Danailov, R. De Monte, G. De Ninno, P. Delgiusto, A. Demidovich, S. Di Mitri, B. Diviacco, A. Fabris, R. Fabris, W. Fawley, M. Ferianis, E. Ferrari, S. Ferry, L. Froehlich, P. Furlan, G. Gaio, F. Gelmetti, L. Giannessi, M. Giannini, R. Gobessi, R. Ivanov, E. Karantzoulis, M. Lonza, A. Lutman, B. Mahieu, M. Milloch, S. V. Milton, M. Musardo, I. Nikolov, S. Noe, F. Parmigiani, G. Penco, M. Petronio, L. Pivetta, M. Predonzani, F. Rossi, L. Rumiz, A. Salom, C. Scafuri, C. Serpico, P. Sigalotti, S. Spampinati, C. Spezzani, M. Svandrlík, C. Svetina, S. Tazzari, M. Trovo, R. Umer, A. Vascotto, M. Veronese, R. Visintini, M. Zaccaria, D. Zangrando, M. Zangrando, Highly coherent and stable pulses from the FERMI seeded free-electron laser in the extreme ultraviolet, *Nat. Photonics.* 6 (2012) 699–704. doi:10.1038/nphoton.2012.233.
- [23] P. Finetti, D.M.P. Holland, C.J. Latimer, C. Binns, Polarisation analysis of VUV synchrotron radiation emitted from a bending magnet source in the energy range 20-50 eV: A comparison between measurements and theoretical predictions, *Nucl. Instruments Methods Phys. Res. Sect. B Beam Interact. with Mater. Atoms.* 215 (2004) 565–576. doi:10.1016/j.nimb.2003.08.034.

- [24] E. Allaria, B. Diviacco, C. Callegari, P. Finetti, B.B.M. Mahieu, J. Viefhaus, M. Zangrando, G. De Ninno, G. Lambert, E. Ferrari, J. Buck, M. Ilchen, B. Vodungbo, N. Mahne, C. Svetina, C. Spezzani, S. Di Mitri, G. Penco, M. Trovo, W.M. Fawley, P.R. Rebernik, D. Gauthier, C. Grazioli, M. Coreno, B. Ressel, A. Kivimäki, T. Mazza, L. Glaser, F. Scholz, J. Seltmann, P. Gessler, J. Grünert, A. De Fanis, M. Meyer, A.K.A. Knie, S.P. Moeller, L. Raimondi, F. Capotondi, E. Pedersoli, O. Plekan, M.B. Danailov, A. Demidovich, I. Nikolov, A. Abrami, J. Gautier, J. Lüning, P. Zeitoun, L. Giannessi, M. Trovati, W.M. Fawley, P.R. Rebernik, D. Gauthier, C. Grazioli, M. Coreno, B. Ressel, A. Kivimäki, T. Mazza, L. Glaser, F. Scholz, J. Seltmann, P. Gessler, J. Grünert, A. De Fanis, M. Meyer, A.K.A. Knie, S.P. Moeller, L. Raimondi, F. Capotondi, E. Pedersoli, O. Plekan, M.B. Danailov, A. Demidovich, I. Nikolov, A. Abrami, J. Gautier, J. Lüning, P. Zeitoun, L. Giannessi, Control of the polarization of a vacuum-ultraviolet, high-gain, free-electron laser, *Phys. Rev. X*. 4 (2014) 1–15. doi:10.1103/PhysRevX.4.041040.
- [25] P. Joos, Measurement of the polarization of synchrotron radiation, *Phys. Rev. Lett.* 4 (1960) 558.
- [26] J. Kim, M. Zukic, M.M. Wilson, D.G. Torr, Design and fabrication of a reflection far-ultraviolet polarizer and retarder, in: *X-Ray Ultrav. Polarim.*, International Society for Optics and Photonics, 1994: pp. 93–104.
- [27] W.C. Johnson Jr, Magnesium fluoride polarizing prism for the vacuum ultraviolet, *Rev. Sci. Instrum.* 35 (1964) 1375–1376.
- [28] D.L. Steinrnetz, W.G. Phillips, M. Wirick, F.F. Forbes, A polarizer for the vacuum ultraviolet, *Appl. Opt.* 6 (1967) 1001–1004.
- [29] J. Kim, M. Zukic, D.G. Torr, Multilayer thin film design for far ultraviolet polarizers using an induced transmission and absorption technique, *NASA-CR-19* (1993) 142–149.
- [30] F. Bridou, M. Cuniot-Ponsard, J.M. Desvignes, A. Gottwald, U. Kroth, M. Richter, Polarizing and non-polarizing mirrors for the hydrogen Lyman- α radiation at 121.6 nm, *Appl. Phys. A Mater. Sci. Process.* 102 (2011) 641–649. doi:10.1007/s00339-010-6133-y.
- [31] F. Bridou, M. Cuniot-Ponsard, J.-M. Desvignes, M. Richter, U. Kroth, a. Gottwald,

- Experimental determination of optical constants of MgF₂ and AlF₃ thin films in the vacuum ultra-violet wavelength region (60–124nm), and its application to optical designs, *Opt. Commun.* 283 (2010) 1351–1358. doi:10.1016/j.optcom.2009.11.062.
- [32] G. Hass, W.R. Hunter, Reflection polarizers for the vacuum ultraviolet using Al+ MgF₂ mirrors and an MgF₂ plate, *Appl. Opt.* 17 (1978) 76–82.
- [33] M. Yang, C. Cobet, N. Esser, Tunable thin film polarizer for the vacuum ultraviolet and soft x-ray spectral regions, *J. Appl. Phys.* 101 (2007) 53114. doi:10.1063/1.2710354.
- [34] L.R. Marcos, J.I. Larruquert, J.A. Aznárez, J.A. Méndez, A.M. Malvezzi, *Advances In FUV Coatings For Space Instrumentation*, 2016.
- [35] Z.-Y. Guo, S.-B. Xi, J.-T. Zhu, Y.-D. Zhao, L. Zheng, C.-H. Hong, K. Tang, D.-L. Yang, M.-Q. Cui, Measurement of the polarization for soft X-ray magnetic circular dichroism at the BSRF beamline 4B7B, *Chin. Phys. C.* 37 (2013) 018001. doi:10.1088/1674-1137/37/1/018001.
- [36] M.F. Tesch, M.C. Gilbert, H.-C. Mertins, D.E. Bürgler, U. Berges, C.M. Schneider, X-ray magneto-optical polarization spectroscopy: an analysis from the visible region to the x-ray regime., *Appl. Opt.* 52 (2013) 4294–310. doi:10.1364/AO.52.004294.
- [37] N.-E. Raouafi, P. Lemaire, S. Sahal-Bréchet, Detection of the O VI 103.2 nm line polarization by the SUMER spectrometer on the SOHO spacecraft, *Astron. Astrophys.* 345 (1999) 999–1005.
- [38] H. Peter, L. Abbo, V. Andretta, F. Auchère, A. Bemporad, F. Berrilli, V. Bommier, A. Braukhane, R. Casini, W. Curdt, J. Davila, H. Dittus, S. Fineschi, A. Fludra, A. Gandorfer, D. Griffin, B. Inhester, A. Lagg, E.L. Degl’Innocenti, V. Maiwald, R.M. Sainz, V.M. Pillet, S. Matthews, D. Moses, S. Parenti, A. Pietarila, D. Quantius, N.E. Raouafi, J. Raymond, P. Rochus, O. Romberg, M. Schlotterer, U. Schühle, S. Solanki, D. Spadaro, L. Teriaca, S. Tomczyk, J.T. Bueno, J.C. Vial, Solar magnetism eXplorer (SolmeX): Exploring the magnetic field in the upper atmosphere of our closest star, *Exp. Astron.* 33 (2012) 271–303. doi:10.1007/s10686-011-9271-0.

- [39] F. Snik, *Astronomical Polarimetry*, 2009.
- [40] N.-E. Raouafi, J.W. Harvey, S.K. Solanki, Properties of solar polar coronal plumes constrained by ultraviolet coronagraph spectrometer data, *Astrophys. J.* 658 (2007) 643.
- [41] Spectroscopic ellipsometry: a historical overview, *Thin Solid Films.* 313–314 (1998) 1–9. doi:10.1016/S0040-6090(97)00762-1.
- [42] J. Jung, J. Bork, T. Holmgaard, N. a. Kortbek, *Ellipsometry*, 2004.
- [43] R.M. a Azzam, *Ellipsometry*, in: *Handb. Opt.*, n.d.: p. 27.1-27.27.
- [44] M. Schledermann, M. Skibowski, Determination of the Ellipticity of Light and of Optical Constants by Use of Two Reflection Polarizers, *Appl. Opt.* 10 (1971) 321.
- [45] J. Barth, R.L. Johnson, S. Logothetidis, M. Cardona, D. Fuchs, A.M. Bradshaw, *Spectroscopic Ellipsometry with Synchrotron Radiation: Latest Developments*, in: 1986: pp. 733–737.
- [46] H. Onuki, N. Saito, T. Saito, Undulator generating any kind of elliptically polarized radiation, *Appl. Phys. Lett.* 52 (1988) 173–175. doi:10.1063/1.99510.
- [47] K. Dorywalski, I. Maciejewski, T. Krzyżyński, Spectroscopic ellipsometry technique as a materials characterization tool for mechatronic systems—The case of composition and doping concentration monitoring in SBN crystals, *Mechatronics.* 37 (2015) 33–41. doi:10.1016/j.mechatronics.2015.11.005.
- [48] A. Kumar, A.K. Ghatak, *Polarization of light with applications in optical fibers*, SPIE Press, 2011.
- [49] R.C. Jones, I. Description and Discussion of the Calculus, *J.O.S.A.* 31 (1941) 488–493. doi:http://dx.doi.org/10.1364/JOSA.31.000488.
- [50] H.G.H.G. Tompkins, E.A.E.A. Irene, C. Hill, N. Carolina, *Handbook of Ellipsometry*, 2005. doi:10.1007/3-540-27488-X.
- [51] [Http://www.sjuts.com](http://www.sjuts.com), for more details about the detector, (n.d.).

- [52] <http://www.hamamatsu.com>, for more details about the lamp, (2018).
- [53] K. Brodie, S. Neate, Features and Operation of Hollow Cathode Lamps and Deuterium Lamps, (1988) 1–6.
- [54] G. Bonanno, G. Naletto, G. Tondello, A test facility to calibrate EUV detectors, in: ESA Symp. Phot. Detect. Sp. Instrumentations, 1992: pp. 233–236.
- [55] G. Monaco, High reflective optics for different spectral region, University of Padova, 2009.
- [56] A.J. Corso, Ground calibration of PHEBUS spectrometer on board of BEPICOLOMBO mission, 2012.
- [57] E.D. Palik, Handbook of optical constants of solids II, 1985.
- [58] J.I. Larruquert, A.M. Malvezzi, A. Giglia, J.A. Aznárez, L. Rodríguez-de Marcos, J.A. Méndez, P. Miotti, F. Frassetto, G. Massone, S. Nannarone, G. Crescenzo, G. Capobianco, S. Fineschi, Reflective and transmissive broadband coating polarizers in a spectral range centered at 121.6nm, *J. Opt. (United Kingdom)*. 16 (2014) 125713. doi:10.1088/2040-8978/16/12/125713.
- [59] <https://www.physikinstrumente.com>, for more details about the rotation stage, (2016).
- [60] Z. Wang, H. Wang, J. Zhu, Z. Zhang, F. Wang, Y. Xu, S. Zhang, W. Wu, L. Chen, A.G. Michette, S.J. Pfauntsch, A.K. Powell, F. Schäfers, A. Gaupp, M. Cui, L. Sun, M. MacDonald, Complete polarization analysis of extreme ultraviolet radiation with a broadband phase retarder and analyzer, *Appl. Phys. Lett.* 90 (2007) 3–5. doi:10.1063/1.2678973.
- [61] T. Kihara, Measurement method of Stokes parameters using a quarter-wave plate with phase difference errors., *Appl. Opt.* 50 (2011) 2582–7. doi:10.1364/AO.50.002582.
- [62] E. Garcia-Cauarel, A. De Martino, J.P. Gaston, L. Yan, Application of spectroscopic ellipsometry and mueller ellipsometry to optical characterization, *Appl. Spectrosc.* 67 (2013) 1–21. doi:10.1366/12-06883.
- [63] H.G. Berry, G. Gabrielse, a E. Livingston, Measurement of the Stokes parameters of light.,

- Appl. Opt. 16 (1977) 3200–3205. doi:10.1364/AO.16.003200.
- [64] A.E.H. Gaballah, P. Nicolosi, N. Ahmed, K. Jimenez, G. Pettinari, A. Gerardino, P. Zuppella, EUV polarimetry for thin film and surface characterization and EUV phase retarder reflector development, *Rev. Sci. Instrum.* 89 (2018) 015108. doi:10.1063/1.5010786.
- [65] T. Saito, A. Ejiri, H. Onuki, Polarization properties of an evaporated aluminum mirror in the VUV region, *Appl. Opt.* 29 (1990) 4538–4540. doi:10.1364/AO.29.004538.
- [66] <http://www.rxollc.com/idl/>, x-ray optics software, (n.d.).
- [67] J.H. Weaver, C. Krafska, D.W. Lynch, E.E. Koch, Optical properties of metals. Pt. 2, *Phys. Data*. Vol. 18-1, (1981).
- [68] R.P. MADDEN, L.R. CANFIELD, G. HASS, On the Vacuum-Ultraviolet Reflectance of Evaporated Aluminum before and during Oxidation, *J. Opt. Soc. Am.* 53 (1963) 620. doi:10.1364/JOSA.53.000620.
- [69] W.B. Westerveld, K. Becker, P.W. Zetner, J.J. Corr, J.W. McConkey, Production and measurement of circular polarization in the VUV, *Appl. Opt.* 24 (1985) 2256–2262. doi:10.1364/AO.24.002256.
- [70] D. Wilson, D. Rudolf, C. Weier, R. Adam, G. Winkler, R. Frömter, S. Danylyuk, K. Bergmann, D. Detlev Grützmacher, C.M. Schneider, L. Juschkina, Generation of circularly polarized radiation from a compact plasma-based extreme ultraviolet light source for tabletop X-ray magnetic circular dichroism studies, *Rev. Sci. Instrum.* 85 (2014). doi:10.1063/1.4897491.
- [71] C. Lin, S. Chen, Z. Chen, Y. Ding, Design of reflective quarter-wave plates in extreme ultraviolet, *Opt. Commun.* 347 (2015) 98–101. doi:10.1016/j.optcom.2015.03.010.
- [72] L.R. Canfield, G. Hass, J.E. Waylonis, Further Studies on MgF₂ Overcoated Aluminum Mirrors with Highest Reflectance in the Vacuum Ultraviolet, *Appl. Opt.* 5 (1966) 45. doi:10.1364/AO.5.000045.

- [73] J.I. Larruquert, R.A.M. Keski-Kuha, Far ultraviolet optical properties of MgF₂ films deposited by ion-beam sputtering and their application as protective coatings for Al, *Opt. Commun.* 215 (2002) 93–99. doi:10.1016/S0030-4018(02)02229-0.
- [74] E.T. Hutcheson, G. Hass, J.T. Cox, Effect of Deposition Rate and Substrate Temperature on the Vacuum Ultraviolet Reflectance of MgF(2)- and LiF-Overcoated Aluminum Mirrors., *Appl. Opt.* 11 (1972) 2245–2248. doi:10.1364/AO.11.002245.
- [75] J. Hennessy, K. Balasubramanian, C.S. Moore, A.D. Jewell, S. Nikzad, K. France, M. Quijada, Performance and prospects of far ultraviolet aluminum mirrors protected by atomic layer deposition, *J. Astron. Telesc. Instruments, Syst.* 2 (2016) 041206. doi:10.1117/1.JATIS.2.4.041206.
- [76] L. V. Rodríguez-de Marcos, J.I. Larruquert, J.A. Méndez, J.A. Aznárez, Self-consistent optical constants of MgF₂, LaF₃, and CeF₃ films, *Opt. Mater. Express.* 7 (2017) 989. doi:10.1364/OME.7.000989.
- [77] B. Ellis, The spectral response of Pb/SnTe detectors, *Infrared Phys.* 17 (1977) 365–374. doi:10.1016/0020-0891(77)90038-0.
- [78] R. Ishikawa, T. Yamaguchi, Y. Ohtaki, R. Akiyama, S. Kuroda, Thin film growth of a topological crystal insulator SnTe on the CdTe (111) surface by molecular beam epitaxy, *J. Cryst. Growth.* 453 (2016) 124–129. doi:10.1016/j.jcrysgro.2016.08.027.
- [79] Y.Y. Wang, K.F. Cai, X. Yao, Facile synthesis and characterization of SnTe films, *Appl. Surf. Sci.* 258 (2011) 919–922. doi:10.1016/j.apsusc.2011.09.027.
- [80] L. Walmsley, L. Waxer, C. Dorrer, The role of dispersion in ultrafast optics, *Rev. Sci. Instrum.* 72 (2001) 1–29. doi:10.1063/1.1330575.
- [81] A. Aquila, F. Salmassi, E. Gullikson, Metrologies for the phase characterization of attosecond extreme ultraviolet optics., *Opt. Lett.* 33 (2008) 455–457. doi:10.1364/OL.33.000455.
- [82] <https://www.elettra.trieste.it>, Elettra Sincrotrone Trieste, *Science* (80-.). (2014) 13–14.

- [83] J.I. Larruquert, R.A. Keski-Kuha, Reflectance measurements and optical constants in the extreme ultraviolet of thin films of ion-beam-deposited carbon, *Opt. Commun.* 183 (2000) 437–443. doi:10.1016/S0030-4018(00)00884-1.
- [84] F. Wang, L. Liu, W. Duan, L. Jiang, W. Li, Z. Wang, J. Zhu, Z. Zhang, L. Chen, H. Zhou, T. Huo, Reflective phase shift measurement of the Mo/Si multilayer mirror in extreme ultraviolet region, *Optik (Stuttg.)* 124 (2013) 5003–5006. doi:10.1016/j.ijleo.2013.03.088.
- [85] R.B. Schoolar, J.R. Dixon, Optical properties of tin telluride in the visible and infrared regions, *Josa.* 58 (1968) 119–124. doi:10.1364/JOSA.58.000119.
- [86] V.S. Neudachina, T.B. Shatalova, V.I. Shtanov, L. V. Yashina, T.S. Zyubina, M.E. Tamm, S.P. Kobeleva, XPS study of SnTe(1 0 0) oxidation by molecular oxygen, *Surf. Sci.* 584 (2005) 77–82. doi:10.1016/j.susc.2005.01.061.
- [87] Cao. Guozhong, Two-Dimensional Nanostructures: Thin Films, in: *Nanostructures Nanomater.*, published by Imperial College Press and distributed by World Scientific Publishing Co., 2004: pp. 173–228. doi:10.1142/9781860945960_0005.
- [88] M. Ohring, *Materials science of thin films*, Academic press, 2001.